ΕΘΝΙΚΟ ΜΕΤΣΟΒΙΟ
ΠΟΛΥΤΕΧΝΕΙΟ

ΣΧΟΛΗ ΕΦΑΡΜΟΣΜΕΝΩΝ
ΜΑΘΗΜΑΤΙΚΩΝ
ΚΑΙ ΦΥΣΙΚΩΝ ΕΠΙΣΤΗΜΩΝ

ΣΧΟΛΗ ΜΗΧΑΝΟΛΟΓΩΝ
ΜΗΧΑΝΙΚΩΝ

ΕΚΕΦΕ «ΔΗΜΟΚΡΙΤΟΣ»

ΙΝΣΤΙΤΟΥΤΟ
ΝΑΝΟΕΠΙΣΤΗΜΗΣ ΚΑΙ
ΝΑΝΟΤΕΧΝΟΛΟΓΙΑΣ

ΙΝΣΤΙΤΟΥΤΟ ΠΥΡΗΝΙΚΗΣ
ΚΑΙ ΣΩΜΑΤΙΔΙΑΚΗΣ
ΦΥΣΙΚΗΣ

Διατμηματικό Πρόγραμμα Μεταπτυχιακών Σπουδών

«Φυσική και Τεχνολογικές Εφαρμογές»

Μελέτη των ανιχνευτών Micromegas με χρήση του VMM ASIC readout για την αναβάθμιση του NSW

ΜΕΤΑΠΤΥΧΙΑΚΗ ΔΙΠΛΩΜΑΤΙΚΗ ΕΡΓΑΣΙΑ

του Χρήστου Παρασκευόπουλου

Επιβλέπων: Θεόδωρος Αλεξόπουλος

Αθήνα, Φεβρουάριος,2017

Ευχαριστίες

Για την εκπόνηση της παρούσας διπλωματικής εργασίας θα ήθελα να εκφράσω τις ευχαριστίες μου σε όλους όσους με στήριξαν και με βοήθησαν σε όλη την διάρκεια της εκπόνησης και συγγραφής της.

Αρχικά θα ήθελα να ευχαριστήσω τον επιβλέποντα καθηγητή μου κ.Θεόδωρο Αλεξόπουλο για την βοήθεια και καθοδήγηση που μου παρείχε. Ο αρχηγός παρείχε συμβουλές, έδινε κίνητρο, υποστήριξη και ήταν πάντα διαθέσιμος και υπομονετικός σε ότι χρειαζόμουν. Ακόμη μου έδωσε την ευκαιρία να είμαι μέρος της ομάδας Πειραματικής Φυσικής Υψηλών Ενεργειών του Ε.Μ.Π. συμμετέχωντας σε έρευνα και δραστηριότητες.

Θα ήθελα να ευχαριστήσω τον κ.Σταύρο Μαλτέζο του οποίου οι συμβουλές ήταν πάντα χρήσιμες και με εξαιρετικό ενδιαφέρον.

Επίσης θα ήθελα επίσης να ευχαριστήσω του συμφοιτητές και φίλους μου Ανδρέα Βγενόπουλο, Μάριο Νάτσιο και Δημήτρη Τζανετάτο που έχουμε συνεργαστεί αμέτρητες ώρες σε θέματα που αφορούν την δουλειά μας σε αυτό τον τομέα και όχι μόνο.

΄Ενα μεγάλο ευχαριστώ χρωστάω στους γονείς μου και τα αδέρφια μου για την στήριξη και την αγάπη τους όλα αυτά τα χρόνια.

Ακόμη ευχαριστώ την Ευγενία η οποία με την ανεξάντλητη υπομονή της είναι πάντα δίπλα μου παρόλο τον μεγάλο φόρτο εργασίας και των δυο μας.

Περίληψη

Οι ανιχνευτές MicroMegas (MM) και small-strip Thin Gap Chambers (sTGC) έχουν επιλεχθεί για να εξοπλίσουν την αναβάθμιση του NSW στο φασματόμετρο μιονίων του ALTAS ως μέρος του sLHC. Οι resistive MM έχουν πολλά πλεονεκτήματα όπως χαμηλό κόστος κατασκευής, αντοχή σε περιβάλλον ηψηλής ακτινοβολίας και δεν έχουν περιορισμούς από αποφορτίσεις και σπινθηρισμούς. Ακόμη παρέχουν πολύ καλή χωρική ανάλυση σε τάξη μικρότερη των 100 μm.

Σε αυτή την διπλωματική χρησιμοποιήθηκαν δεδομένα με το νέο σύστημα readout που θα χρησιμοποιηθεί στο NSW, τα VMM με την χρήση των πρωτότυπων ανιχνευτών του SM1 και LM2. Κατά την διάρκεια του Σεπτεμβρίου, Δεκεμβρίου του 2016 και Ιανουαρίου του 2017 έγινε ανάλυση δεδομένων με τις εκδόσεις VMM2 και VMM3.

Το πρώτο κεφάλαιο είναι μια σύντομη περιγραφή του Πειράματος ATLAS και της αναβάθμισης του NSW. Στο δεύτερο είναι οι κύριες αρχές αλληλεπίδρασης των σωματιδίων με την ύλη. Στην συνέχεια πως εξελίχθηκαν οι ανιχνευτές που κάνουν χρήση αυτών των ιδιοτήτων μέχρι την δημιουργία των MicroMegas. Το τρίτο κεφάλαιο περιγράφει τα ηλεκτρονικά συστήματα του NSW με πλήρη ανάλυση της λειτουργίας του VMM2. Στο τέταρτο κεφάλαιο περιγράφεται η πειραματική διάταξη και η ανάλυση των δεδομένων μέσω αυτών των συστημάτων.

Abstract

MicroMegas (MM) Detector along with the small-strip Thin Gap Chambers (sTGC) are the chosen technologies for the New Small Wheel upgrade at the Atlas experiment for the sLHC. Resistive MM detectors have many advantages such as low construction costs, tolerance to high radiation environment with no limitation from discharges and sparks. Also they have very good tracking capabilities with spatial resolution less than 100 μm.

This thesis focused in the data retrieved from the new readout System the VMM ASIC fitted on the prototype NSW chambers SM1 and LM2. VMM is designed for the purposes of the NSW project and will be used as the front end ASIC. During the tests beams of September, December of 2016 and January of 2017 the data analysis was implemented with the VMM2 and VMM3 versions .

In the first chapter of this thesis there is a brief description of the ATLAS experiment and the motivation for the upgrade of the NSW. In the second chapter there are some basic principles of the interactions of particles with matter. Then the evolution of the proportional chambers until the MM implementation and operation. In the third chapter there is the brief description of the NSW electronics system. The same chapter has an extensive description of the overall capabilities the VMM utilises from signal processing to triggering. In the fourth chapter there is a description of the experimental setups that been used and the analysis of the data outputs from the VMM readout system.

CONTENTS

LIST OF FIGURES

LIST OF TABLES

CHAPTER 1

THE ATLAS DETECTOR AT THE LARGE HADRON COLLIDER AT CERN

In this chapter there is a brief description to the world's largest and most powerful accelerator the Large Hadron Collider (LHC) with emphasis to the ATLAS detector and the Muon Spectrometer. LHC is going to be upgraded in higher luminosity (High Luminosity LHC (HL-LHC)) so the muon spectrometer of ATLAS must be evolved in order to be able to handle the increased particle rates. The Micromegas detector was chosen for the upgrade of the New Small Wheel (NSW) in the muon spectrometer which is the major subject of research of this thesis.

1.1 The Large Hadron Collider

The Large Hadron Collider (LHC) [3] is the world's greatest particle accelerator. It consists of two superconducting rings and is located the under the French-Swiss boarders at a depth ranging from 50 to 175 metres underground. LHC is in the 26.7 km tunnel at the European Organisation of Nuclear Research (CERN).

LHC was built during the 1984-1989 for the needs of CERN LEP [4] which operated until 2000 .The first beam was produced in September of 2008 and collisions came later during the same year. The centre of mass energies aimed to the luminosity of a level up to 14 TeV and the main target is to reveal the physics beyond the Standard Model.

Experiments and the complex of LHC

The LHC has four majors experiments. The two general purpose experiments are ATLAS [5] and CMS [6] and aims at the luminosity of $\mathcal{L} = 10^{34}\ cm^{-2}\ s^{-1}$ for p-p collisions. Moreover there are the LHCb [7] experiment which aims to the luminosity

of $L = 10^{32} cm^{-2} s^{-1}$ and TOTEM [8], for proton detection from elastic scattering at small angles which aims to $L = 2 \times 10^{29}\ cm^{-2} s^{-1}$.

Additionally LHC can operate not only with p-p collisions but also Pb-Pb ion beams and p-Pb beams. Ion beams are detected from ALICE experiment [9] at a peak luminosity of $L = 10^{27}\ cm^{-2} s^{-1}$.

Particles before arriving at the LHC ring must follow a succession of machines that aim to increase their energies. Initially a bottle of Hydrogen gas fills the chamber of a linear accelerator. Then electric field is applied to the hydrogen nuclei and isolated protons are kept to proceed to the next stage of route. The initial energy of 50 MeV is performed from the linear accelerator LINear ACcelerator 2 (LINAC 2). The beam continues to the Proton Synchrotron Booster(PSB) and reaches the energy of 1.4 GeV before Proton Synchrotron (PS) accelerates the particles to energy of 25 GeV.

The last step before proton are injected into the LHC is the Super Proton Synchrotron (SPS) where they reach energies at the range of 450 GeV and then LHC accelerates them at the nominal energy of 7 TeV .

Most of the accelerators we described are also used for experiments with lower energy ranges. The complex of accelerators at CERN is shown below.

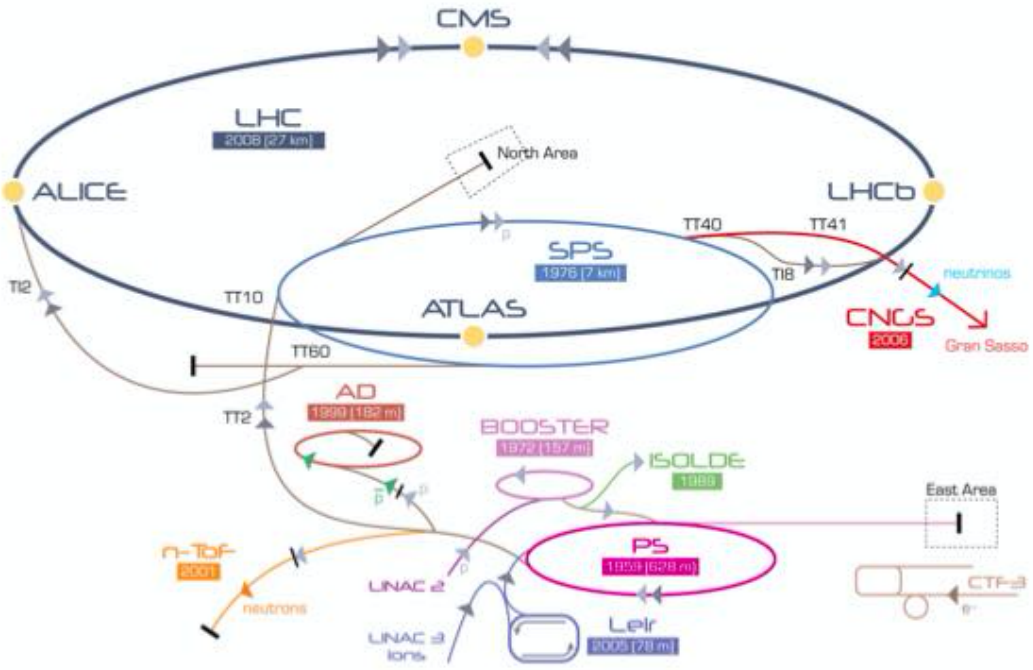

Figure 1.1: The accelerator complex at CERN

The instantaneous luminosity L of LHC is proportional to the rate R for p-p collisions and it is $\mathcal{L} = \mathcal{R}/\sigma$ where the σ is the cross section of the p-p collision. The

luminosity is depended only from beam parameters and is equal to:

$$\mathcal{L} = \frac{n_b f_r n_1 n_2}{2\pi \Sigma_x \Sigma_y} \tag{1.1}$$

In the equation 1.1 the f_r is the revolution frequency, the n_b is the number of bunches colliding at the interaction point n_1 and n_2 are the number of particles in the two colliding bunches and Σ_x,Σ_y are the horizontal and vertical beam profiles taking into account that both beams have similar characteristics. The luminosity of the LHC is not constant but decays due to beam loss from collisions. The two biggest experiments of LHC, ATLAS [5] and CMS [6] aim to the peak luminosity of $\mathcal{L} = 10^{34}\ cm^{-2}\ s^{-1}$ for p-p collisions.

To achieve such a strong luminosity high intensity beams are required. Two rings with separate magnet fields and counter rotating beams and vacuum chambers in the main arcs with common sections only at the insertion regions where the experimental detectors are located. More than a thousand superconducting dipole, quadrupole, sextupole, octupole and decapole magnets bend and tighten the beams around the 27 km circumference of the LHC.

At the nominal energy of 7 TeV per beam a magnetic field of around 8.4 T at a current of around 11.7 kA is required with the magnets having two apertures, one for each of the counter-rotating beams. This extremely high field can only be achieved with magnets made of superconducting Niobium-Titanium (NbTi) material and cooled at 1.9 K with super-fluid He. The cryogenic equipment needed to produce the 100 tons of superfluid helium is unprecedented in scale and complexity for the whole LHC ring.

1.2 The ATLAS experiment

The initials ATLAS come from **A** **T**oroidal **L**HC **A**pparatu**S** and along with CMS are the two biggest general purpose experiments of LHC. ATLAS weighs 7000 tons and has a cylindrical structure with a length of 44 m and a diameter of 25 m following the slope of the LHC. It is divided to the following systems:

- The Magnet System
- The Inner detector
- The Calorimeters
- The Muon spectrometer

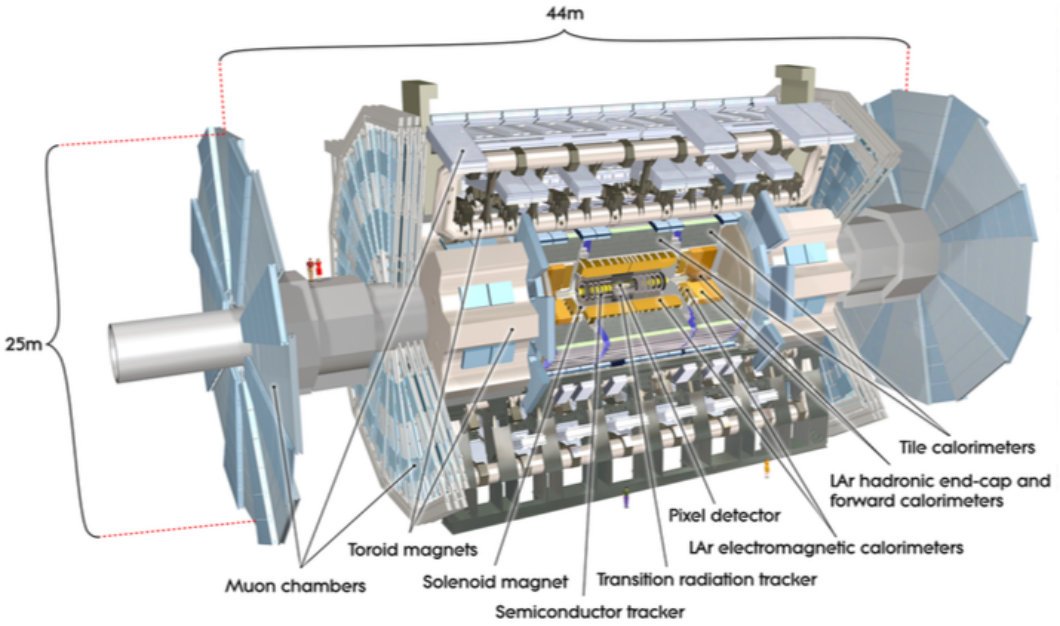

Figure 1.2: A graphical representation of ATLAS

1.2.1 The Magnet System

In order to achieve accurate measuring of momenta of the charged particles which are produced from collisions a magnet field is applied from different layers of ATLAS. The structure of the magnet is based on an inner thin superconducting solenoid [10] surrounding the inner detector cavity and large superconducting air-core toroids consisting of independent coils arranged with an eight-fold symmetry outside the calorimeters.

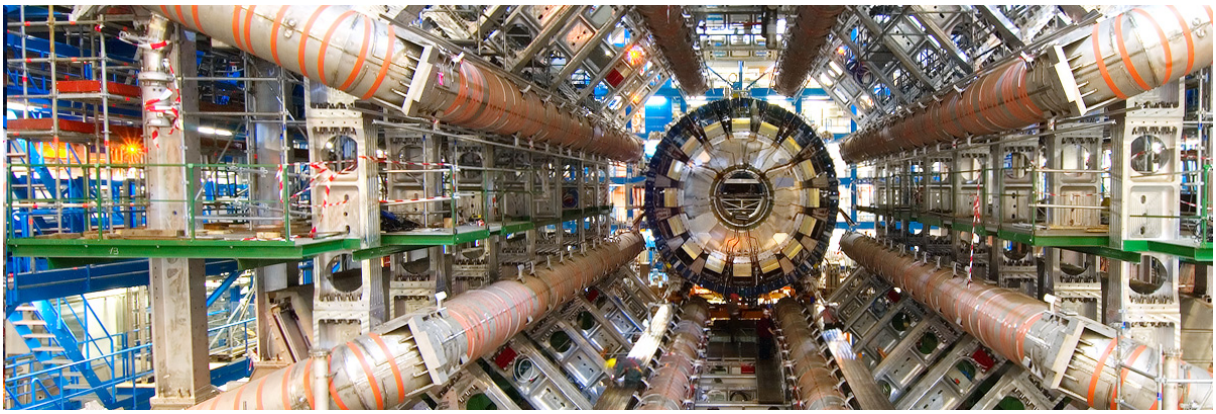

Figure 1.3: The ATLAS magnet system

The inner thin superconducting solenoid provides a field of 2 T for the inner detector by a superconducting solenoid that is integrated into the cryostat of the barrel liquid argon calorimeter. The design aims to minimise the material in front of the calorimeter. The large superconducting air core toroids provides the magnetic field for the muon spectrometer. It consists of a large barrel [11] toroid and two end-cap toroids [12]. The overall length is 26 m and the diameter is 20 m.

The magnet field has a 3.9 T peak for the barrel and 4.1 T for the end caps. In figure 1.4 there is a graphical representation of the three systems. The maximum field is observed in the region where the superconducting matter of the system corresponds to the central solenoid and barrel/end-cap toroids. The resultant field intensity, summing up the different contributions, is not uniform along the detector volume. An example map of the field intensity as a function of the radial distance from the axis and along the z direction for a specific cross-section in ϕ, ($\phi = \pi/8$) is figured in the 1.4 where we see the central solenoid installed in the liquid argon calorimeter cavity (blue colour) encircled by the barrel (red colour) and the end-cap (green colour) toroid coils.

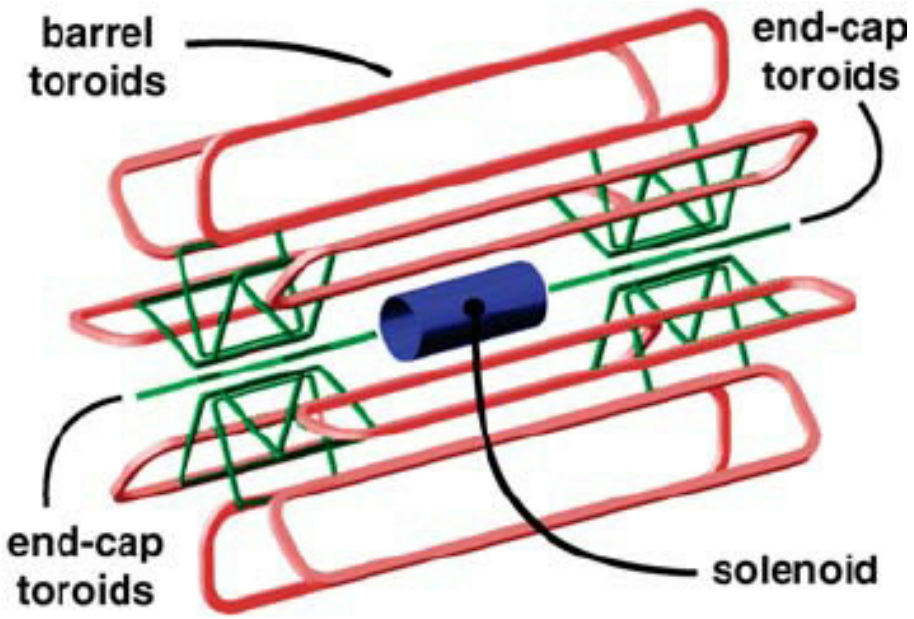

Figure 1.4: Graphical representation of the Atlas Magnet System where we see the three main parts

1.2.2 The Inner Detector

In the inner part of the detector [13] there is a combination of three different detector systems that cover the pseudo-rapidity of the range of $|\eta| \leq 2.5$. The ATLAS inner detector (ID) [14] which consists of the silicon Pixel Detector(Pixel), the Semi - Conductor Tracker (SCT) and the Transition Radiation Tracker(TRT). ID has

detectors of high resolution which cover the tracks of charged particles.

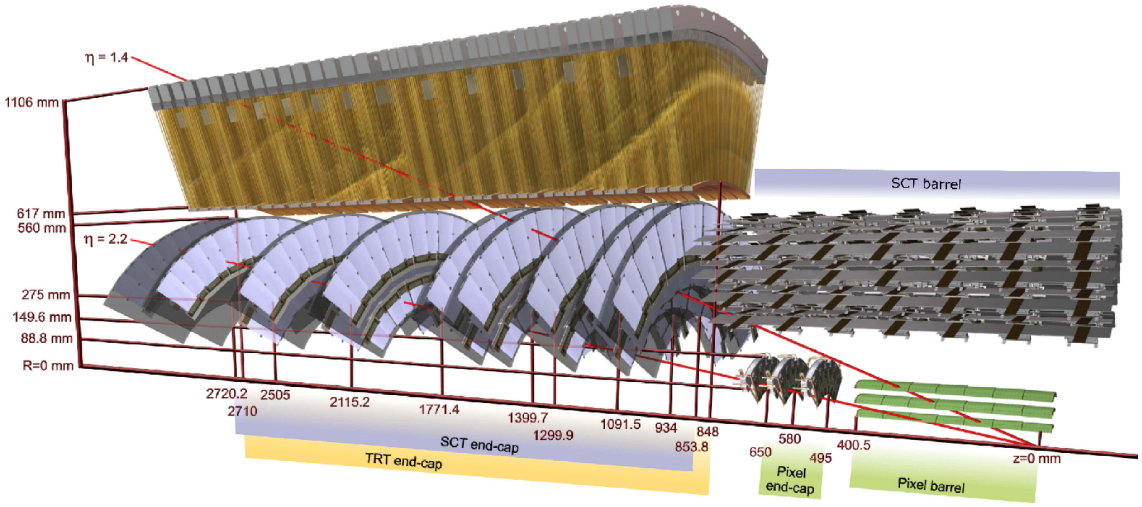

Figure 1.5: Graphical representation of the Inner Detector where are seen it's three parts . Distances between the three different detector systems are noticed

It is contained in the inner frame of a cylinder 7 m length and radius of 1.15 m. It can achieve pattern recognition techniques, momentum measurements and identification of electrons. In the centre, the high resolution Pixel detector can provide three space points per track. It is surrounded by the SemiConductor Tracker (SCT), on which silicon strips provide typically four space points per track.

On the outer, a continuous straw-tube layer of tracking detectors with transition radiation capability, called Transition Radiation Tracker (TRT), provide typically 36 measurements per track with high rate capability. The hits of every different system of the ID are recorded and then the trajectories within the Tracker are reconstructed.

The accuracy of the reconstruction is limited by a combination of uncertainty contributions including the finite resolutions of the detector elements, the exact knowledge of the magnetic field, the relative locations of the detector elements and finally the amount of material in the detector.

1.2.3 Calorimeters

ATLAS calorimeters are responsible for high resolution measurements of energy, position and movement of electrons, photons and jets and are having the ability to measure losses of the p_t. Moreover they are capable of particle identification and contribute in the muon momentum reconstruction.

The calorimeter [15] consists of the electormagnetic calorimeter (EM) which covers the pseudorapidity of the region $|\eta| < 3.2$ and the Hadronic Calorimeter (LAr) which covers the pseudorapidity of the region $|\eta| < 1.7$ and the endcaps region $1.5 < |\eta| < 3.2$. The Liquid Argon (LAr) [16] detector has accordion - shaped Kapton electrodes

and lead absorber plates over its full coverage divided into a barrel part and two end-caps.

The hadronic calorimeter uses techniques and devices which are appropriate for the demands of each radiation. The EM calorimeter layer, which is installed closest to the beam pipe, is able to provide very precise measurements of the incoming particles position and the deposited energy, based on their electromagnetic interaction with its material. The barrel EM calorimeter's energy - absorbing materials are lead and stainless steel, with liquid argon as the sampling material.

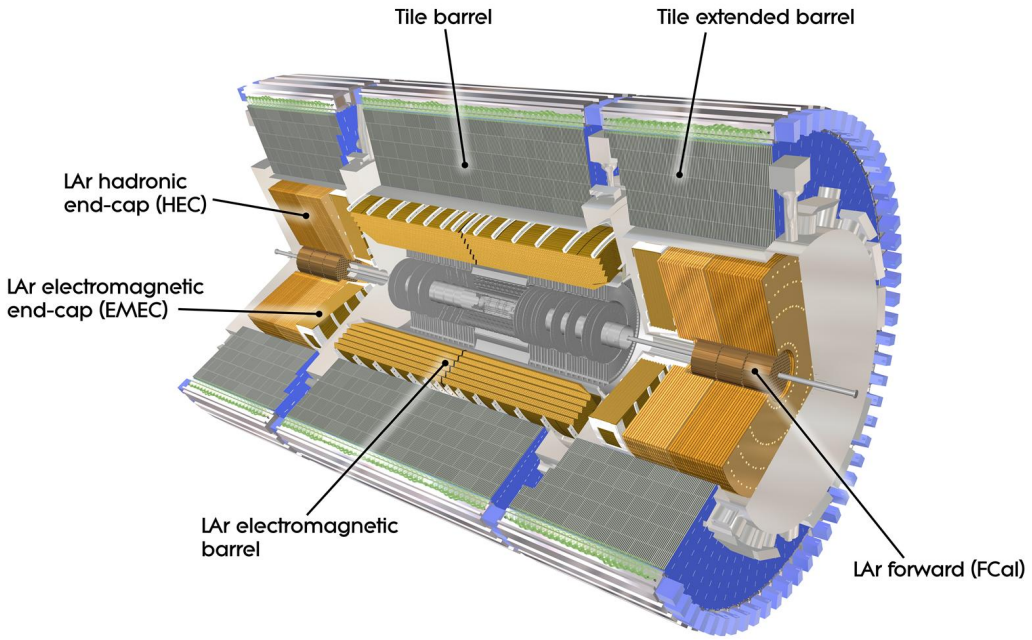

Figure 1.6: Graphical representation of the ATLAS calorimeter where the main parts are noticed, barrel and end caps.The main part has a length of 8 m and covers a region of 12 m

The hadronic calorimeter absorbs energy from particles that interact via the strong force (primarily hadrons) and pass through the EM calorimeter and it is less precise, both in energy magnitude and in localisation. The energy - absorbing material is steel, with scintillating tiles that sample the energy deposited. Many of the features of the calorimeter are chosen for their cost-effectiveness, the instrument is large and comprises a huge amount of construction material. The far-forward sections of the hadronic calorimeter use liquid argon for sampling as well, while copper and tungsten are used as absorbers.

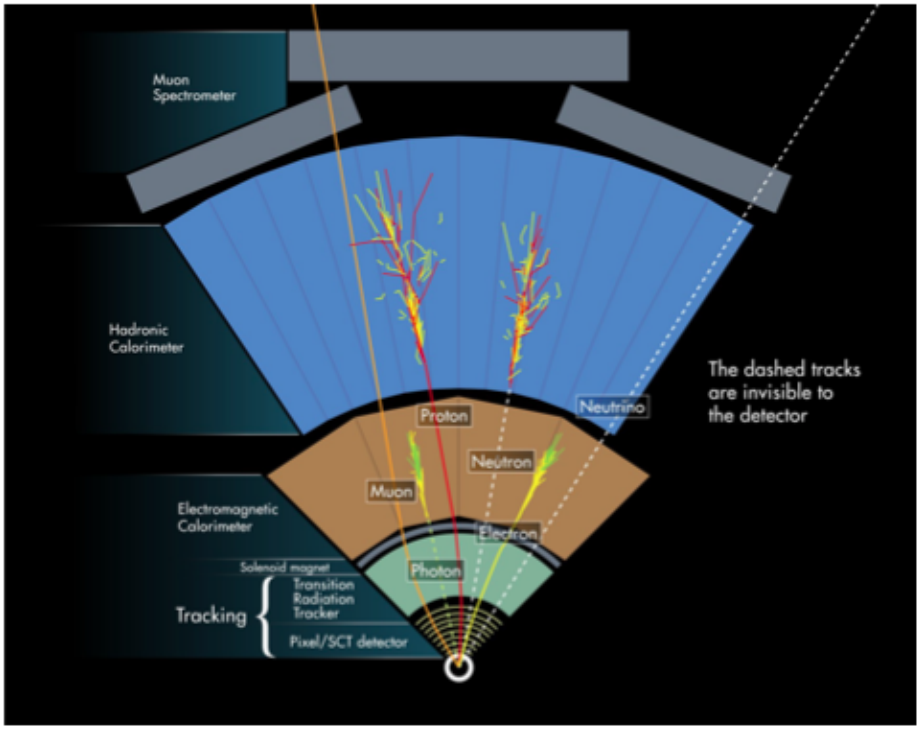

Figure 1.7: The ATLAS working principle. The Magnet systems, inner detector and the calorimeters along with the muon spectrometer are represented.

1.2.4 The Atlas Muon Spectrometer

The representation of the Muon spectrometer [17] is in figure 1.8. The chambers are in such position that particles from IP come through three detection areas. The four different systems used for the respective areas of the muon spectrometer are:

- Cathod Strip Chambers (CSC) for pseudorapidity of region $2.0 < |\eta| < 2.7$
- Monitor Drift Tubes (MDT) cover three detection layers for pseudorapidity of $|\eta| < 2.0$ and two detection layers for $2.0 < |\eta| < 2.7$
- Resistive Plate Chambers (RPC) for pseudorapidity $|\eta| < 1.05$
- Thin Gap Chambers (TGC) for pseudorapidity $1.05 < |\eta| < 2.7$

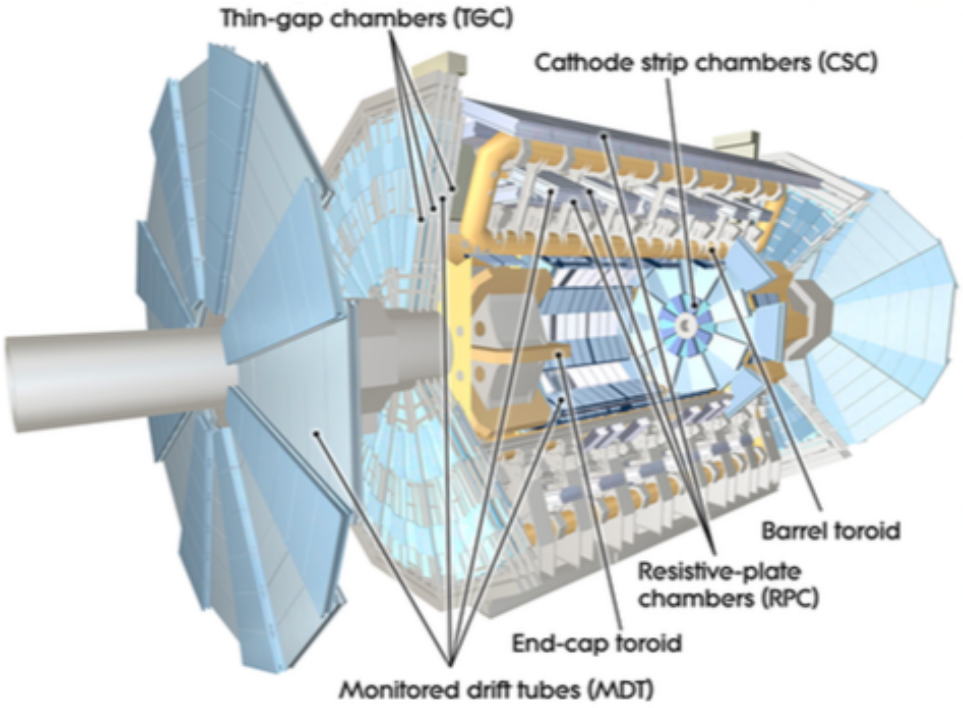

Figure 1.8: Graphical representation of the ATLAS Muon spectrometer detector technologies.

CSC and MDT chambers are very useful for high resolution position measurements while RPC and TGC chambers are used for trigger. MDTs cover the 99.5% of the tracking region and give to us information for particle flux parallel to the beam axis but no timing resolution of bunch crossing. Also cannot give information for flux not parallel to the beam axis. CSC chambers can give us this missing information and cover a very small region in the centre where we get the biggest particle flux.

Trigger operation is performed from RPC chambers in the barrel region and TGC at the end caps.Those detectors have really fast timing resolution of few ns and they contribute to level-1 trigger and BC identification. Beside trigger operation these detectors are used for pattern recognition and use algorithms for the reconstruction of trajectories. High space resolution is needed such as 5-20 mm and they are in place to measure not parallel to the beam axis trajectories. Muon spectrometer is placed in a way which occurs from the process of improving and takes into account different requirements for better detector output. The muon chambers set-up is such that particles from IP come through three layers of position tracking and three of the trigger.

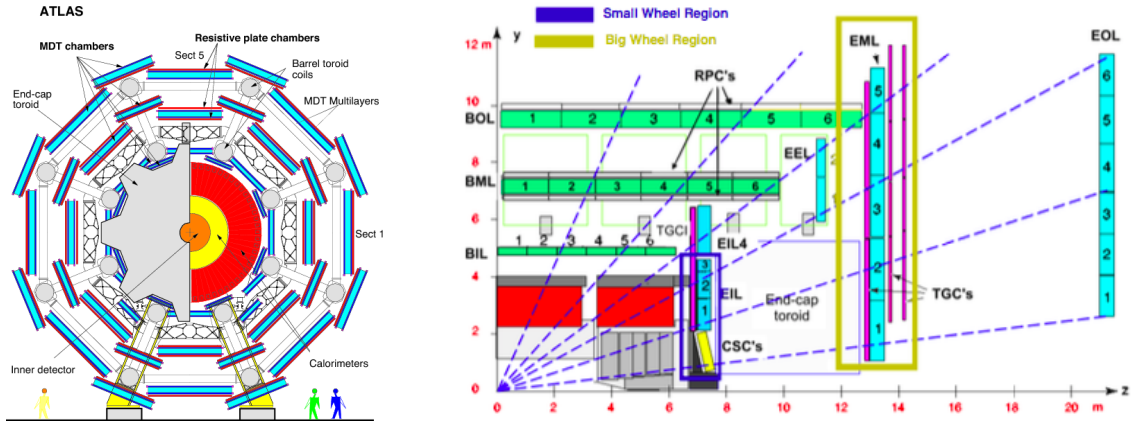

(a) (b)

Figure 1.9: A representation of the ATLAS Muon spectrometer .On the left side we see the barrel and on the right side we see different types of detectors

In order to take advantage of the spatial resolution our detectors provide and a cooperation between them to be efficient there is an alignment process [18]. Firstly there is a non-stop monitoring system for this reason. Both optical and temperature sensors can find the relative placements between the chambers and then the software correction is applied for the misalignments. The alignment process can be divided in internal and global. Each chamber has sensors that control and align the alterations and then the global system shows the misalignments of all the chambers.

The types of sensors are both optical and thermal. Optical sensors are either a RASNIK (Red Alignment System of NIKHEF [19]) or a pair of BCAM laser diodes (Brandeis CCD Angular Monitor[20]) used as reference points are monitored to a Charge-Coupled Device (CCD). The end cap devices are controlled by the Long Wire Data Acquisition system (LWDAQ) [21].

Monitor Drift Tubes (MDT)

Monitor Drift Tube Chambers consist of aluminium pipes of 30 mm diameter and a 400 μm wall thickness with a 50 μm diameter central wire.The tubes use a gas mixture of Ar + 7% CO_2 at 3 bar pressure.

The tube length varies from 70 cm up to 630 cm. They are arranged in multilayers of three or four tube layers on either side of a support structure. They consist of two multi-layers of drift tubes separated by a support frame.

Each multi-layer combines three layers of tubes with the exception of the inner stations of the muon spectrometer (small radius) where one additional layer of tubes is used in each multi-layer enhancing the pattern recognition performance in the high background rates of this region. Each drift tube is read out at one end. The potential applied to the centre wire is around 3080 V. The space resolution of each chamber

after calibration and corrections needed due to the magnetic field is 80 μm.

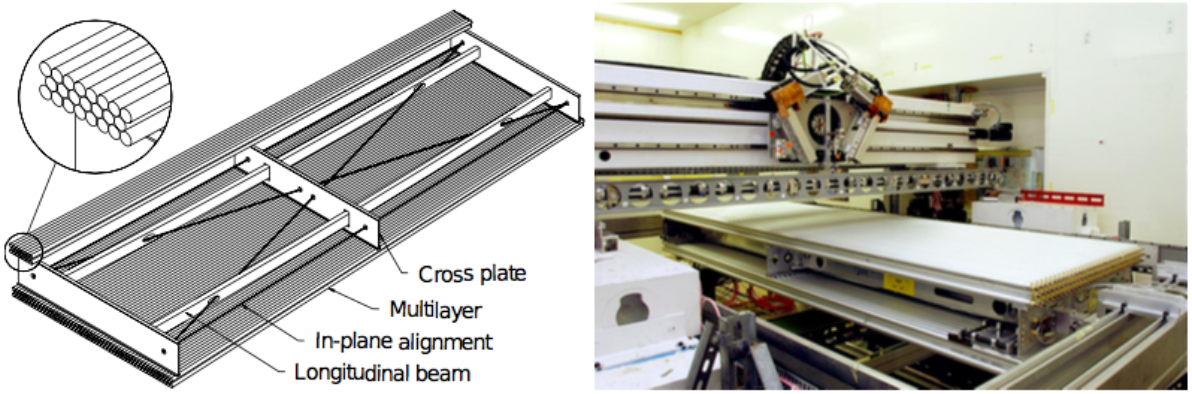

Figure 1.10: Graphical representation of the MDT chamber and the chamber during the construction process

The Cathode Strip Chambers(CSC)

The Cathod Strip Chambers are proportional chambers with cathode strip readout and a symmetric cell in which the anode-cathode spacing is equal to the anode wire pitch. The precision coordinate is obtained by measuring the charge induced on the segmented cathode strips by the avalanche formed on the anode wire.

The cathode strips are oriented orthogonal to the anode wires. CSCs are arranged in four layers equipping only the small wheel in a segmentation of 16 sectors per wheel, as seen in figure 1.11. They are operated with a gas mixture of Ar+20%CO_2 at atmospheric pressure. They are located in the inner side of Small Wheel at the end caps region. Due to the two layer read outs CSCs are able to id positions of particles not parallel to the beam plane. They can also collect ionised electrons in less than 30 ns.

The Cathode Strip Chambers (CSC) measure the position of hits using a nearly orthogonal layout of anode wires and cathode strips. The cathode strips run radially away from the beam pipe and are used to measure the ϕ position of the hits whereas the anode wires determine the radial position.

The signal produced in both the strips and the wires can be used to determine the timing of a hit with similar resolution. When the gas in a CSC chamber is ionised electrons drift towards the anode wires which are kept at a high voltage. The charge collected on the anode wire is input into a constant fraction discriminator in the Anode Front End Board (AFEB) [22].

The ionized electrons induce a charge on the cathode strips which is amplified, shaped, and then sampled every 50 ns. Eight 50 ns samples are saved with the first two bins serving as dynamic pedestals. The sample with the largest charge along with the sample before and two after are used to determine the time of the hit.

Both the anode wire and cathode strip times are corrected for time of flight from the IP assuming straight line speed of light travel. Additionally a propagation delay correction is applied to the cathode strip time based on the location of the hit along the strip.

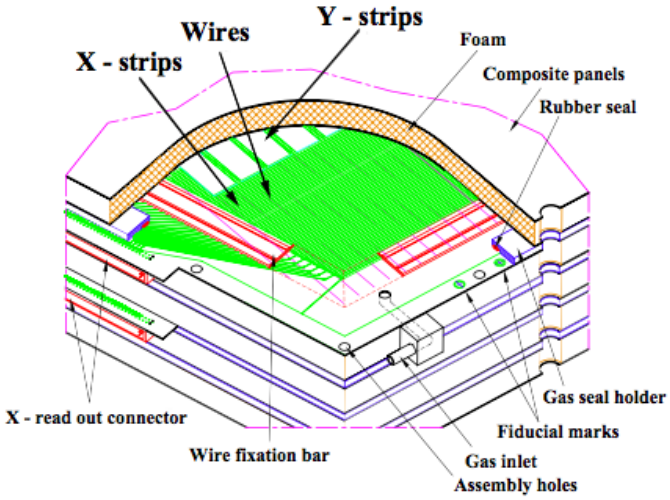

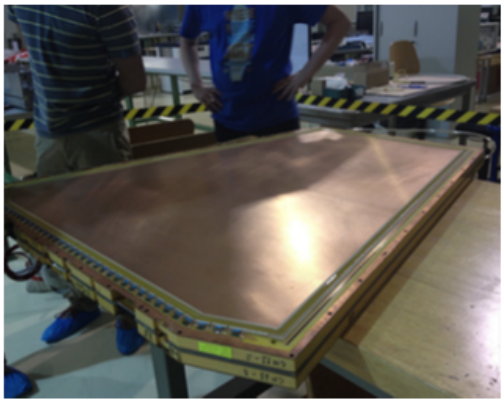

Figure 1.11: Representation of the chamber and a CSC chamber during a service operation

Resistive Plate Chambers(RPC)

In the barrel region ($|\eta| < 1.05$) of the muon spectrometer the RPC chambers are responsible of the trigger signals. The RPC chamber is a gas detector with parallel plates and has a high timing resolution of the 1 ns. This is within the ATLAS requirements.

RPC chambers have a mix of many gases $C_2H_2F_4$:4,5 % – C_4H_{10} :0,3 % SF_6 . Moreover due to their fast timing RPCs are able to measure the BC identification. Also can track the hits from precision chambers which are related with the muon trajectory. The set-up of the RPC system for maximum performance of the trigger and the barrel consist of three stations each on having two precision layers.

Two middle stations have a lever of 50 cm within and are close to the centre of the region of magnetic field and provide trigger for low momenta muon particles while in the third station in the outer layer of the magnet due to the threshold, the trigger for higher momenta muons.

Thin Gap Chambers(TGC)

Thin Gap Chambers cover a pseudorapidity range of $1.05 < |\eta| < 2.07$ (barrel region). They provide the trigger information for the end caps. Combining the information from the MDT chambers they provide measurement of the azimuthal

coordinate. The middle end-cap station of the MDT is complemented by seven layers of TGC, which provide both triggering and azimuthal coordinate measurement while the two layers of TGC in the inner muon end-cap (SW) measure the azimuthal coordinate.

TGCs are similar to the Multi-Wire Proportional Chambers with anode wires enclosed by two graphite cathode layers and two layers of readout strips running perpendicularly to the wires.

They are operated with a highly quenching gas mixture of $CO_2 + 45\,\%\, n - C_5H_{12}$ and a very intense electric field (3200 V) to satisfy the time, momentum, and azimuthal coordinate resolution requirements while making the performance of large surface chambers insensitive to mechanical deformations. The very good timing resolution guarantees the BC identification capability of the TGC.

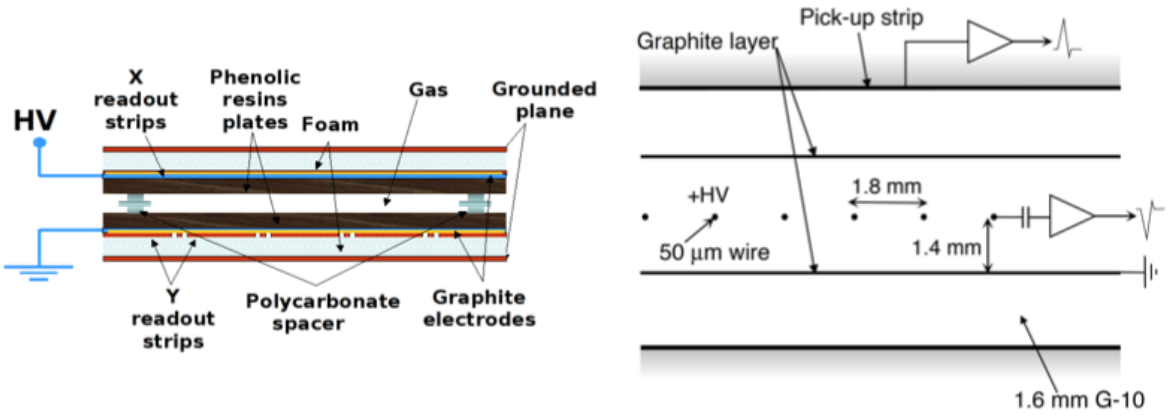

Figure 1.12: The cross section of an RPC chamber and a drawing of the TGC internal structure

1.3 The ATLAS New Small Wheel Upgrade Project

In the 2010-2012 (Run-1) period, LHC was able to deliver us the last missing part of Standard Model, the Higgs Boson [23], [24]. Run-1 period was followed by the Long Shutdown 1 (LS1) period which lasted two years. After the upgrades performed during LS1 , Run-2 operated with the centre of mass energy of 13TeV .

Luminosity was at $\mathcal{L}= 10^{34}\ cm^{-2}\ s^{-1}$ level and after LS2 it will increase at $\mathcal{L}= 2\times 10^{34}\ cm^{-2}\ s^{-1}$ [25]. Towards the installation of the HL-LHC where the luminosity will be further increased after the end of Run 3 experimental set-ups must be upgraded. The New Small Wheel will operate from 2019 until 2032.

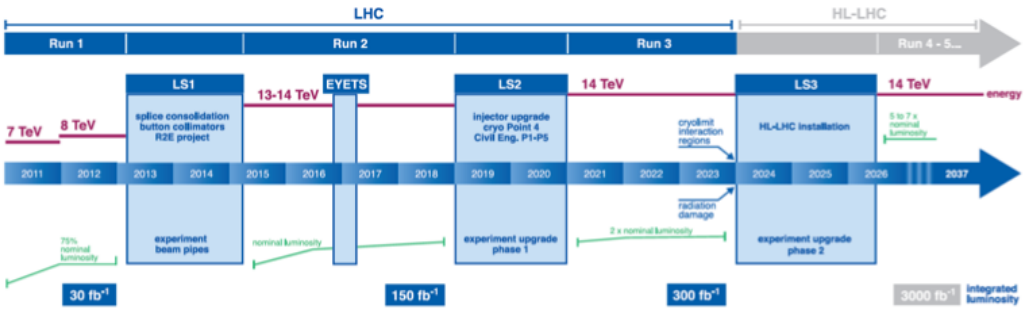

Figure 1.13: The LHC schedule

After the peak luminosity increases, ATLAS and CMS experiments will have also to be upgraded. Especially the ATLAS detector will be upgraded in two steps: Phase-1[26] in the LHC shutdown 2018/19 and Phase-2 [27] in 2023-25. ATLAS phase-1 upgrades focuses in the inner end-cap of the muon spectrometer the Small Wheel(SW). Small wheel has three detector types at the moment CSCs, MDTs and TGCs , figure 1.14 .

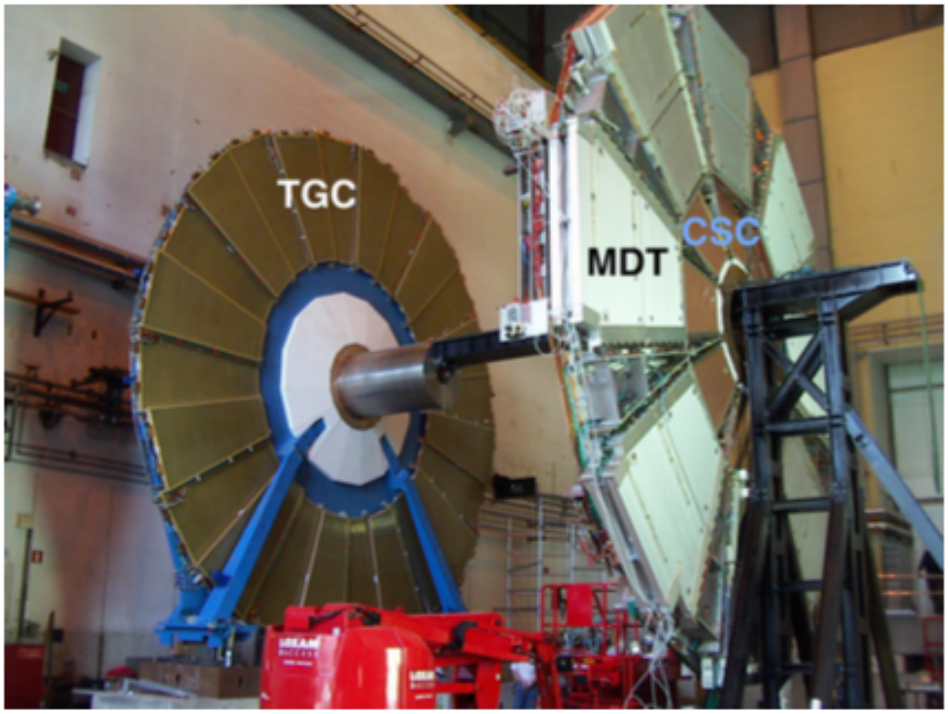

Figure 1.14: Small Wheel at the current set-up

During the period between LS2 and LS3 the expected number of inelastic interactions per bunch-crossing is estimated to be 60 to 70 and after LS3, up to 140. This excesses the current efficiency of the SW.

This is of main importance since the end-cap region of ATLAS covers 63% of the muon system rapidity. So in both trigger and tracking measurements limits of the current set-up cannot cover the increased rates, especially since background rates are a main part of :

- End-Cap Muon Trigger cannot cover the rate of particles from the forward direction
- Muon tracking capacity will be downgraded

The end cap Level-1 muon trigger takes data from the TGC chambers of the Big Wheel located after the end-cap toroid magnet. End cap Muon triggers are dominated by fake hits due to background. As mentioned before background is a main part of the muon trigger rates. The material between the SW and end Big Wheel, produces low energy particles, mainly protons, which hit the BW at the same angles real particles do, producing the so called "fake triggers" as shown in figure 1.15 .

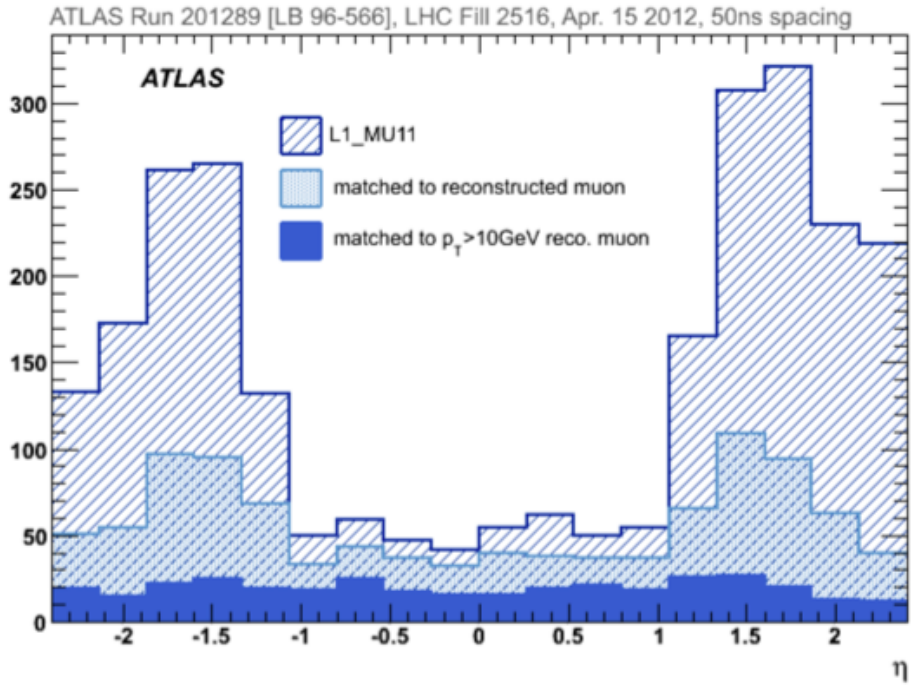

Figure 1.15: η distribution and number of Level-1 muon candidates.

The dashed distribution shows trigger rate of the muon system with $p_t > 10\ GeV$. Adding threshold of $p_t > 10\ GeV$ (dark blue distribution) almost eliminates the fake end cap muon triggers [28]. Fake triggers are almost 90% of the total number.

In order to overcome the fake triggers problem the SW will be upgraded in the New Small Wheel (NSW) during the LS2. NSW will combine two detector systems sTGC chambers and Micromegas (MM) detectors [29]. Main target is to improve transverse momentum measurement and to discriminate against background while maintaining the low transverse momentum threshold [30] .

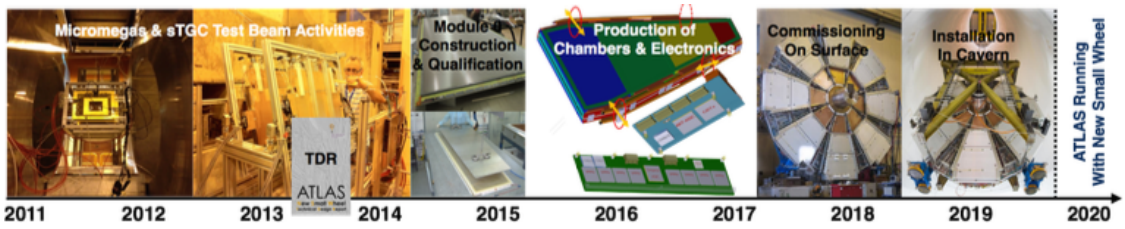

Figure 1.16: The NSW update schedule

1.3.1 Project requirements

As said above NSW will have both sTGC and MM chambers. Main principle is that the new systems will combine high efficiency in both low and high rates of particles high luminosity dictates. NSW must provide trigger information without background fake triggers affecting it's performance as shown in figure 1.17.

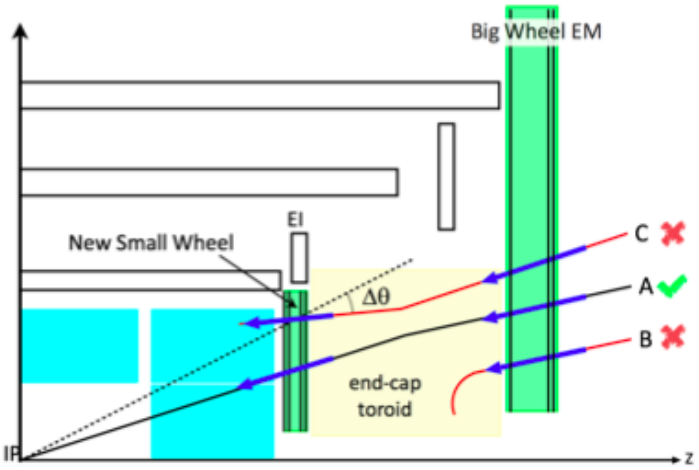

Figure 1.17: Trigger coincidence of SW and BW. A detector at the end-cap can provide BW trigger logic keeping the real candidates and removing fake.

The reconstruction of tracks for the region of rapidity $1.3 < |\eta| < 2.5$ is better than 1 $mrad$ and the rate will be reduced to 20 kHz matching the requirements of ATLAS trigger rate for muon system. For the luminosity of $\mathcal{L}$= 10^{34} cm^{-2} s^{-1} rates were predicted to be 100 kHz [31]. Trigger rates will be reduced five times as shown in

figure 1.18. Also segment reconstruction will be executed within a maximum latency of 1 μsec.

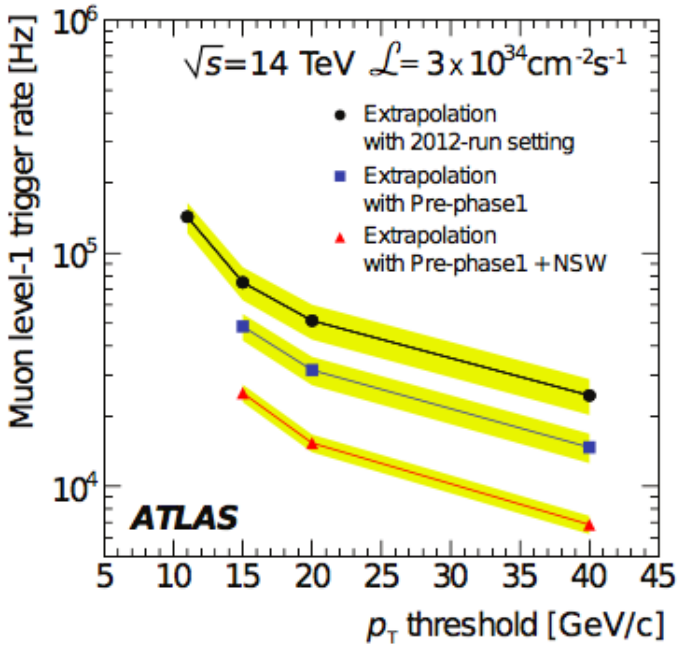

Figure 1.18: Expected Level-1 muon trigger as a function of p_τ threshold. The red configuration shows that expected trigger rate will be reduced significantly.

1.3.2 Detector Technologies of the NSW

NSW will be a match for the current SW and detectors on it, which will cover a detector area of 1200 m^2 for each wheel. Will consist of detector planes with two detector systems the small-strip Thin Gap Chambers (sTGG) and the Micro-Pattern Gaseous Detectors the so called Micromesh Gaseous Detectors (Micromegas). Small TGC chambers are used mainly for triggering and Micromegas for tracking.Each wheel is segmented in 16 sectors.

Small-strip Thin Gap Chambers (sTGG) are used primarily for triggering capabilities. TGC detector has single bunch crossing identification capability. The beam Bunch Crossing frequency is 25 ns. sTGC chambers are capable of producing data within this time and are also good for spatial recognition due to their small strip pitch ($3,2$ mm). The signal due to ionisation charges is induced on the anode wires, readout pads and strips behind cathode planes.

Micromegas detectors are used for their tracking capabilities with spatial resolution less than 100 μm but also timing resolution of less than 10 ns. They have small drift gap of 5 mm and strip pitch of 0.4 mm-0.25 mm depending on the set-up. Earliest arrival time in every Bunch crossing for the NSW MM chambers will be used as

trigger. As the main subject of this thesis is MM detectors they will be further analysed in the next chapter.

The layout of the NSW

NSW is a match for the current SW so it's dimensions will be on par with it . Each wheel will have 16 sectors of small and large scale covering it's full size. Every sector consists of 8 layers separated by a spacer of 50 mm. So as the sTGC detectors will be used for triggering will be fitted in the outer layers of the frame while MM detectors the inner part. Micromegas will not be visible sitting between the sTGCs. Any technology primary abilities compliments the other and full fill the requirements of the upgrade.

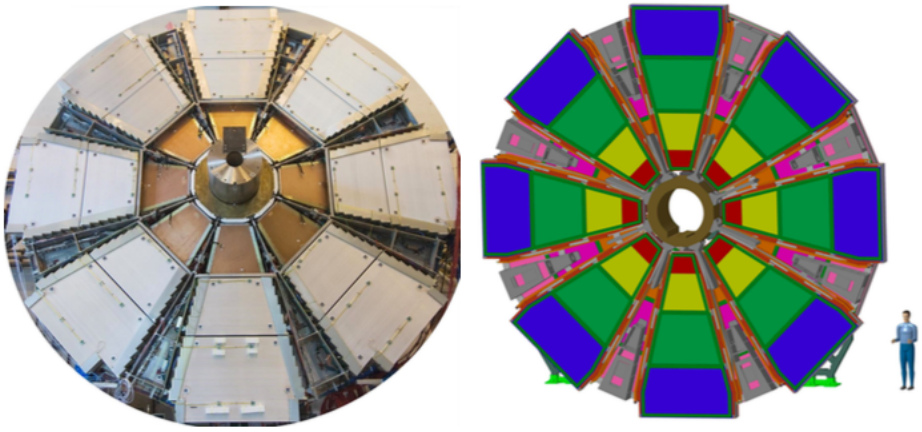

Figure 1.19: Current SW and a graphical representation of the NSW

As seen in figure 1.19 the NSW consists of wedges of each detector type and totally sixteen. Sectors are then segmented in eight large and eight small parts. Large sectors have 450 μm strip pitch and small 425 μm. The sector configuration for each detector type is described below:

MM

LM1, lower radius of the large sectors
LM2, larger radius of the large sectors
SM1, lower radius of the small sectors
SM2, larger radius of the small sectors

sTGC

QL1, lower radius of the large sectors
QL2, medium radius of the large sectors
QL3, larger radius of the large sectors
QS1, lower radius of the small sectors
QS2, medium radius of the small sectors
QS3, larger radius of the small sectors

Each sector consists of 2 wedges. Each wedge is a stack of chambers combining four detection layers of each technology, with the arrangement sTGC-MM-MM-sTGC,

so sixteen detection points per track. The largest possible lever arm between the triggering wedges is achieved with this configuration for better reconstruction of the track. In this thesis data from both SM1 and LM1 prototypes were acquired for analysis.

The MM small sectors configuration is shown in figure 1.20 .

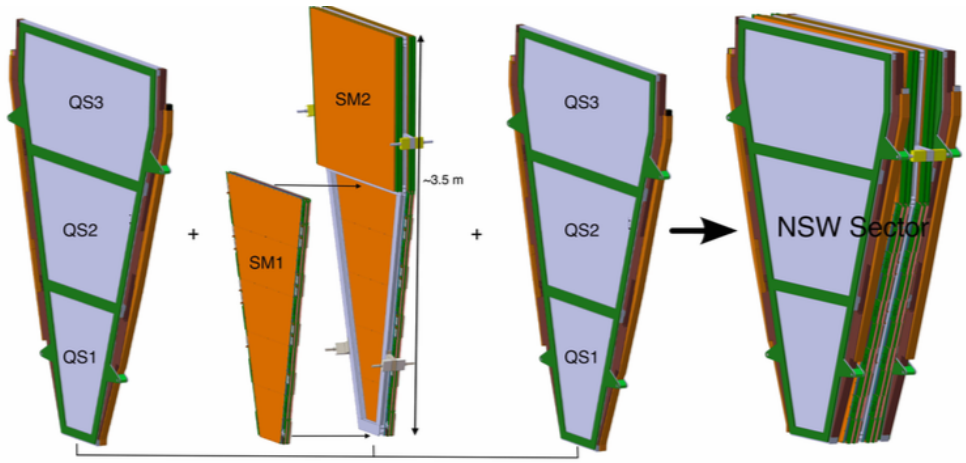

Figure 1.20: Two MM small wedges modules SM1 and SM2 type, mounted on both sides of the inner frame and then framed by two sTGC quadruplets

Each micromegas layer is segmented in eight PCB boards. The upper modules contain three boards while the lower five boards. Finally PCB readout boards contain of 512 readout strips.

CHAPTER 2

INTERACTION OF CHARGED PARTICLES WITH MATTER-THE MICRO MESH GASEOUS DETECTOR

Particle detectors operate through the interactions of particles with matter. In this section the basic attributes of this operation are going to be described then how particles interact with the medium and the way signal is propagated. Then some main principles and processes that will give us better understanding of the Micromegas detector a latest generation gaseous detector which as described before is the main particle tracking system for the NSW upgrade.

2.1 Premier interactions of charged and neutral particles with matter

Charged particles incoming through a detector interact with the medium of it giving a signal. Electromagnetic interaction is the main process in which detectors are based. Especially in ionisation gaseous detectors charged particles interact with the gas of it. When a charged particle is passing through the medium it generates positive ions and electrons.

Particles are losing energy through the material and two types of reactions then happen stimulation and ionisation. For this to happen excitation energy given to the molecule should be appropriate for the quantum leap propagating a coordination reaction. For noble gasses the cross section σ, has values of around 10^7 barn. In this way not ions and electrons are produced but the excited molecule can participate in further reactions leading to ionisation.

In the case of ionisation specific action is not required but enough energy to exceed a threshold value. The electrons and ions produced are the primary ionisation. In some of these ionisations electrons can take quite energy value that in turn cause further ionisations. These are called secondary ionisations. The ionisation products

are the primary tool for the detection.

2.1.1 Neutral particles

Due to the movement of particles through the detector, electrons may loose energy radiating photons. Neutral particles are detected not directly but from their interactions in the gas of the detector. The produced photons can interact with the following processes:

- **Photoelectric absorption**: A low energy photon is absorbed by an atomic electron and a photoelectron is ejected from one of the atom's boundary states (as in K shell). The ion is filled through the absorption of a free electron or by the re-arrangement of the atom electrons and the emission of an x-ray photon that is most probably reabsorbed very close to its generation point.

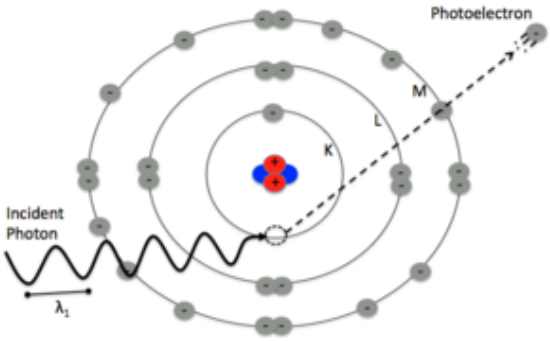

- **Compton scattering**: Inelastic scattering of the photon by an electron in the absorber results in energy transfer to the bounced electron related to the deflected angle of the photon

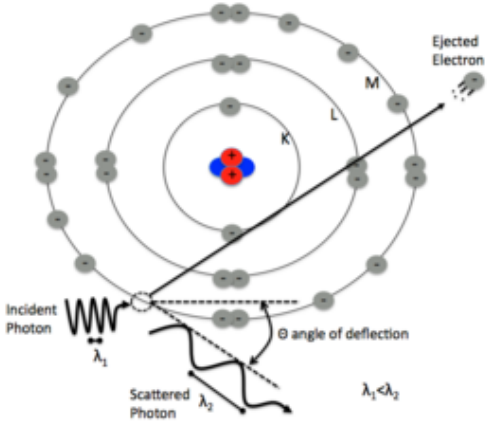

- **Pair production**: When a photon has much larger energy than twice the rest mass of an electron the photon disappears and is replaced by an electron-positron pair

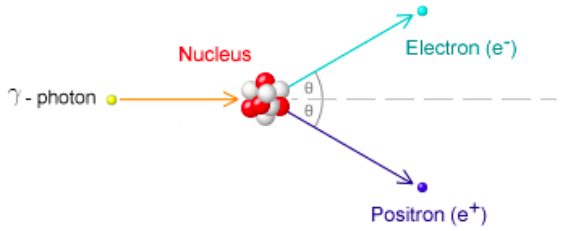

Neutrons which is the other case of neutral particles, produce heavy charged particles from their interaction with the nuclei of the absorbing material. Slow neutrons involve in nuclear reactions while fast neutrons excite the nuclei which de-excites producing gamma ray.

2.1.2 Charged particles through medium

Main attribute of the drift of charged particles through the medium is their energy loss through electromagnetic process. The linear stopping power S through the medium, negative due to energy loss, in an absorbing material is the differential loss divided by the differential path length:

$$S = -\frac{dE}{dx} \tag{2.1}$$

For heavy charged particles ($m_0 \gg m_e$) this is given by the Bethe-Block equation 2.3. The particle's velocity is $\beta = u/c$, I is the mean excitation energy, $K = 4\pi N_A r_e^2 m_e c^2$, $\gamma = E/Mc^2$, z is the charge of the incident particle, Z and A the number and atomic mass of the absorber, m_e the electron mass, r_e the classical electron radius, N_A is Avogadro number and $\delta(\beta)$ is the density effect term :

$$-\left(\frac{dE}{dx}\right) = Kz^2\frac{Z}{A}\frac{1}{\beta^2}\left(\frac{1}{2}ln\frac{2m_e c^2\gamma^2\beta^2}{I} - \beta^2\right) \tag{2.2}$$

Equation 2.3 shows that energy loss decreases as β increases. For particles at relativistic energies almost at speed of light and $\beta \approx 0.95$ the energy loss is at a minimum and $\beta\gamma \approx 3$. A particle at the energy loss minimum is called minimum ionised particle(mip).

The energy increases again due to logarithmic term in brackets and this behaviour is called logarithmic or relativistic rise of the energy. As $\delta(\beta)$ increases more, the atoms close to the trajectory of the incident particle, produce a polarisation such that shield the transverse electric field of the incident particle and the energy loss approaches a plateau. If it wasn't for that term the increase would be unlimited and

this way the energy loss is delimited. This was initially studied by E. Fermi and is called the density effect or Fermi plateau [32]. A correction term $\delta(\beta)$ is introduced into Equation 2.3 to incorporate this effect reaching the following expression:

$$-\left(\frac{dE}{dx}\right) = Kz^2\frac{Z}{A}\frac{1}{\beta^2}\left(\frac{1}{2}ln\frac{2m_ec^2\gamma^2\beta^2}{I} - \beta^2 - \frac{\delta(\beta)}{2}\right) \tag{2.3}$$

By the Bethe-Bloch equation we extract an average energy loss to the atoms of the medium. In gas detectors electrons have the same mass as the target electron mass. Also fluctuations between particles affect each event. So the energy transfer needs other more analytic ways in order to be calculated see [33] .

2.1.3 Ionisation

In gaseous detectors charge particles interact with the medium (gas) in order to produce electron-ion pairs or excited atoms propagated to the detection through electromagnetic interaction.

The electron that was extracted from atom is called the primary electron. If the energy of the primary electrons is high enough, further ionisations will be produced causing secondary electrons.

Total ionisation and per unit path is :

$$n_\tau = \frac{\Delta E}{W_i}$$

ΔE is the deposited energy per 1cm of transversed detector material and W_i is the mean energy required for electron-ion production. From studies in [30] for $Ar + 7\,\%CO_2$ mixture in Micromegas chambers :

$$n_p = 0.93 \times 29.4 + 0.07 \times 34 = 29.7[pairs/cm] \tag{2.4}$$

$$n_\tau = 0.93 \times \frac{2440}{26} + 0.07 \times \frac{3010}{33} = 93.7[pairs/cm] \tag{2.5}$$

W_i is depended from the gas medium, the type and energy of the particle but it was observed that it has a constant mean value for great gas and particle quantities and was measured at 25-35 eV/ion pair. The pairs which have a mean value of n_τ have a Poisson distribution. So if the probability of primary ion pairs is k then:

$$P_k{}^n = \frac{n^k}{k!}e^{-n}$$

then the dispersion of the distribution equals the mean value of numbers of primary ionisation n. Micromegas detectors have a dispersion of 30%.

2.2 Drift velocity

Drift of ionisation products move to the directions their charge determines. Of course, velocity is respectively non proportional to the particles mass. Velocity is also depended on the electromagnetic field applied, temperature and pressure.

2.2.1 Electron drift

Electrons drift faster to the detection plane due to their smaller mass, compared to ions. When electric field is applied to the detector electrons of the primary ionisation drift to the direction of the positively charged electrode called Anode. Also ions larger mass leads to big energy losses through gas interactions. Within a medium of magnetic field B where $-(m/\tau)u$ is the friction free force fow slow down effect of electrons, τ the average time between collisions and electric field E, motion is described by Langevin equation [34]:

$$m\frac{du}{dt} = e(E + u \times B) - \frac{m}{\tau}u \tag{2.6}$$

If drift velocity is constant we get:

$$|u_d| = \frac{e\tau E}{m\sqrt{1 + (\omega\tau)^2}} \tag{2.7}$$

$$\tag{2.8}$$

If no magnetic field is applied then $\omega\tau = 0$ and:

$$|u_d| = \mu E \tag{2.9}$$

2.2.2 Ion drift

Of course it is anticipated that due to their large mass ions drift slower than electrons through the medium. When the field is applied ions drift to the direction of the cathode. So the electric field applied is proportional to ion velocity. When the ion of a mass m, interacts with gas molecules mass M the coefficient f which expresses the energy loss is :

$$f = \frac{2mM}{\sqrt{(m+M)^2}}$$

If their mass is equal then $f \approx 1/2$ and $f \approx 10^{-3}$ of electron atom collision. The mean drift velocity of ions is:

$$u_d^{ion} \simeq \left(\frac{1}{m+M}\right)^{1/2}\left(\frac{1}{3kT}\right)^{1/2}\left(\frac{eE}{N\sigma}\right) = \mu E \tag{2.10}$$

Where T is temperature, N is density, k is the Boltzmann's constant σ is the cross section of the ion-gas molecules interaction and μ is ion mobility. The mobility value can be considered constant in stable environment.

2.2.3 Macroscopic view and diffusion of ion and electron drift

As mentioned above ion and electrons move to the directions of cathode and anode respectively. Through collisions the gas molecules have a mean drift value. The mobility coefficient μ is then $\mu = u/E$, u is the drift velocity and E the electric field. After the thermal equilibrium of gas molecules we can derive the diffusion coefficient D from equation 2.11 called Einstein equation:

$$\frac{D}{\mu} = \frac{kT}{e} \tag{2.11}$$

For electrons we can consider a linear drift with higher mobility of course. It depends from the electric field E and can reach an upper limit. In this case it remains constant. Velocity up to 10^6 m/s can be achieved and in this case E is in the 1 kV/cm range. Then diffusion coefficient D is increased and directs electrons in higher dispersion [35]. From the Kinetic theory we can exact the number of charged particles N, position x, after time t :

$$\frac{dN}{dx} = \frac{N_0}{\sqrt{4\pi Dt}} exp\left(-\frac{x^2}{4Dt}\right) \tag{2.12}$$

N_0 is the number of all charged particles,x the coordinate of position and D is the diffusion coefficient.The rms is then:

$$\sigma(x) = \sqrt{2Dt} \tag{2.13}$$

In a case of three coordinates we have radial diffusion coefficient $\sigma(r)$.So $r = \sqrt{x^2 + y^2 + z^2}$ and

$$\sigma(r) = \sqrt{6Dt} \tag{2.14}$$

The diffusion coefficient is derived from Kinetic theory:

$$D = \frac{1}{3} u\lambda \tag{2.15}$$

where λ is the mean free path of the charged particle in the gas.λ is :

$$\lambda = \frac{1}{\sqrt{2}} \frac{kT}{\sigma_o p} \tag{2.16}$$

σ_o is the cross section for a gas molecule and the diffusion is then:

$$D = \frac{2}{3\sqrt{\pi}} \frac{1}{\sigma_o p} \sqrt{\frac{(kT)^3}{m}} \tag{2.17}$$

2.3 Avalanche and Signal formation

2.3.1 Gas multiplication

The primary electrons, so called first ionisations products, drift to the electrodes of the Anode through the gas. When their energy exceeds a sufficient value due to the affection of the field, they can create further ionisations in the gas. Secondary electrons, if energy is sufficient, will do the same and this goes on and on. So by this effect we have a production of ion-electron pairs and the formation of the avalanche. Electrons drift faster so the avalanche is shaped like a drop. In the front "head" side electrons are moving along while in "tail" we see the slower ions.

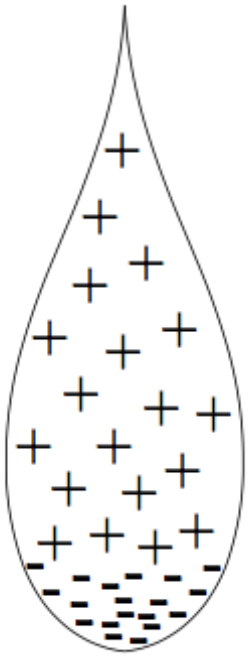

Figure 2.1: The drop shaped avalanche formation

If we consider λ the mean free path of the electron between two collisions then the coefficient $\alpha = 1/\lambda$ is the ionisation probability per length. This is called first Townsend coefficient. This equals to N the density of electrons and σ_1 the ionisation cross section per electron. For a number of n electrons in path dx we will have further dn electrons:

$$dn = nadx \tag{2.18}$$

So from equation 2.19 we can derive the number n of electrons, in the path x:

$$n = n_o e^{ax} \tag{2.19}$$

The n/n_o is the multiplication factor or as we call it the gas gain. If the Townsend coefficient a becomes a function of distance, in case of non uniform electric fields, the gas gain is:

$$M = exp\left(\int_{r_1}^{r_2} a(x)dx\right) \tag{2.20}$$

The gas gain depends from the gas mixture we use. The upper limit or Raether limit is 10^8 and further than this limit we have sparks. In the Micromegas chamber we have primarily Ar but this alone cannot give a gas gain bigger than $10^3 - 10^4$.

This happens because excited Ar molecules and other noble gases are de-excited producing a photon with ionisation energy higher than the ionisation potential of the Cathode or Anode metal. The photon of 11.6 eV from the Ar detaches electrons from the copper strips in the Micromegas case (copper strips have extraction energie of 7.7 eV) so the new ionisations from all those electrons create avalanches. So the detector is currently leaked from current and further gas gain cannot be achieved.

For this reason we use low quantities of a polyatomic gas in the detector. Those molecules are called quenches cause they absorb photons in a widespread energy volume without producing further photons. In the micromegas the gas used is Ar+ 7% CO_2. Because of those chemical reactions the volume of the gas is decreased and for this reason there must be a continuous flux of this gas mixture in the chamber.

2.3.2 Signal formation

As we described the avalanche is induced to the electrodes of the detector. Of course electrons and ions drift towards opposite directions due to the electric field. Electrons drift faster because of their smaller mass and within a few nanoseconds reach the anode very fast and induce a very small signal while the ions of the avalanche with a velocity two to three orders of magnitude less than this of electrons, induce charge on the electrodes with hundreds of nanoseconds duration. The method generally used to calculate the charge induced on an electrode is done by using the Shockley-Ramo theorem [36],[37] and the concept of weighting field. In the case of a charge q moving with a drift velocity u_{drift} the induced current at an electrode will be:

$$i(t) = qu_{drift}E_w \tag{2.21}$$

Where $E_w = - \bigtriangledown \psi_n[\mathbf{x(t)}]$ is the weighting field and $u(t)$ is the drift velocity of the point charge.

2.4 The Micro Mesh Gaseous Detector

In the previous subsections of this chapter we described the interactions of the charged particles with mediums and gave specific details. This was done so as the reader will

be able to understand these interactions that are the main principals gas detectors manipulate to operate in order.

Gaseous detectors were introduced many years ago but the evolution of this technology remain an important tool for many areas of physics. We will focus to their use in high energy physics and mostly to the MicroMegas detector for the NSW upgrade which was the detector for the data used in this thesis.

2.4.1 Gaseous Detectors

As said in the introduction of this section, gaseous detectors are used over the past century in a very large scale of experiments. They mainly operate through interaction of the charge particle with the medium of the detector, in our case the gas.

Gas counters are separated in regions of operation according to the voltage they operate. This is for detectors working in pulse mode which means the detector is eligible to take inventory of all the particles that interacted and provide amplitude and timing measurements.

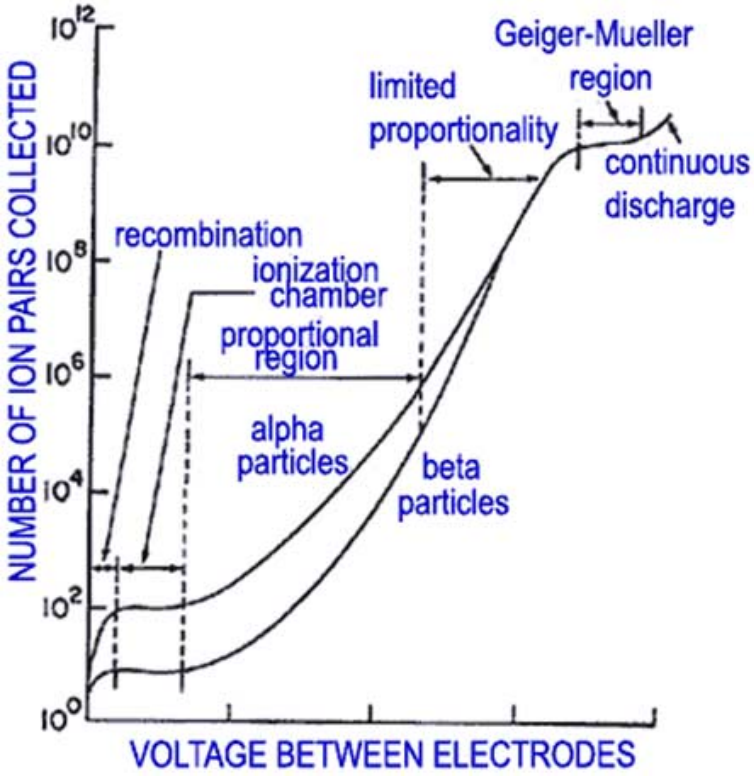

Figure 2.2: Gaseous detectors regions as a function of high voltage.We see the regions and ammounts of energy for two different types of radiation

In figure 2.2 we see the distinguished areas. In the low voltage area particles

cannot be collected from the electric field. That is happening because the field is not strong enough to attach the ion - electron pairs before they are reattached.

This can be achieved by increasing the electric field as seen happens in region II. It is called the nominal region of operation for ionisation chambers. If higher electric field is applied we move to region III, the proportional region. This is the region for proportional counters like the Micromegas chambers. In this area the ion-electron pairs are able to produce further interactions within the gas, creating avalanches and amplification of our signal. In region III there is a linear correlation of the applied voltage to the pairs created.

With the further increase of the field this proportionality is no longer in the same rate and is called the Region of limited proportionality. Electrons in this area are collected faster than positive ions. Due to the further applied voltage and larger number of ions the positive ion space is so big that creates an intense electric field which disfigures the linear properties of the chambers and is called Geiger Muller region IV. With the further increase there is a continuous discharge.

The first detectors of those properties were introduced by Geiger and Rutherford in 1908 [38]. Those detectors are cylindrical with a wire in their centre. In the Geiger mode it is counting α-particles while discharging. Their main operation is the base of the detector technologies followed. When a particle passes through anode wire gathers the charged carriers and then electrons due to their high velocity drain from the anode and UV photons are emitted.

Photons create further interactions while moving to the cathode(wall). In order to separate the pulses a resistor is fitted so as the anode voltage is smaller than the discharge minimum value. Geiger then replaced the anode with a fine needle. The electrical signal is a linear correlation to the energy lost and then β-particles can be measured independently.

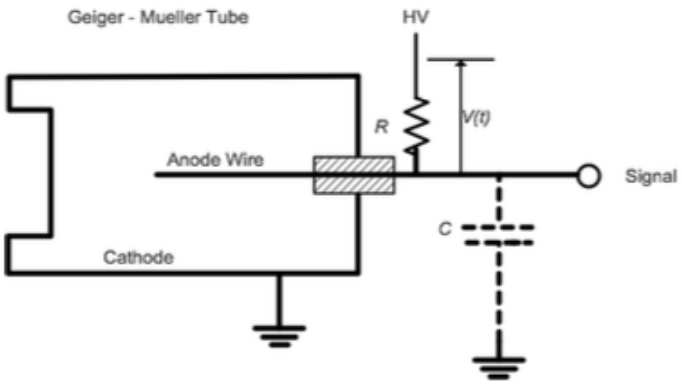

Figure 2.3: A representation of the circuit for the Geiger-Muller counter. In 1928 a thin layer of conducting material was added to the needle.

2.4.2 Micro-Pattern Gaseous Detectors

At first limited from their size but due to the modern photolithographic technology evolution, the Micro-pattern Gaseous Detectors(MPGD) are used widely for many years. They provide a spatial resolution better than 100μm, high rate capability larger than 10^6 Hz/mm^2 and single photon-electron timing resolution of the ns range. Micromegas detector specked for the New Small Wheel upgrade will be further analysed.

2.4.3 The Micro-Strip Gas Chamber

During the 1985 A. Oed was the first to use microelectronics and introduced the Micro-strip Gas Chamber(MSGC) [39]. He used small distance of anode-cathode ($\sim$ 100 μm) and by this way it could collect the ions fast and so by this way the field is not effected. Also metal strips, which are parallel one to another, 10 μm thickness are the anodes of the detector and continuous cathode strips which can be alternated with the anode strips by the voltage are induced to them. Also there is the back plane electrode which has equal potential with the anodes.

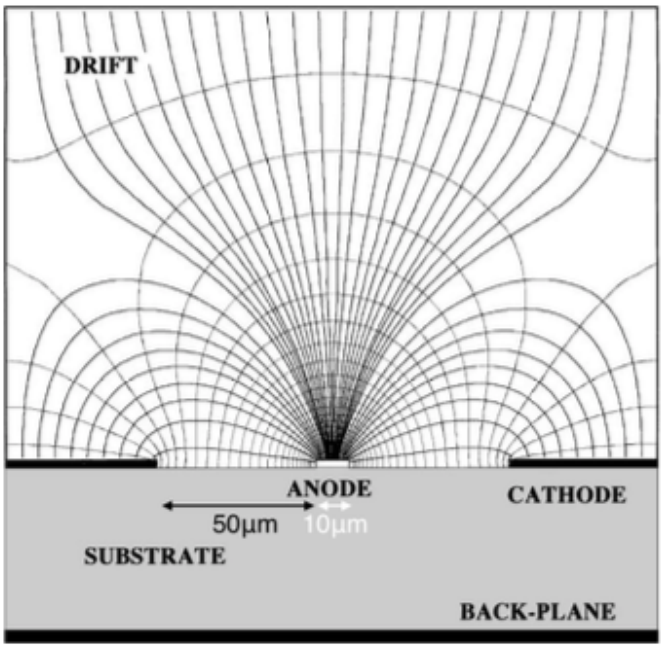

Figure 2.4: A representation of the MSGC electric field lines.

2.4.4 The Gas Electron Multiplier

The MSGC detector although performed with a high rate capability due to it's electrode fine construction could easily be destroyed from heavily ionising particles. For this reason Fabio Sauli invented the Gas Electron Multiplier in 1997 [40].

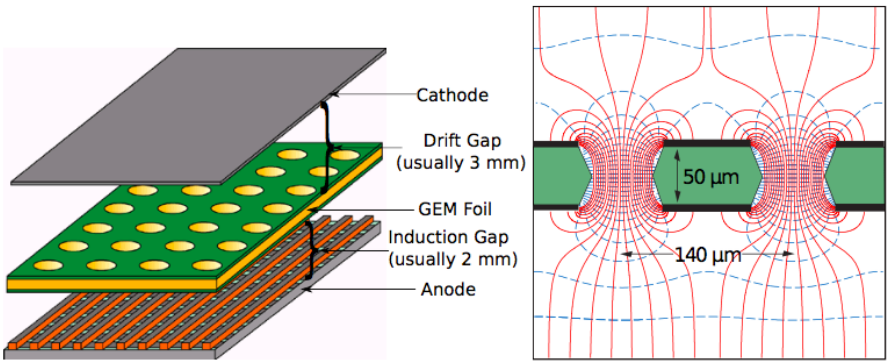

Figure 2.5: Schematic structure of GEM

As seen in figure 2.5 there is a matrix of holes($\sim 25 - 150$ μm diameter) with a pitch of 50-200 μm. GEM is made by an insulating foil ($\sim 50\mu$m) on both sides. All these construction different specks make a big difference in gain and detection. The potential difference applied to the two sides of GEM electrons drift to through the holes. Inside GEM the high electric field reforms the openings to amplification regions. GEM can also operate by using layers of GEM foils and by this way higher gain can be achieved.

2.4.5 The MicroMesh Gaseous Structure

Micromegas is and MPGD detector. The acronym Micromegas comes from MICRO MEsh GAseous Structure and was first introduced by I.Giomataris and G.Charpak [41] in 1996, after evolution stages and different configurations. Micromegas is a gaseous detector which is mostly characterised by it's inner gaps, the drift gap and the amplification gap.

Usually drift gap is 3-5 mm distance wide and amplification gap 100-150 μm. The drift region is induced with gas mixture and is also the conversion area. High voltage is applied in drift region by the drift electrode. Those areas are separated from the Mesh, a metallic grid which is also in high voltage region in this specification. Then at the amplification gap there are the cylindrical pillars made from insulating materials, in mm distance one to another. Pillars define the amplitude of the amplification gap.

When a charged particle is passing through the MM detector it is ionised by the HV applied. So electrons created from this process drift towards the Mesh in nanoseconds. Then at the amplification region, due to the different voltages applied

on the drift electrode and Mesh, there is a 50-100 times stronger field. Mesh is 95% transparent, depends though to different specifications and HV applied.

Electron avalanche is created in the amplification region. After the very small timing of one nanosecond the electrons induce a fast pulse to the readout strips also providing superb spatial resolution. The graphical representation is shown in figure 2.7.

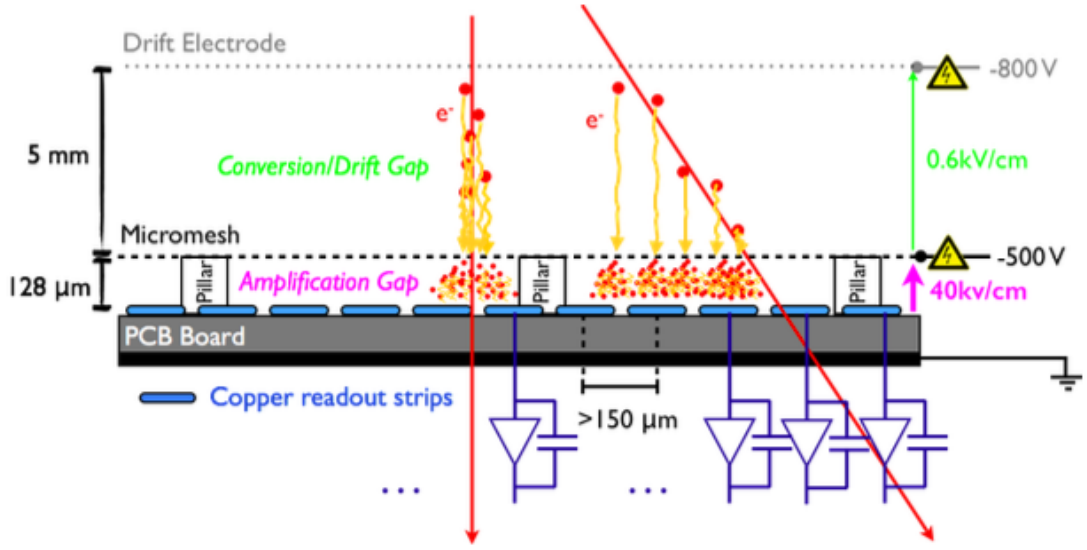

Figure 2.6: Schematic structure of Micromegas. The standard functions of the detector are represented.Ions are collected by the Mesh so space charge effects are not affecting the operation

The Bulk MicroMegas

Following an R&D process bulk MM were introduced in 2006 introducing a new manufacturing technique. Bulk MM structure is robust and low cost. Also this kind of manufacturing is very useful for large detectors. An FR4 anode plane with printed copper strips is laminated on a Printed Circuit Board (PCB) . The Mesh in this case is woven wire Stainless Steel with an extra photo-resistive layer not electroformed grid. The 300 μm diameter pillars are printed with a photolithographic method but pillar height and separation distance of the mesh are depended on the different needs of each experiment. Respectively with the bulk technique different distance specks can be used. The drift electrode is the same as the Mesh and is installed at the rest of the bulk structure. This is a lower cost fabrication method, it is more useful and resistant.

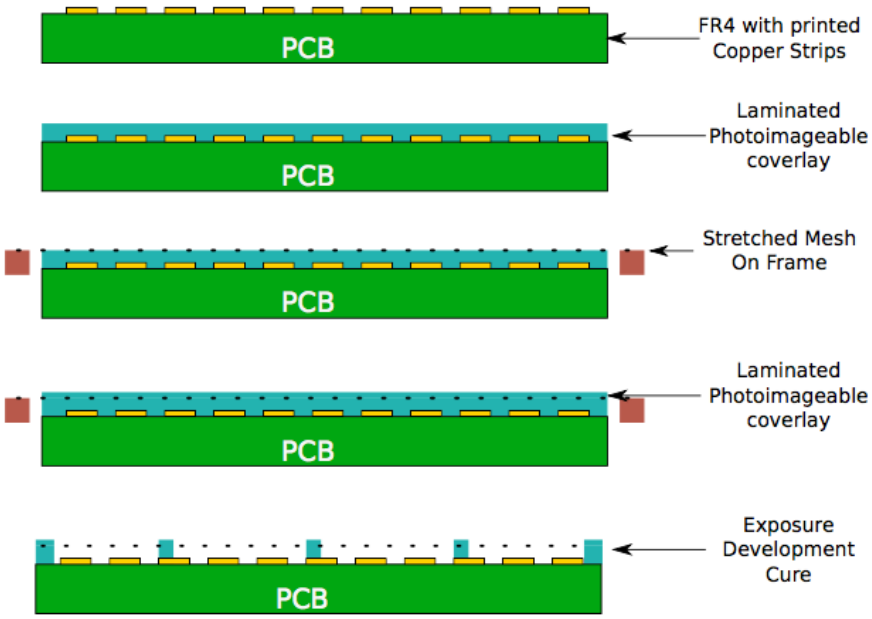

Figure 2.7: Manufacturing process of bulk MicroMegas

2.4.6 Micromegas detectors with resistive strips

Although the bulk Micormegas were a breakthrough they have an important limitation. Incoming particles can reach a gain of up to 10^7 range. In the bulk Micromegas case this leads to discharges and sparks.

To solve this problem the Muon ATLAS MicroMegas Activity (MAMMA) [42] through an R&D process, especially for the MM detectors for the NSW upgrade, was initiated. They reached to the decision of using the Resistive Micromegas which have the same fabrication as bulk ones but added a resistive layer above the copper readout strips. Resistive strips are the same dimensions as the readouts but they are grounded. Using consecutive resistive strips decreases the discharge rate due to sparks while detector is still efficient and can operate in a high rate.

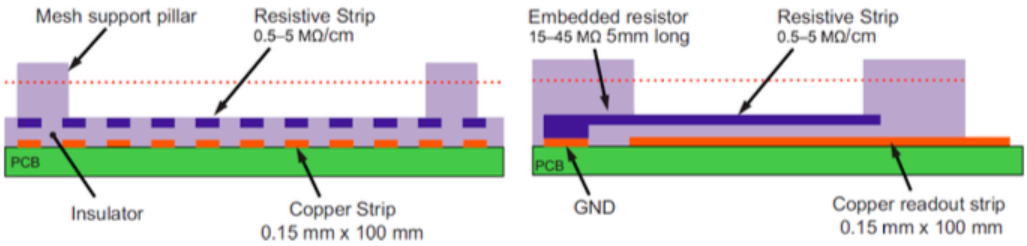

Figure 2.8: Graphical representation of the resistive MM

Micromegas output has been extremely studied using different conditions. The figure 2.9 shows the monitored HV and currents left for non-resistive MM chamber while the right is for the resistive one [43]. Chambers were exposed to a neutron beam of 5.5 MeV energy with a 10^6 Hz/cm^2 flux.

The two chambers were applied to the same voltages, same gas mixture and operated with the same electronics. Typical spark signals, directly measured through on the readout strips, are shown for a non-resistive chamber on the left and a resistive MM on the right:

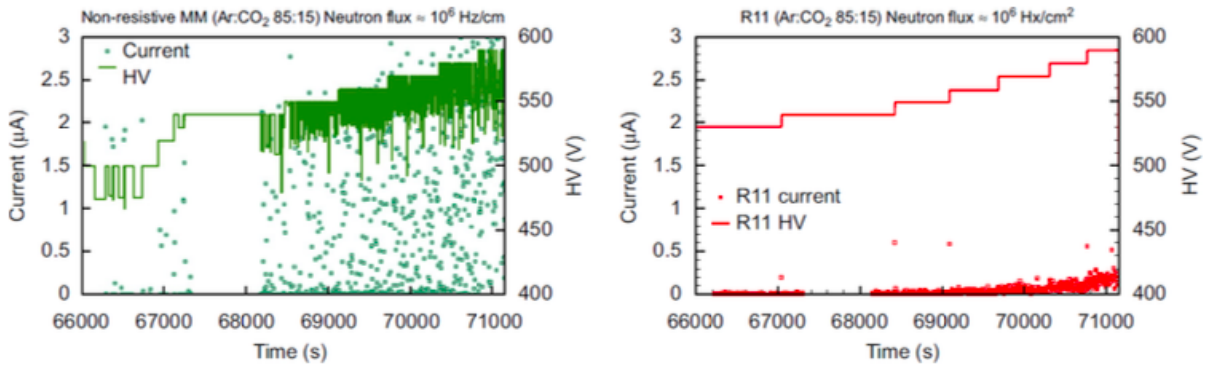

Figure 2.9: Studies for non-resistive and resistive MM chambers with a Neutron flux as a function of current, supplied voltage

The steps of HV applied (simultaneously on both chambers) are illustrated from the continuous line while the points are for the current. Resistive MM can operate in high rate neutron flux even for a high gas gain while non-resistive can create sparks even for low gain values while for the highest Voltage values the discharges make it very hard to operate. In the event of a spark the resistive strip charges up and the discharge current flows through the resistive strip to ground.

The spark amplitudes in the resistive MM are reduced by an order of magnitude compared to the MM without resistive-strip protection. Moreover, the discharge is recovered much faster in the resistive MM and the dead time caused by the spark is greatly reduced by the resistive-strip protection scheme. The area of discharge is kept small by this way.

The resistive strips technology is very useful for chambers with multiple readout layers.In figure 2.10 we can see a two-dimensional MM chamber.The second layer (Y strips layer) is on top of the X layer while the two layers are separated from FR4 material.So the X-Y strips are perpendicular to each other giving a two dimensional hit position.

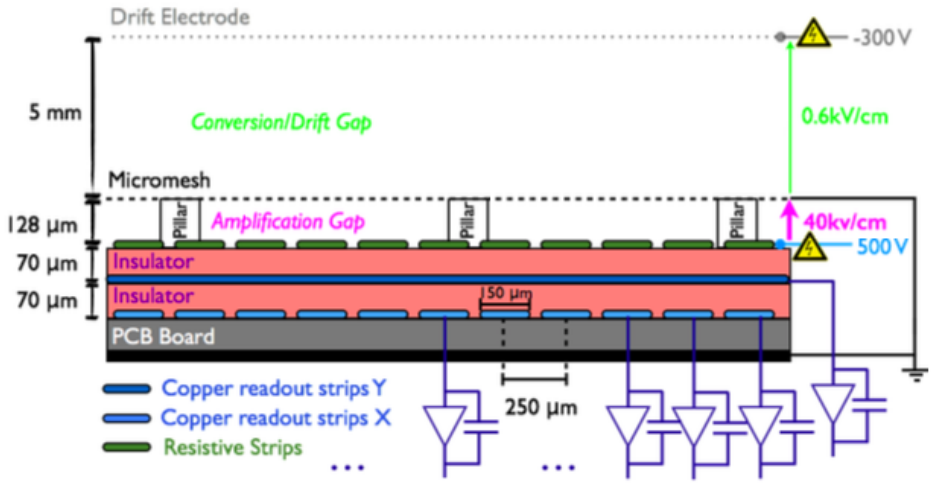

Figure 2.10: Resistive MM chamber with a 2D readout.

2.4.7 Micromegas gas mixture

As discussed in 2.3.1 the gas in the detector is a mixture of a high proportion of noble gas and a polyatomic quenching gas. The mixture in Micromegas case is based in Argon and the quench gas is the CO_2. After simulation studies using Garfield and Magboltz in drift velocity and Lorentz angle but also in transverse diffusion, it was determined that for the NSW upgrade requirements the best mixture was Ar + 7%CO_2.

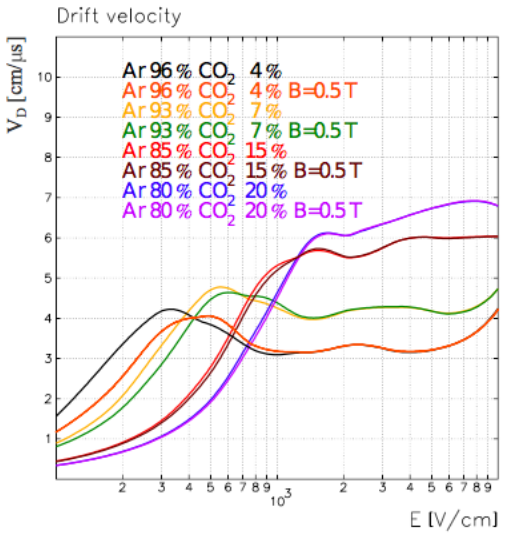

Figure 2.11: Drift velocity for different mixtures.

This was due to the plateau region achieved by this mixture to the electric filed of 600V/cm operating voltage. Mesh transparency close to 100% is achieved in electric field of less than 1 kV/cm for drift region in this case it is 0.6 kV/cm.

In figure 2.12 we see the plateau of drift velocity at this electric field value range. For less than 0.5 T magnet field it has a 4.7 cm/μs of average velocity. Then at the amplification region the electric field is much higher in the 40 kV/cm area while drift velocity is approximately 12 cm/μs.

The Lorentz angle due this strong electric field is less than 5^o in amplification region while in the drift region the electrons are much affected with over 25^o deviation in 0.5 T region.

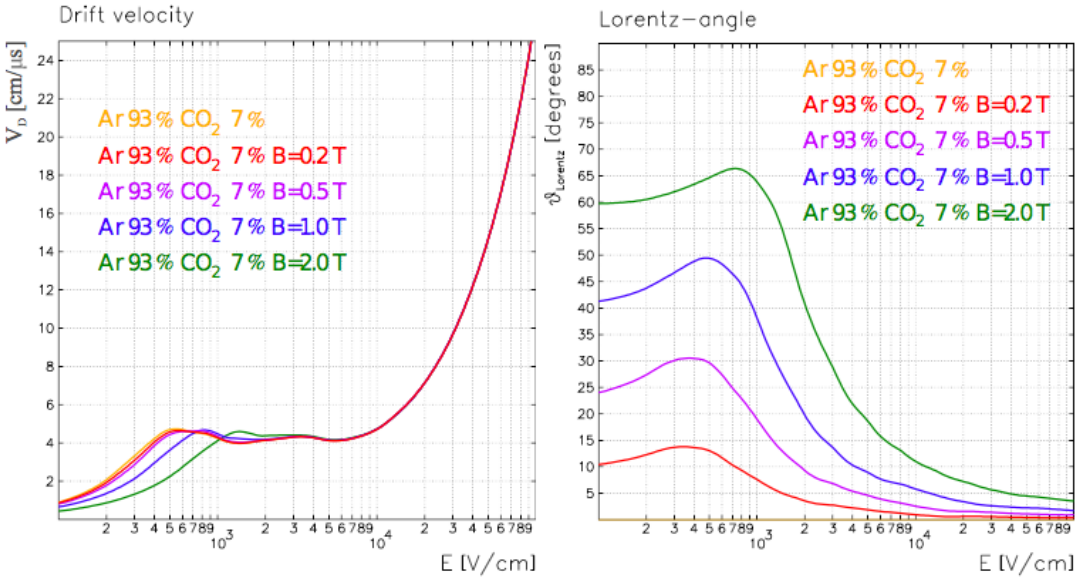

Figure 2.12: Drift velocity and Lorentz-angle as a function of Electric field. **Left:** Drift velocity for different magnetic fields. **Right:** The Lorentz angle for low electric fields like in amplification region is affected in the presence of an intense magnetic field

2.5 NSW upgrade MicroMegas Parameters

As discussed in 1.3 the New Small Wheel upgrade is taking place in the inner-end cap region of the muon spectrometer. Current set up is going to be replaced with Micromegas and sTGC detectors(multi wire proportional chambers). The prototypes of the modules were the detectors for the data analysis of this thesis.

2.5.1 MM module design and concept

NSW consists of 16 sectors, 8 big and 8 small. Each sector will include eight layers of MM detectors making it 128 in total. Those sectors are segmented in lower or larger radius and large or small sectors which makes four different configurations(LM1, LM2, SM1, SM2) [44]. Each configuration is segmented in eight PCB boards of 0.5 $\pm 0.05 \mu$m thickness. The PCBs will be four different types. Two will have strips perpendicular to the redial direction while two will have strips of the reconstruction of second coordinate [45]. Each PCB comprises of 1024 readout strips covered by a 50 μm thick Kapton foil.

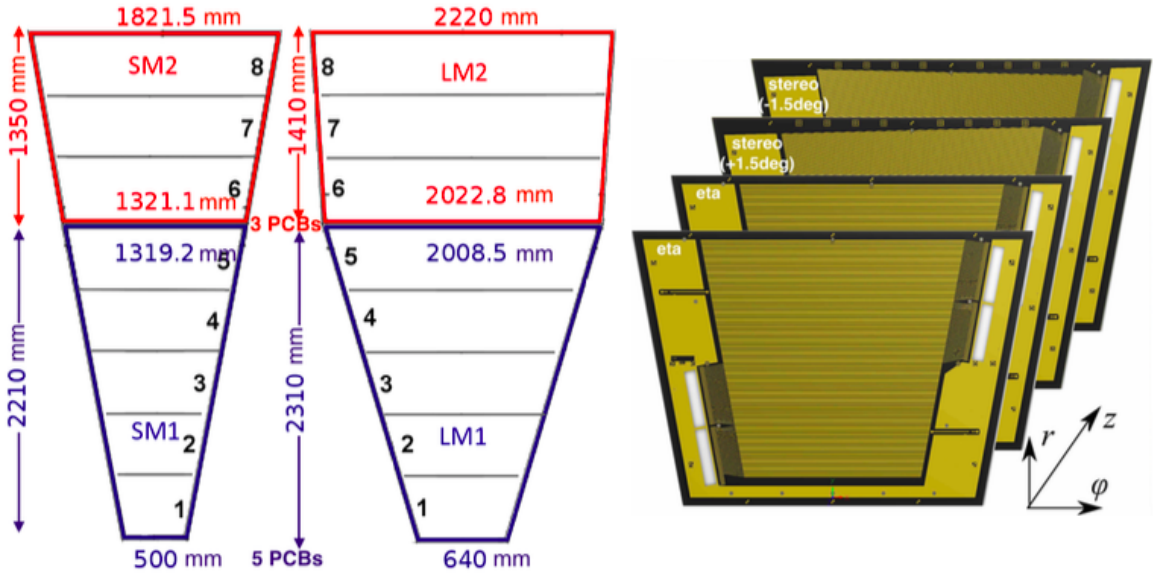

Figure 2.13: Graphical representation of MM modules with exact dimensions.Large sectors of the wedge consist of 5 PCBs while small sectors consist of 3 PCBs.Also four different PCB types are represented.

The detectors are designed to allow a spatial resolution of 100 μm in the precision radial (η) and 2-3 mm in the non precision ϕ direction. To reach such a resolution good planarity of readout and drift panels is required. This is achieved by two vacuum tables.

The large size of the wedges led to a new construction method called the mechanically floating mesh. Stainless steel mesh is pre-stretched and glued on an aluminium frame which is attached to the drift panel. Then it is pressed on the pillars making it accessible. By this method the amplification gap is slightly higher so higher amplification voltage is required.

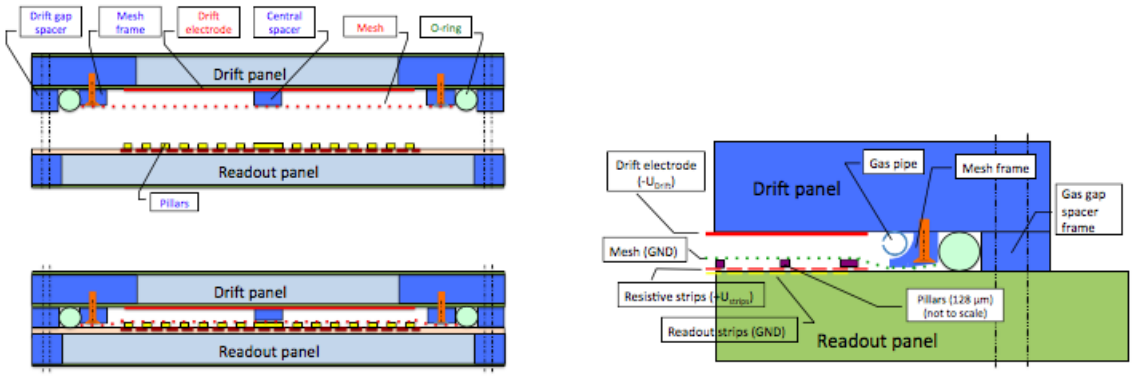

Figure 2.14: **Right:**The mechanically floating mesh teqnique. In closed position the mesh touches the pillars on the readout panel. **Left:**Electrical potentials of readouts strips, resistive strips, mesh and drift electrode are indicated.

2.5.2 Quadruplet Design Parameters

The Micromegas detectors inside the NSW are segmented in quadruplets. They consist of three drift panels and the readout structure consists of two double sided readout panels. The outer drift panels are identical and only on the inner side there is the cathode and micro-mesh while the inner drift panel is double sided. The readouts consist of strips with 0.43 mm pitch and up to 2 mm length and they are double sided one carrying the parallel eta strips while the other the stereo strips.

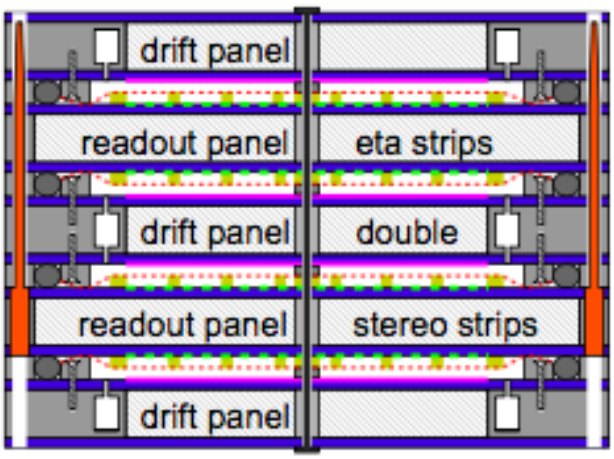

Figure 2.15: Graphical representation of the quadruplet structure with the inner double sided readout panels and the three drift panels.

On the figure 2.15 we can also see the mesh (red colour) supported by the drift panels, while the pillars (yellow) in this case are 128 μm high. The structure of the quadruplet is sealed and tightened with O-rings and if needed it can be opened for operations needed such as maintenance. Modules are assembled vertically in a clean room to avoid dust contamination [44]. Before sealing one with the other gas tightness of all panels is tested with the measurement of pressure drop as a function of time. For such a large surface there are also needed some alignment methods. The readout panels are aligned by two precision pins and bushings while the the drift panels the mounting hole accuracy is sufficient. After closing a high voltage test is performed.

The connection between the MM detectors of the NSW and the trigger(ADDC) and TDAQ(L1DDC) systems is performed by the MMFE-8(MicroMegas Front End) board [46]. Number eight refers to the 8 VMM Asics on the front-end board.VMM ASIC will be further analysed in the next chapter.

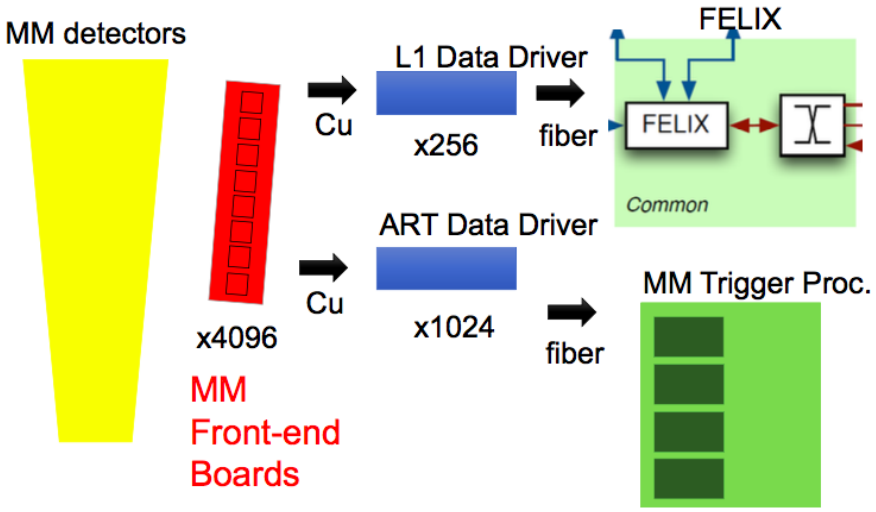

Figure 2.16: MMFE-8 simple Overview

CHAPTER 3

THE VMM ASIC FOR THE NEW SMALL WHEEL UPGRADE

The VMM is a Application Specific Integrated Circuit (ASIC). It is the front end ASIC for the electronics readout in MicroMegas and sTGC detectors of the NSW upgrade. VMM is developed at the Brookhaven National Laboratory by Gianluigi de Geronimo and his microelectronics group. It is fabricated in the 130 nm Global Foundries 8RF-DM process(former IBM 8RF-DM).

3.1 NSW electronics complexity

3.1.1 The MMFE-8 board

MMFE-8 board is the front-end electronics for the ATLAS MM detectors [47]. It interacts directly with the trigger(ADDC) and DAQ (L1DDC) electronics [1]. In addition a communication is established between L1DDC and ADDC cards.

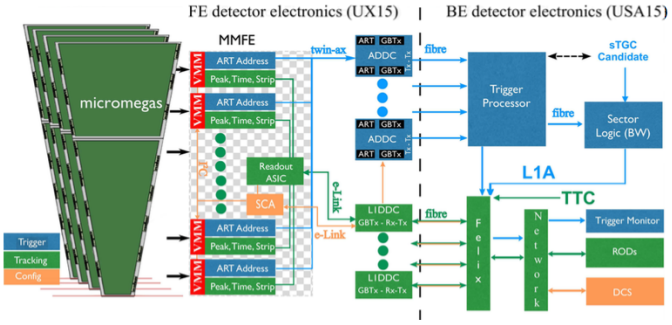

Figure 3.1: Overview of the NSW MM electronics. The MMFE-8 board is connected with the ADDC and L1DDC cards via e-links.Picture is taken from [1]

The 8 in MMFE-8(MicroMegas Front-End) board, refers to the 8 VMM ASICs. The Demonstrator board uses an FPGA (Artix-7), Ethernet PHY and COTS for DCDC/LDO while the Production board uses an SCA (Slow Control ASIC), ROC (Readout Out Controller ASIC), FEAST (DCDC), and has no PHY.

Figure 3.2: The MMFE-8 Board

Two Zebra connectors and holders are located on the top of board. The Zebra connectors themselves are 110 mm x 6.30 mm x 2.50 mm. The wire pitch is 100 mm and the wire width is 50 mm, which can be compared to the MM pad pitch of 400 mm and pad width of 200 mm. Each Zebra connector mates to 256 MM channels. There are four additional channels on each Zebra connector that are used for MM ID. The MM ID is determined by shorting the ID lines to ground on the detector side. There is an internal pull-up on the FPGA side. Significant R&D work remains to be carried out investigating the robustness of these connectors.

Front-end electronics will be installed on the MM wedges radially along both sides. This is a way to equalise the load on both sides of the detectors and cable routing [2].

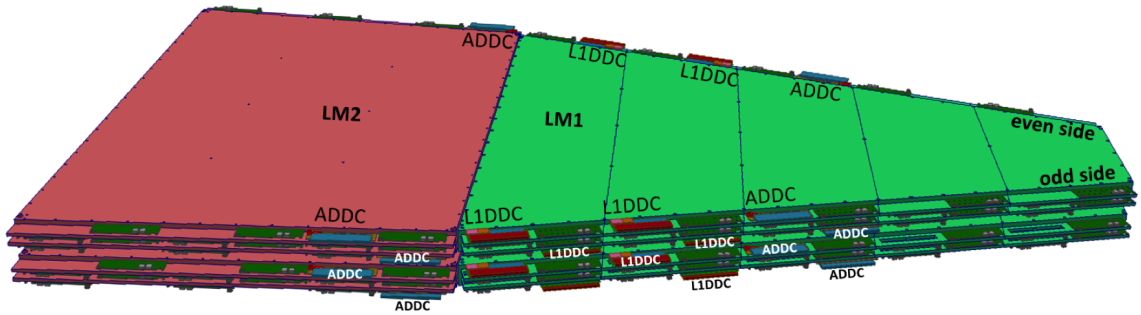

Figure 3.3: A MM sector with the electronic placement

L1DDC and ADDC will be placed only on the 1^{st} and 4^{th} plane of each wedge. One L1DDC and ADDC serve 8 front end boards to minimise cable length making

the total numbers of 512 L1DDC, 512 ADDCs and 4096 MMFE8 boards. Also the front end ASIC for the MM chambers the VMM has 64 channels per chip and every one channel is the direct read out for one MM strip. So eight chips per board make it a total of 512 readout strips .

The micromegas system of the NSW needs to provide muon segment candidates to the Sector Logic (SL) within the Level-1 latency of 41 clock ticks of 40 MHz. This corresponds to a latency of 1025 ns. Once the segment is confirmed by the SL the tracking primitives have to be readout and processed. The micromegas system consists of ∼2.1 M channels. The front-end ASIC providing the trigger and tracking primitives is the VMM. The MMFE, apart of the VMM ASIC, will feature a GBT-SCA8 for the configuration, calibration and monitoring of the MMFE8. Moreover a custom readout ASIC will be integrated in the MMFE8 capable to gather, format and serially transmit the information of the eight VMM into a single e-link output. A separate e-link will be used for the configuration path.

The MMFE8 is also capable of driving the ART signals to a separate transmission line for every LHC bunch crossing of 25 ns. All the components of the MMFE are installed in a PCB of 215×60 mm^2[1].

3.1.2 The L1DDC card

The Level-1 Data Driver Card (L1DDC) card will serve as an intermediate stage between the Front End boards and the Felix interface system and is designed for the NSW upgrade needs by the NTUA HEP team. The two technologies of NSW sTGC and Micromegas (MM) use the same building blocks for the readout L1DDC cards. It is also capable to configure the ADDC and the MMFE through dedicated to configuration E-links.

The L1DDC is built in a PCB of the same dimensions like the ADDC readout data of eight MMFE. ADDC and L1DDC are multiplexed through e-links.

The L1DDC features a GBTx ASIC. GBTx is capable of driving the Level-1 data through the GBTx into a fiber to a network interface called FELIX .

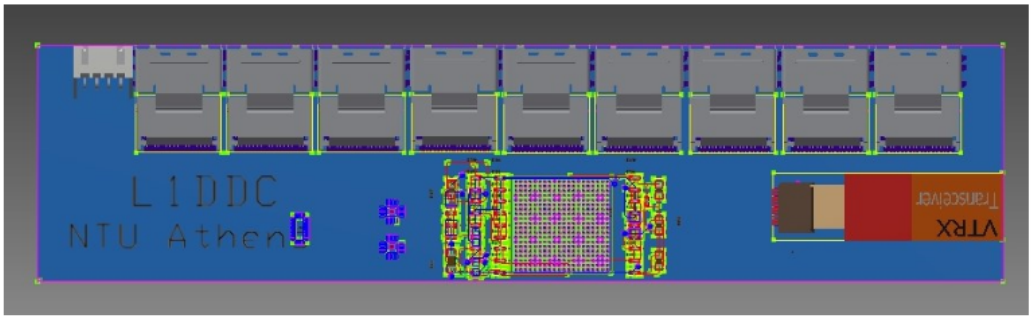

Figure 3.4: 3D Model of the L1DDC

L1DDC implements the configuration e-links uniform along the radial direction with a bit-rate of 80 Mbps e-links while the readout e-links, with a bitrate of 160 Mbps for the four outer MMFE and 320 Mbps for the inner four. This is due to the higher particle rate which requires a higher bandwidth in the inner radius of the detector[1].

3.1.3 The ADDC card

The Address in Real Time Data Driver Card (ADDC) for the MM Detector will be used in the ATLAS NSW upgrade [48]. It addresses the first-above threshold events. The design and fabrication of ADDC prototypes and final boards will be in Brookhaven NL and Dr.Lin Yao is the main engineer working on the ADDC. The production of ADDC will be together with the VMM chip [49].

A custom ASIC (ART ASIC) will receive ART signals and do the hit selection processing. The primary function of the card is to transmit the trigger data from the front end ASICs to the trigger processor in the USA15.

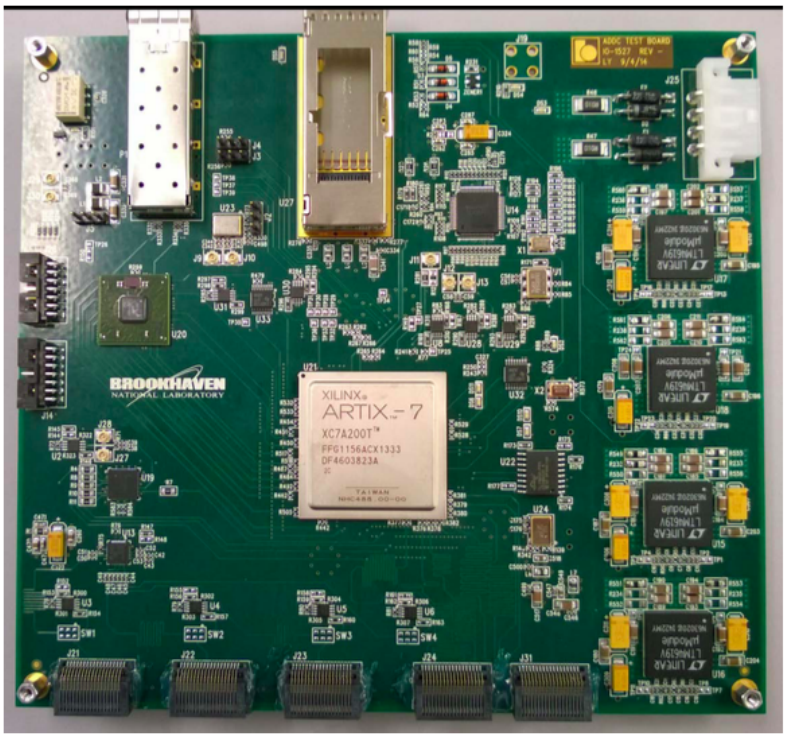

Figure 3.5: ADDC version 1 Photo

For the Micromegas detector, the trigger primitive is the Address in Real Time (ART). The ART is generated by each of the 64-channel front end ASIC (the VMM) at every bunch crossing and it is the 6-bit address of the strip with the earliest hit above a given threshold. The ADDC receives the ART signals from the front-end

board, does a priority-based hit selection, and then sends the selected data to the back end trigger processor.

The hit selection will be processed by a custom ASIC, the ART ASIC. Finally the GBTx ASIC and VTTx transmitter module collect data from up to 32 front end ASICs and transmit them to the trigger processors through an optical fiber link.

To take advantage of the dual optical transmitter links on one VTTx module, the ADDC board is designed to handle 64 front end ASICs with 2 GBTx chips. Another ASIC of the GBT chipset, the GBT-SCA, will be used on the ADDC for configuration and control of the ART ASIC and the second GBTx.

3.2 The Specifications of the VMM2 ASIC

VMM is the front end ASIC for the NSW upgrade. The results that will be presented in the next chapter of this thesis, are all retrieved from MM detectors,the LM2,SM1 prototypes and a T-chamber which are readout from VMM2 and VMM3 chips. VMM is highly configurable and will be used on both sTGC and MM detectors.

Specifically it will readout negative anode strip signals from the Micromegas detectors and negative wire-group signals from the sTGC detectors, positive cathode strip signals from the sTGC for precision spatial reconstruction and positive cathode pad signals used in the sTGC trigger.

3.2.1 Description of the VMM

VMM is composed of 64 linear identical front-end channels.In figure 3.6 we can see the channel architecture.

A low-noise charge amplifier (CA) with adaptive feedback, test capacitor and adjustable polarity optimised for a capacitance of 200 pF and a peaking time of 25 ns. The shaper is a third-order designed in delayed dissipative feedback and has adjustable peaking time in four values (25,50,100 and 200 ns) and band-gap referenced baseline.

The DDF architecture offers higher analog dynamic range, making possible a relatively high resolution at input capacitance much smaller than 200 pF. The gain is adjustable in eight values (0.5, 1, 3, 4.5, 6, 9, 12, 16 mV/fC).

Next to the shapers are the sub-hysteresis discriminators [50] with neighbour enabling logic and individual threshold trimming, the peak detector, and the time detector. The sub-hysteresis function allows discrimination of pulses smaller than the hysteresis of the comparator circuit.

The threshold is adjusted by a global 10-bit DAC and an individual channel 5-bit trimming 150 DAC. The neighbour channel logic forces the measurements of channels neighbouring a triggered one, even if the channel does not have a signal over the set threshold. The neighbour logic extends also to the two neighbouring chips through bidirectional IO.

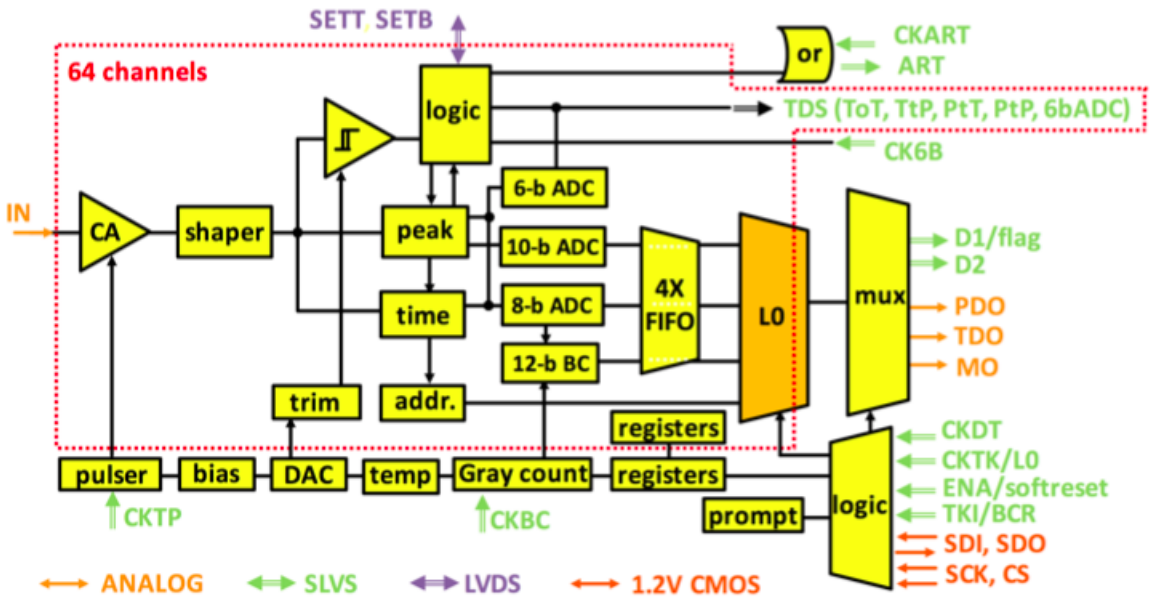

Figure 3.6: Channel architecture of the VMM2

The peak detector measures the peak amplitude and stores it in an analog memory. The time detector measures the peak timing using a time-to-amplitude converter (TAC), a voltage ramp that starts at the time of the peak and stops at a clock cycle of the BC clock. The TAC value is stored in an analog memory and the ramp duration is adjustable in four values (60 ns, 100 ns, 200 ns, 400 ns). The peak and time detectors are followed by a set of three low- power ADCs (a 6-bit, a 10-bit, and a 8-bit), characterised by a domino architecture [51] but of a new concept. These ADC are enabled depending on the selected mode of operation.

The most common problem of the VMM chip is usually a non operative channel. In this case there is a small spatial resolution local inefficiency which can be corrected with software. For more than two adjacent channels there will be a bigger effect in the spatial resolution efficiency. In the case of a chip failure there will be a non operative segment of 3.5 cm in the given sector of a MM chamber. In the case of sTGC chambers the dead pitch will be bigger .

3.2.2 Signal Processing

In this section the analog requirements for both detector technologies are analysed. The MM readouts are the anode strips which input negative polarity signals to the VMM. Signal is induced from electrons and positive ions after the avalanche is formed within the 128 μm amplification gap. Due to the small gap the signal has a $\sim$ 200 ns duration.

Since the ions are moving in a constant electric field the current is uniform and the anode strip capacitance varies from 50-300 pF depending on the length of the strips. The noise is determined by the requirement of a single primary electron detection with a threshold 5 times the rms noise, a gas gain of 30.000 collecting half of the charge and the maximum posiible electrode capacitance of 200 pF.From those conditions the noise level must be 0.5 fC or 3000 electrons rms.

3.2.3 Physical Description of the VMM

As referred above VMM is a fully custom ASIC. VMM2 and VMM3 most specs are the same in the case of layout and pin assignment. It will be packaged in a 400 ball, 1 mm pitch BGA.

The VMM2 layout size is 13.518×8.384 mm^2 and the die size 13.599×8.464 mm^2. With the addition of the Latency and Level-0 buffers the die size is expected to increase by about 1mm in its long side. The ball assignment is shown in Fig.3.7, and the detailed pin list and their functions in Table 1.

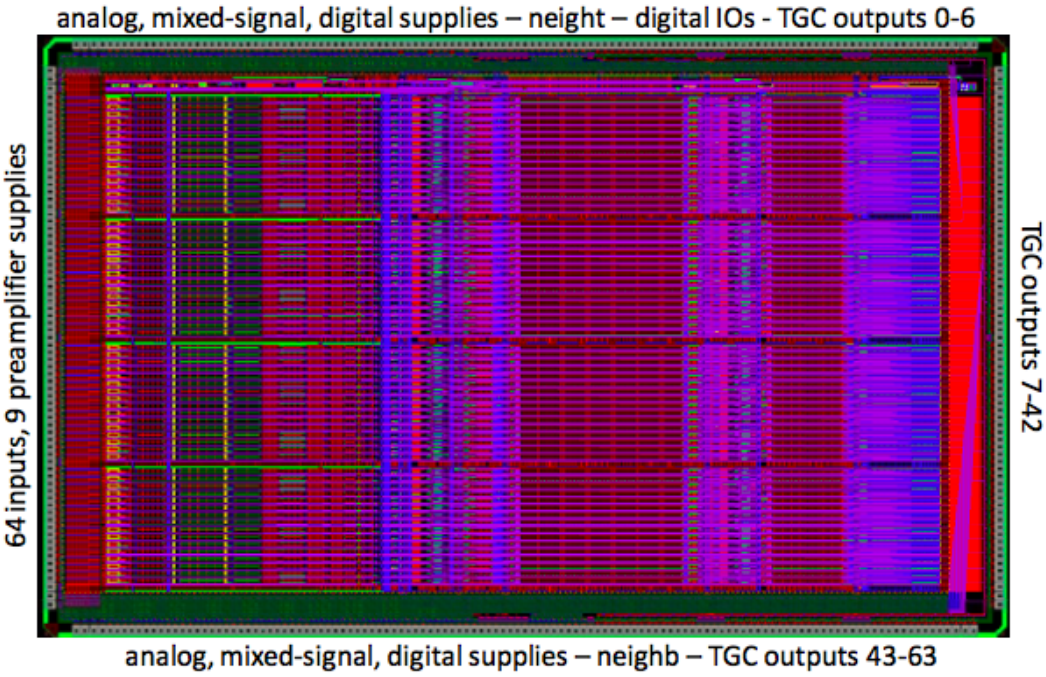

Figure 3.7: VMM die layout

BGA Ball Function	
Ball/Pin name	**Description-Comments**
Vdd,Vss	Analog supplies 1.2 V and grounds 0 V – 123 pins total, max current 400 mA
Vddad, Vssad	Mixed-signal (ADC) supplies 1.2 V and grounds 0 V – 16pins, max current ∼200 mA
Vddd, Vssd	Digital supplies 1.2 V and grounds 0 V 22 pins
Vddp	Charge amplifier supplies 1.2 V 12 pins, max current ∼150 mA
i0-i63	Analog inputs ESD protected
mo	monitor multiplexed analog output
pdo	Peak Detector multiplexed output. Not used by NSW
tdo	Time detector multiplexed analog output . Not used by NSW
SETT	Ch 0 neighbor trigger, SLVS
CKBC	Bunch Crossing clock, SLVS, Advances 12-bit Gray-code BC counter
CKTP	Test Pulse Clock, SLVS
SDI	Configuration SPI data input, CMOS
SDO	Configuration SPI data output, Tristated if chip is not selected , CMOS
CS	Configuration SPI chip select, CMOS
SCK	Configuration SPI clock, CMOS
TKI	BCR/OCR. Token input in analog mode
TKO	Token output Used in analog mode only

ENA	Acquisition start/stop and provides acquisition reset at falling edge:
	• ena high: acquisition is enabled
	  • internally enabled after 40 ns from ena high
	  • in two-phase (analog) mode is acquisition
	  • in continuous (digital) mode is acquisition and readout

CK6B	6-bit direct output clock, SLVS
CKTK	Level-0 accept (L0). Token clock (non-NSW use), SLVS
DT0	Flag and first data line in digital DDR mode (flag and address in analog mode), SLVS
DT1	Second data line in digital DDR mode, SLVS
CKART	Address in Real Time (ART) clock, SLVS
ART	ART output, SLVS
CKDT	Data clock SLVS
ttp0–ttp63	Direct digital outputs, SLVS
SETB	ch63 neighbor trigger, SLVS

Figure 3.8: Table 1: Pad/Pin Assignment/ Function

3.2.4 Cooling of the VMM

In the detector area with high radiation and density VMM ASIC must be cooled. For this reason there is a water cooler region.

The IBM Design Manual specifies the operating temperature range to be from -55^oC to 125 ^oC. However device life time degrades rapidly at high temperatures. So temperature should be kept less than 50 ^oC ideally in 30-40 ^oC range. VMM includes a temperature sensor which can readout in configuration mode. The die temperature is approximately given by:

$$^oC = 725 - \frac{V_{sensor}}{1.85}$$

where V_{sensor} is the temperature sensor reading in mV.

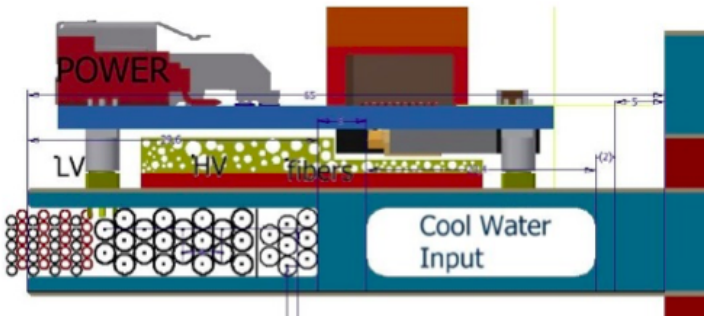

Figure 3.9: The cool water input under the detector area

3.2.5 Functional Description of the VMM

The VMM ASIC can operate in independent data paths the configuration mode, two-phase analog mode and continuous digital mode.

Configuration mode

In configuration mode the VMM is having the data acquisition (ena) signal at low and Serial Peripheral Interface(SPI) configuration (cs) at low. Then the chip registers are accessible through the configuration SPI clock (sck) the configuration SPI data input (sdi). The data transmitted are shifted at the falling edge of sck in 96-bits groups and latched when cs is high. What is registered in the configuration mode is available through the configuration SPI data output (sdo). The front end board for the MM detectors will contain 8 VMM chips and when one is not selected its sdo is tri-stated or high impedance so it doesn't interfere with the data.

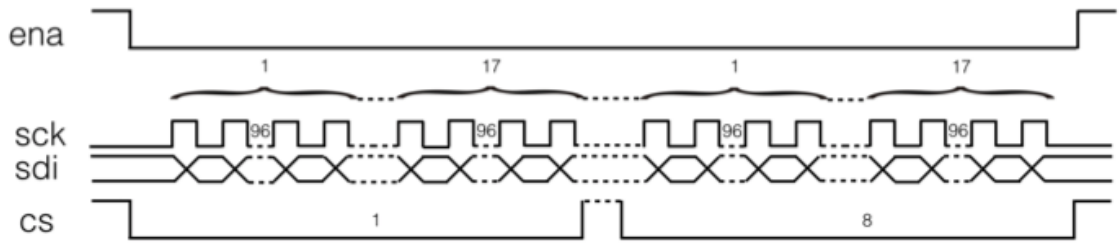

Figure 3.10: Timing in configuration mode

Two - Phase Analog Mode

In this mode, available from VMM1 implementation, the ASIC operates in two phase, performing acquisition when ena high and readout when ena low. The events are processed and stored in the analog memories of the peak and time detectors. As soon as a first event is processed, a flag is raised at the digital output of first data line the data0. Once the acquisition is complete the ASIC can be switched to the readout phase and the readout proceeds injecting a token at the token input tki. The first set of amplitude and time voltages is made available at the analog outputs peak detector output (pdo) and time detector output (tdo).

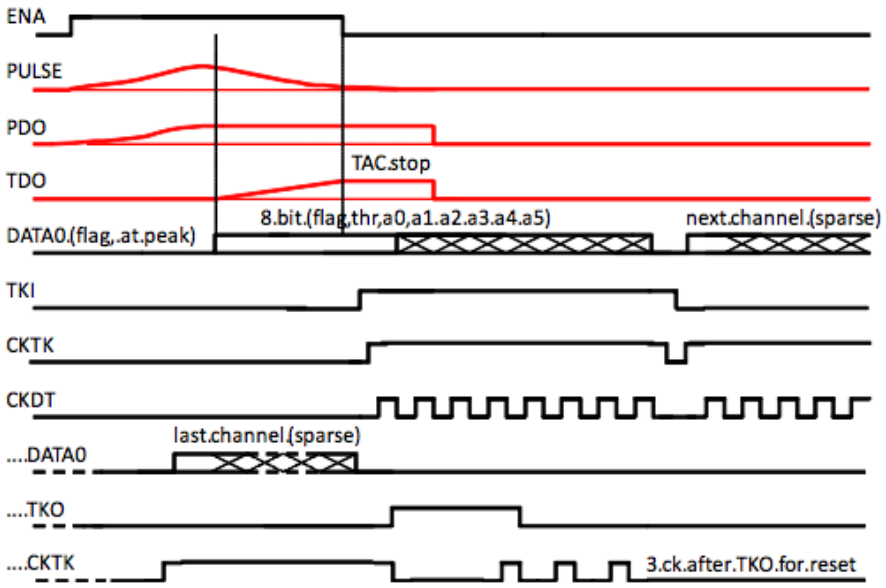

Figure 3.11: Timing in analog mode

Analog buffers can be enabled using the global register bits sbfp and sbft. The address of the channel is serialized and made available at the output data0 using six data clocks. The next channel is read out by advancing the token with the token clock. The token is sparse, passed only among those channels with valid events. If, after the token clock occurs, the data0 goes low, the readout is complete and the token is routed to the output tko for the readout of the next chip. This allows a daisy-chained readout with a single token input.

This mode will not be used in the NSW, but is being left in subsequent versions as an option. It should be noted that the two trigger paths, the 64-channel parallel outputs as well as the ART stream are active in this mode as well. The flag of the ART can be used, for example, as a fast all 64-channels whereas the prompt parallel outputs can be used to implement more sophisticated trigger algorithms. If not needed the

parallel SLVS outputs can be disabled with significant savings in power consumption and increased noise immunity from digital activity.

Continuous Mode

In the continuous mode the 64 channel direct digital outputs ttp0-ttp63 and each channel resets at the end of every pulse providing a continuous function. Each channel operates individually. The pulses are separated in four categories: time-over-threshold (ToT), threshold -to- peak (TtP), peak-to-threshold (PtT), or a 10 ns pulse occurring at peak (PtP), and can be set using the global bits stot and stpp. Alternatively, if the bits spdc and s6b are both set high, the peak detector converts the voltage into a current that is routed to the 6-bit ADC. The 6-bit ADC provides a low-resolution A/D conversion of the peak amplitude in a conversion time of about 25 ns from the peak time after an event flag which occurs at the peak time. Using another global bit called sc6b and the channel bit sz6b conversion time and zeroing can be set respectively. The flag is lowered at the next clock cycle of the data clock, and the 6-bit ADC data is shifted out after that, either at each clock cycle or at each clock edge of the data clock depending on another global bit the sdck6b. The channel reset occurs after the last bit has been shifted out.

In this mode the peak and time detectors convert the voltages into currents that are routed to the 10-bit ADC and 8-bit ADC respectively. The 10-bit ADC provides a high resolution A/D conversion of the peak amplitude in a conversion time of about 200 ns from the occurrence of the peak. The conversion time and baseline (zeroing) are adjustable using the global bit set sc10b (the conversion time is a 200 ns base plus a 60 ns increment for the MSB and LSB phases, set by the sc10b bits) and the channel bit set sz10b respectively. The 8-bit ADC provides the A/D conversion of the peak timing (measured using the TAC) from the time of the peak to a stop signal.

The TAC stop signal occurs at a next clock cycle of a shared 12-bit Gray-code counter which is incremented using the external clock signal BC. The counter value at the TAC stop time is latched into a local 12-bit memory, thus providing a total of 20-bit deep timestamp with a nanosecond resolution. The conversion time and baseline (zeroing) are adjustable using the global bit set sc8b (the conversion time is a 100 ns base plus a 60 ns increment for the MSB and LSB phases, set by the sc8b bits) and the channel bit set sz8b respectively.

The channel is reset once both the 8-bit and 10-bit conversions are complete and the digital values are latched in digital memories. Thus, in continuous (digital) mode a total of 38-bits are generated for each event. The first bit is used as a readout flag, the second is the threshold crossing indicator (allows discrimination between above-threshold and neighbour events). Next is a 6-bits word for the channel address, followed by 10-bits associated with the peak amplitude, and 20-bits associated with the timing. The digital output bit assignment is summarised also on the table of 3.6.

3.3 MicroMegas Triggering scheme

The VMM, in addition to the information recorded at Level-1 (or Level-0), provides trigger primitives for both Micromegas and sTGC detectors. In each case an independent trigger data path provides information to the trigger processor at the bunch crossing frequency.

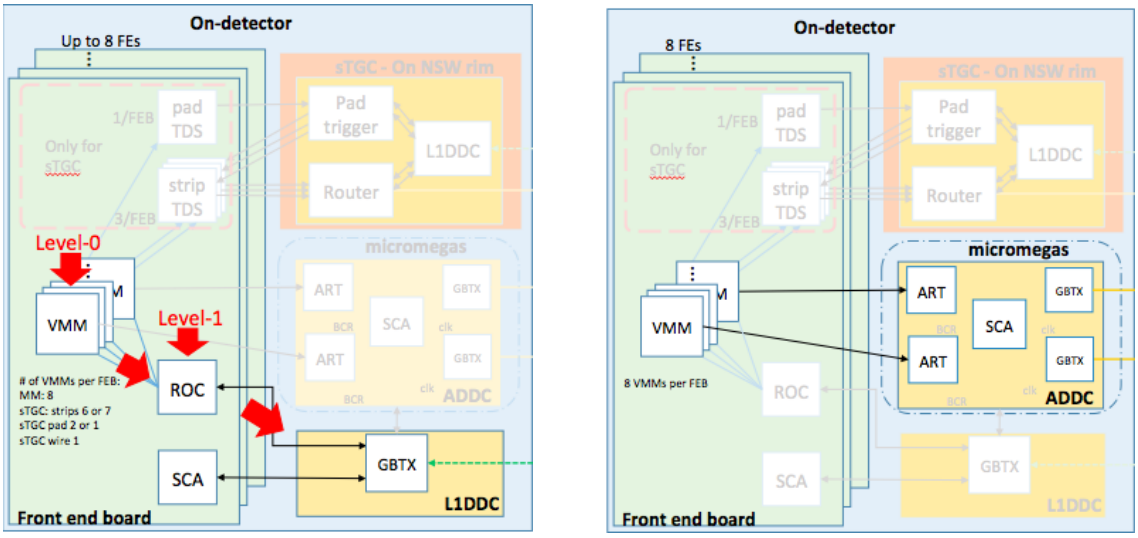

(a) (b)

Figure 3.12: (a) Level-0 and Level-1 readout scheme (b) MicroMegas readout scheme. Pictures are taken from [2]

The MM detector in the NSW will have over 2 million channels. This is making really hard the measurements for the trigger to be done parallel and in real time. Each VMM provides the function of address in real time (ART) of the first chip above threshold. The system, thus, is equivalent to a trigger system with segmentation of 3.2 cm(64 x 0.5 mm) with spatial resolution of order of 300 μm sufficient for the angular resolution required in order to reject candidates that are not consistent with those originating at the interaction point. This way the trigger channel count is reduced to 32,000 channels(4096 total mmfe8 boards x 8 vmm each).

The ART mode is enabled with the bit sfa. Either at the pulse threshold crossing (bit sfam low) or at the pulse peak (bit sfam high) a flag is released at the art output. The flag is followed by the serialised address of the event. Also in this case the address is released either at each clock cycle or at each clock edge of the external ART clock, depending on the global bit sdcka. Arbitration logic blocks subsequent to the first hit those occurring 2 or more ns later.

The ART must be aligned to the ART clock. It can optionally be provided at threshold crossing or at peak found. In the NSW implementation we choose the former. It reduces the latency by about the peaking time and at the same time

allows the use of longer integration time which results in lower electronic noise and higher charge collection. While the direct outputs are active simultaneously with all modes of operation they are not needed in Micromegas. It must be possible to turn off the SLVS drivers in order to reduce power consumption and the possibility of digital interference with the front end operation. The ART latency is the sum of several delays the time from instantaneous charge event to 1% of the peak is ∼10 ns the time from pulse peak to peak found ∼5 ns, digital latency from comparator firing to leading edge of ART is ∼5 ns and digital latency from peak found to leading edge of ART is 5 ns.

CHAPTER 4

STUDIES OF THE OUTPUTS OF THE VMM2 AND VMM3 ASIC WITH MICROMEGAS CHAMBERS

This chapter contains the data analysis of MicroMegas chambers using the new readout chips, the VMM ASIC. MicroMegas chambers readout at test beams was always implemented with the readout system from the raw channel data of the APV25 chip. The APV25 is a 128-channel analogue pipeline chip for the readout of silicon microstrip detectors [52]. Data acquisition and saving into ROOT ntuples via the mmDAQ [53] needed a generic framework for reconstruction of the raw data in order to allow the users of the collaboration to perform in a coherent manner.

These raw ntuples are processed and reconstructed from the RecoMM framework [54] that was developed within the Muon Atlas MM collaboration. Data reconstruction is done at steps. A first pre-processing of the data is done with some filter options such as noisy strips, cross-talk strips etc. For each different experimental set-up these options can be enabled or disabled. Recomm was built on C++ libraries and has many options and configuration parameters like processing, clustering the strips position, timing, charge etc.

In the NSW the Micromegas and sTGC chambers will use the VMM chip for the same purpose. The VMM chip is no longer saving in raw ntuples but data are already configured for analysis and can be used directly. In this thesis data from VMM2 and VMM3 ASIC were used and the processing, charge and timing distributions etc were implemented later with dedicated algorithms. The resistive Micromegas chambers were the SM1, LM2 prototypes and a T-chamber. VMM2 chip was the readout on the prototypes while the VMM3 was used on the T-chamber. We used two radioactive isotopes the Strontium 90(^{90}Sr) for the VMM2 measurements and in the last section with the VMM3 readout, the Iron-55.

The analysis was implemented with the ROOT Data Analysis Framework. ROOT is a powerful scientific software framework, ideal for big data processing, interaction, statistical analysis, visualisation and storage [55]. Root was created at CERN for the

needs of high energy physics research. The integration is done in $C++$ but other languages can be also used.

4.1 Description of the VMM and Experimental Setup characteristics

4.1.1 VMM Specs and signal acquisition

VMM2 was the chip used mostly for the readout in the experimental setup but also analysis was implemented in the last section of this thesis with the VMM3 ASIC. The chips equip the front end boards and every one of them has 8 chips.

Each chip has 64 channels. The channels are equipped with low noise charge amplifier and a shaper [56] which provides baseline stabilisation and a discriminator with trimming capability. Digital to Analog Converters (DAC) are used for adjusting the amplitudes and the internal pulser. For the MM detectors the address of the channel with the earliest arrival time is used for trigger primitives and is called Address in Real Time (ART). This is very useful because it reduces the trigger channel count from approx. 2 million to 32000.

VMM provides measurement of the peak amplitude and time with respect to the trigger signal. The single channel signal is amplified and shaped and then is compared to the threshold value which is set by the Time - over - Threshold or Time - to - Peak detection circuit. The Charge amplification and shaping provides adjustable gain(0.5, 1,3 and 9 mV/fC) and peaking time (25,50,100 and 200 ns). Then the channels that have signal above threshold are processed for peak and timing measurements.

When the peak is detected a Time - to - Amplitude - Converter (TAC) is initiated and stopped by a signal from the DAQ system. Then the read out is done serially by a token which gives information about the channel (strip), charge and time measurements of signals above threshold. There is also the capability to read signal from channels below threshold. This is done with the neighbour read out logic enabled. When this is on, the VMM process the data not only from channels above threshold but also to the adjacent channels.

Table 4.1: The VMM ASIC specs

Technology	130nm
Channels	64
Adjustable gain	0.5,1,3,4.5,6,9,12,16mV/fC
Adjustable peaking time	25,50,100,200 ns
Pulse generator	10-bit adjustable, 1mV
Configuration	1072-bits
ART	Adress in Real Time
Time to Amplitude Converter	125ns,250ns,500ns, 1 μs

All the channels have been individually calibrated using the built-in pulser of the VMM. This was done in order to have equal response of all VMM channels for the charge and timing measurements but also triggering and low signals accurate read out capability. This procedure is further described in [18] and [30] .

4.1.2 MicroMegas Chamber specs and setup

At first data from SM1 module were used. Then data from the LM2 chamber but with a later version of the MMFE8 board. The runs are including data from the MMFE8 board with all the chips on but also some measurements with only the VMM in the position 5 on.

Also although the drift gap Field was always at 300 V the amplification field was changed between 580-640 V. In the NSW the amplification field will always be at a preset value but in our studies in order to explore the overall behaviour of the chamber and the VMM chip the field was increased in every run so in every section the parameters of each plot will be specified.

Table 4.2: MicroMegas Module Specs

MicroMegas Chamber	SM1 & LM2
Strip Pitch	425 & 450 μm
Strip width	300 μm
Gas mixture	Ar+7%CO_2
Amplification Gap	128 μm
Drift Field	-300V
Amplification field	580-640 V

4.2 Performance studies

In this section the procedures done stepe by step are going to be described in order to study the VMM chip performance and different measurements and outputs that may occur due the increased amplification field values. Firstly some tests were done to extract charge (pdo), timing and hit positions directly from the VMM ASIC. All the procedures will be further explained in the sections to follow.

4.2.1 Tests for PDO,TDO,BCID and Beam Profiles

While in the NSW the values of the Amplification Gap will be at a nominal value in our studies different Amplification field voltages were used in consecutive Runs. Also the VMM chips of the MMFE8 in some cases were masked and retrieved the values of only one chip but in other cases all the chips were on. The following plots are from all

the consecutive runs and demonstrate the retrieved values from the basic variables. As described before, the tool we used is the ROOT Analysis Framework.

When a channel has charge above threshold the signal is processed for peak and timing measurements. After the peak is detected the Time - to - Amplitude Converter (TAC) is initiated and then stopped by another signal from the DAQ system. After the event is processed a flag is raised and this set of amplitude and timing measurements are available from the analog outputs PDO (Peak Detector Output) and TDO (Time Detector Output).

After this information is read out the user retrieves diretly the channel number above threshold which corresponds to a strip number with the MMFE8 board set up. Address in Real Time (ART) information is provided from the VMM ASIC which corresponds to the first chip above threshold in an event.

It receives synchronously with the Bunch Crossing (BC) clock the ART signals and encodes the strip address of the VMM with the hit and gives an ID to the BC (BCID) and then the data is transmitted to the MM trigger. VMM ASIC is very useful displaying the results of every Run and data are available for reading, manipulation and processing without reconstruction frameworks further interference. Those outputs are saved to ROOT ntuples and for our setup firstly with the SM1 chamber and for Different Amplification fields are shown below.

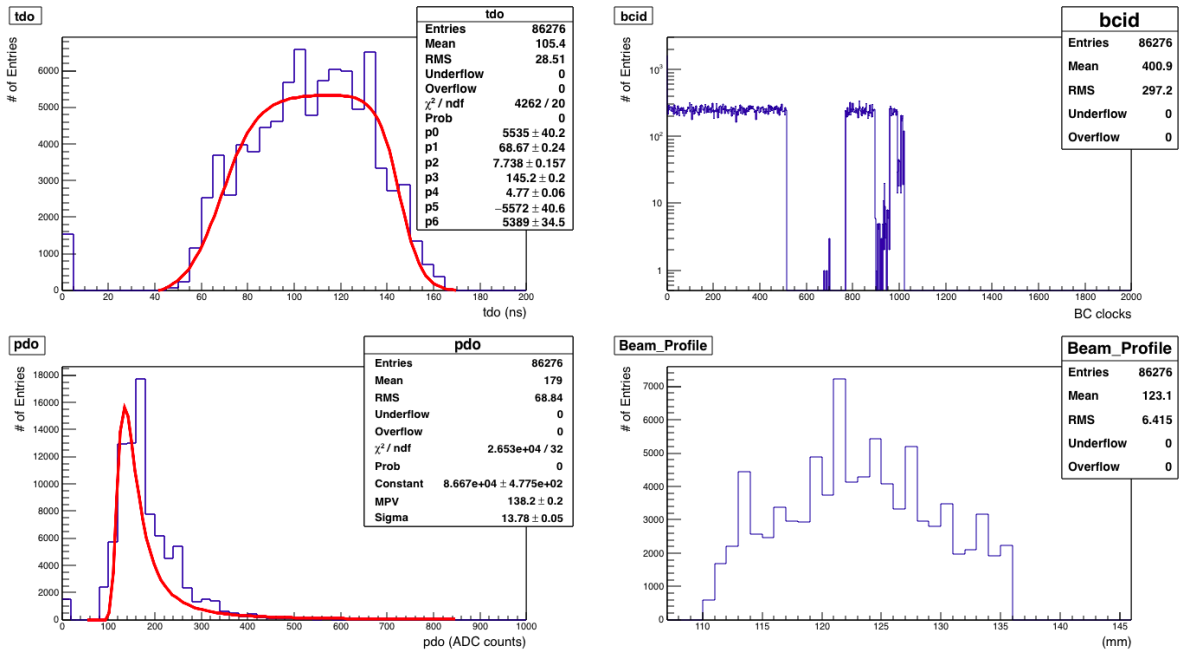

Figure 4.1: Amplification Field at 580 Volts, activated only VMM in position 5

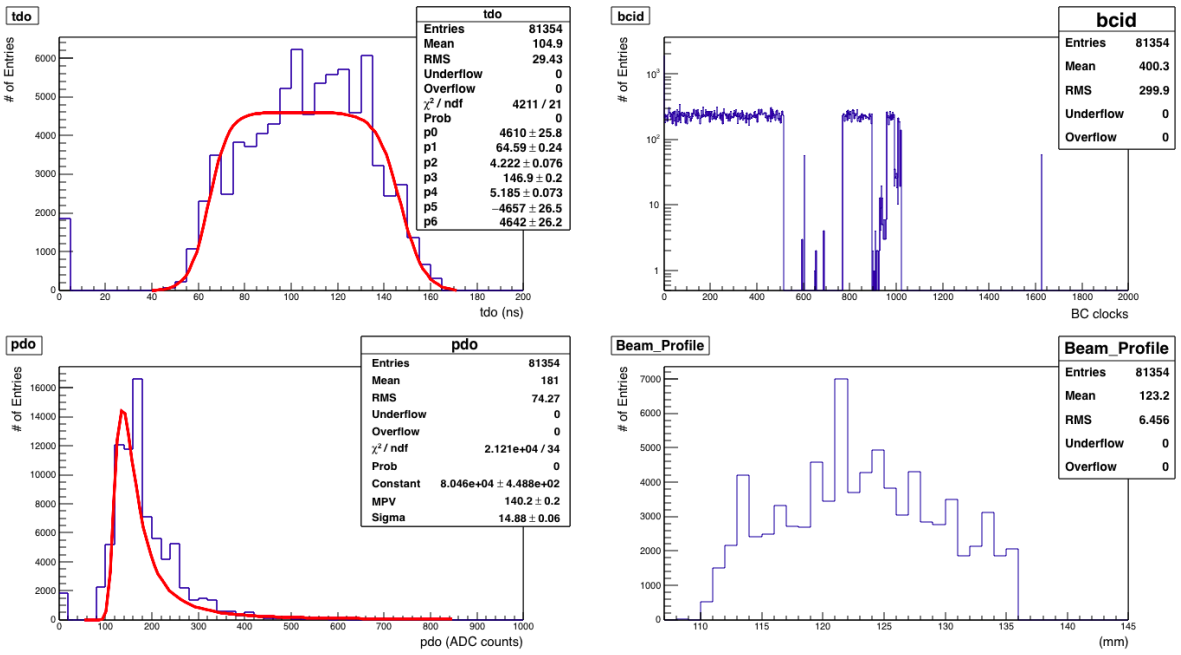

Figure 4.2: Amplification Field at 590 Volts, activated only VMM in position 5

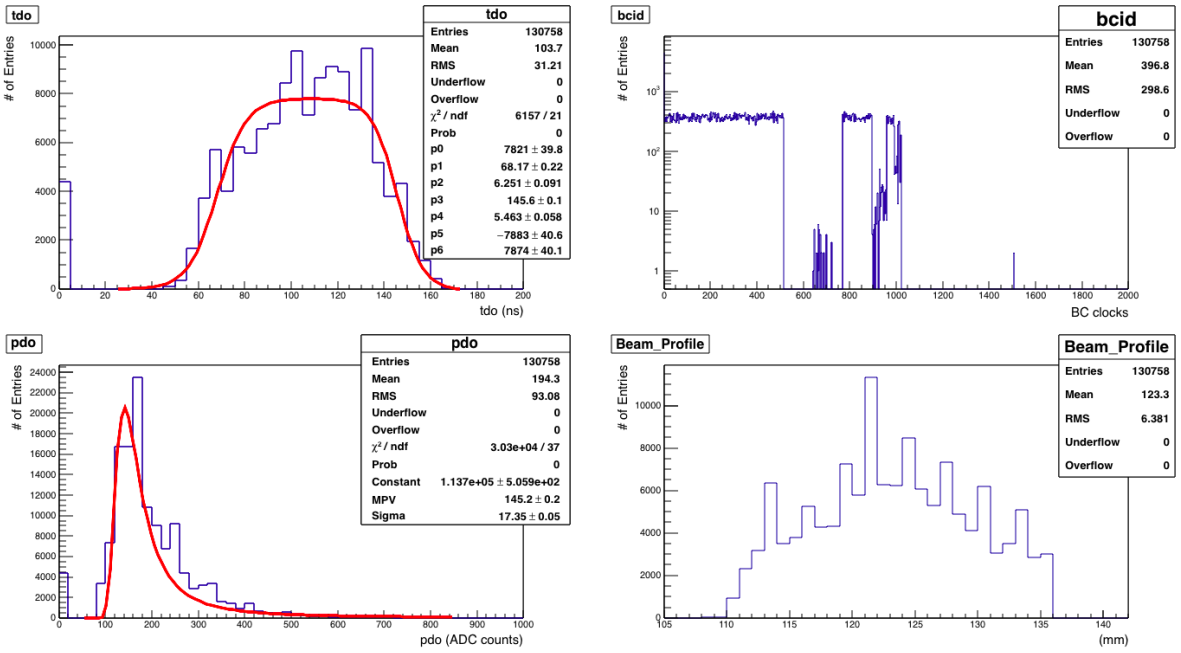

Figure 4.3: Amplification Field at 600 Volts, activated only VMM in position 5

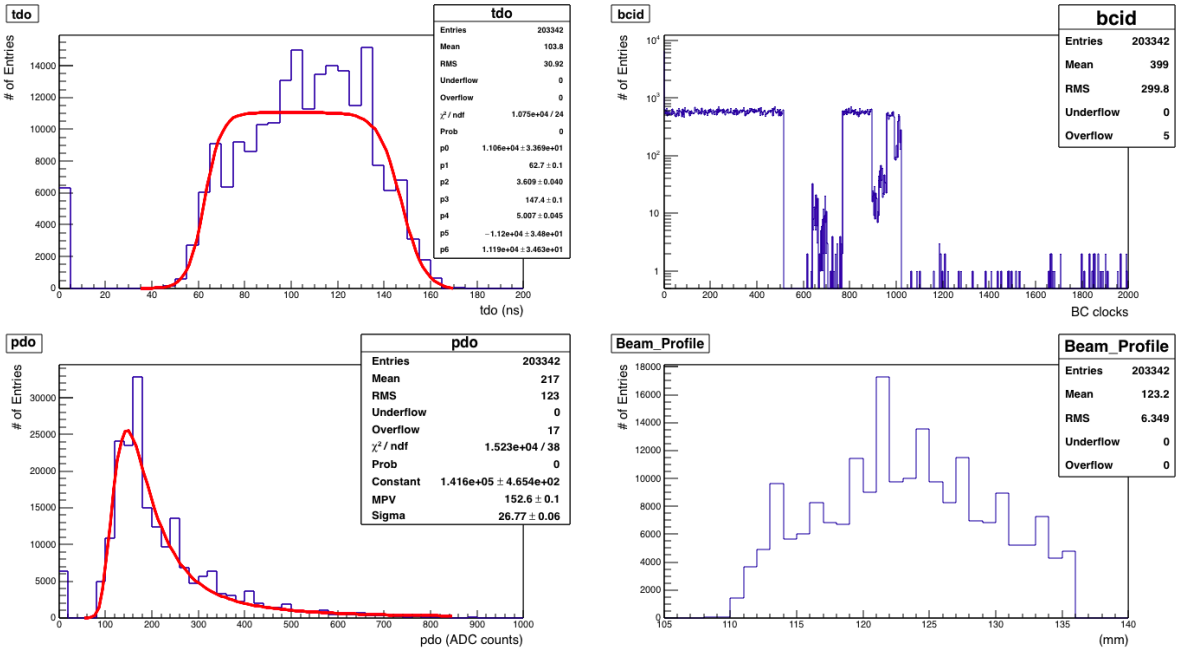

Figure 4.4: Amplification Field at 610 Volts, activated only VMM in position 5

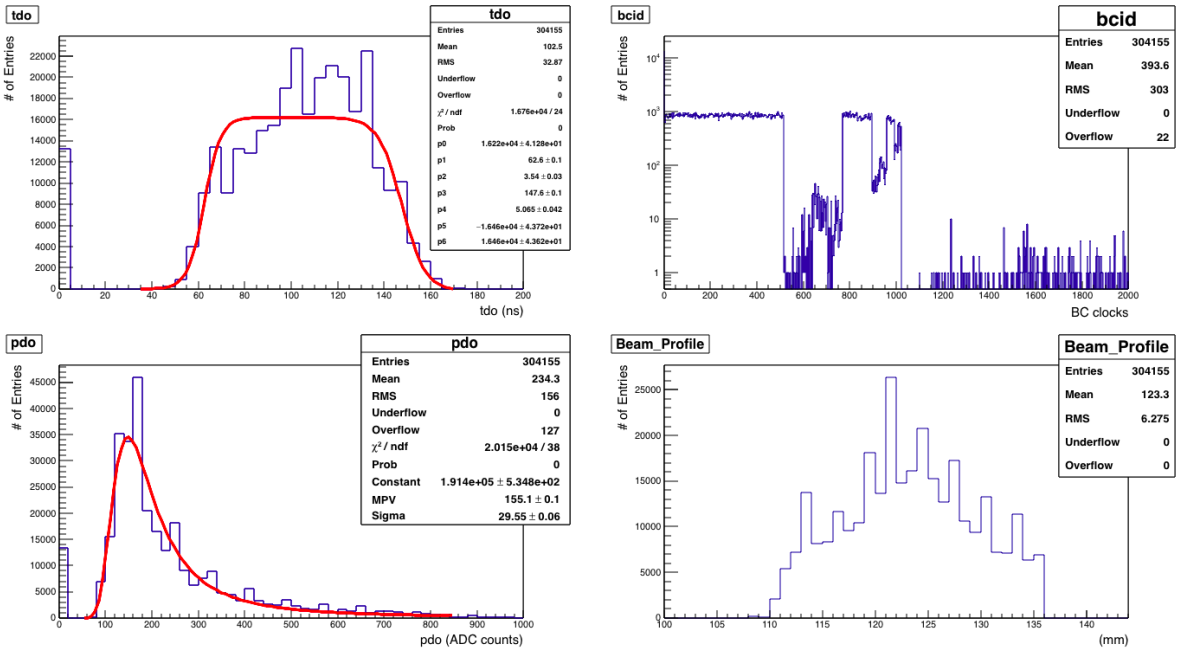

Figure 4.5: Amplification Field at 620 Volts, activated only VMM in position 5

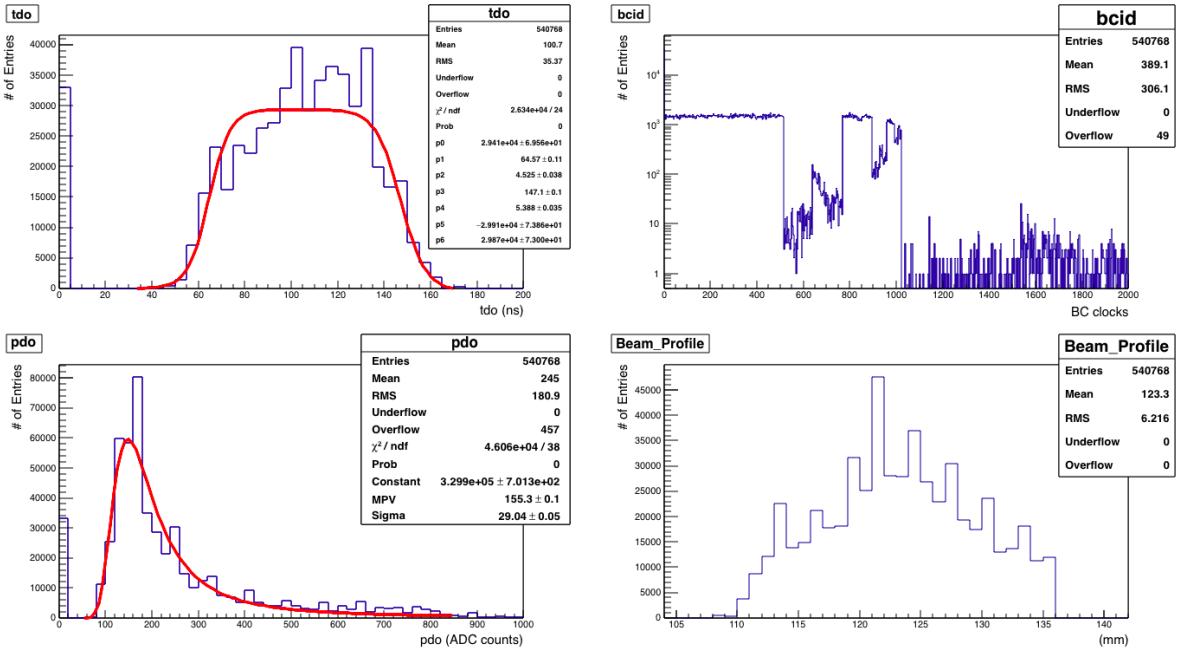

Figure 4.6: Amplification Field at 630 Volts, activated only VMM in position 5

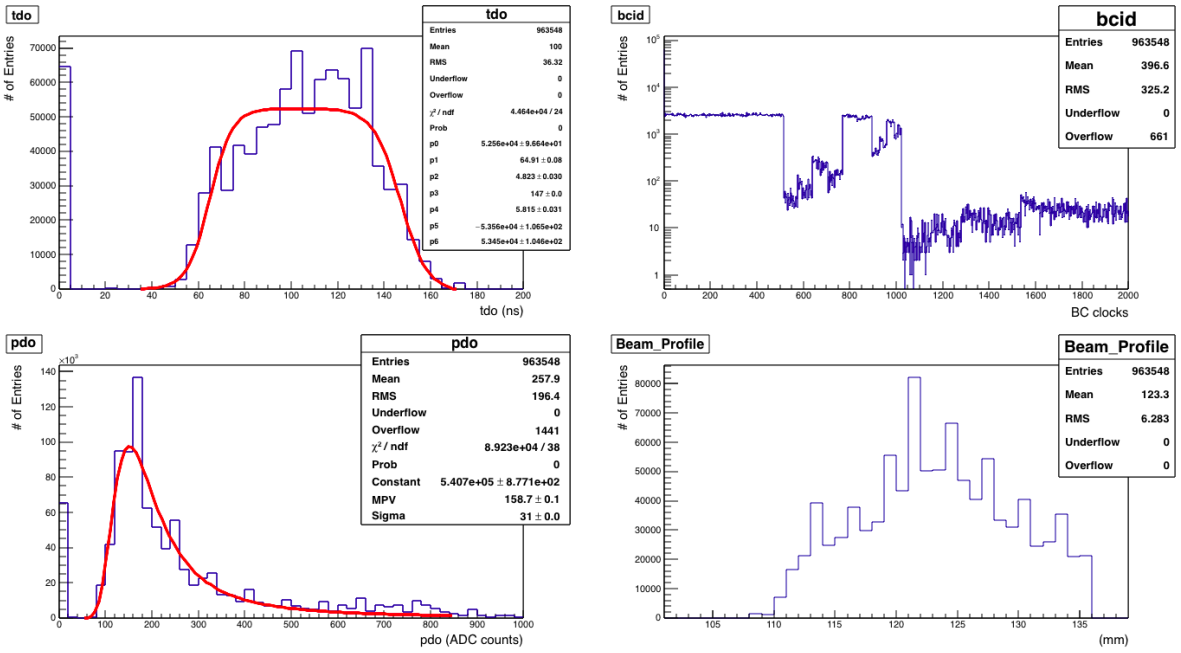

Figure 4.7: Amplification Field at 640 Volts, activated only VMM in position 5

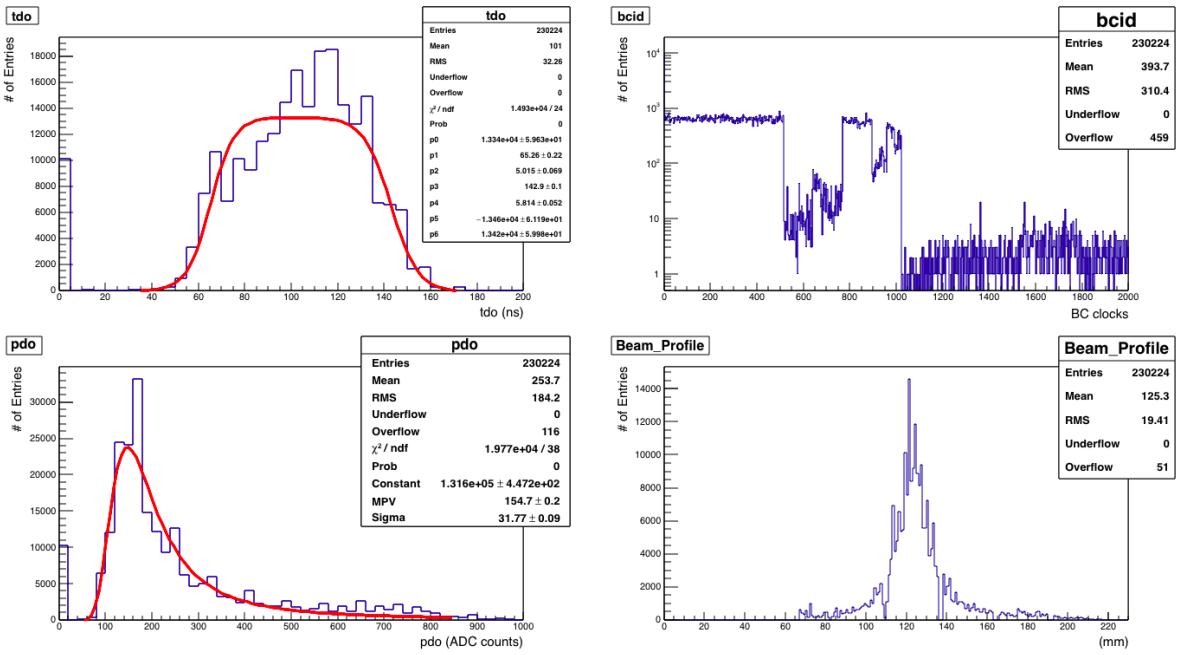

Figure 4.8: Amplification Field at 610 Volts, masked only VMM in position 2,3

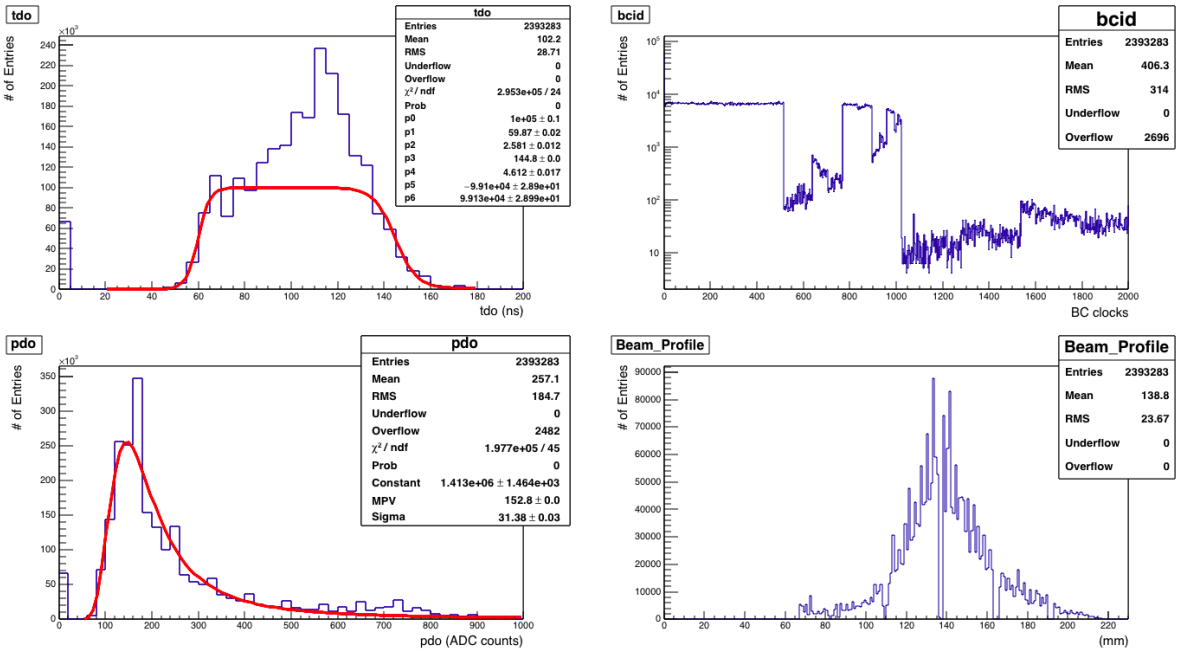

Figure 4.9: Amplification Field at 610 Volts, masked only VMM in position 2,3 and raised source above chamber $\sim 10cm$

The tracks are perpendicular to the chamber for every run. Beam profiles above are for the conditions described in each caption. As expected increasing the HV values differentiates the results. In the two last figures the beam profiles are for only two VMM chips masked and we can see better the distribution and placement of the hits from the Strontium. The empty spots in some positions is a result of the fact that the first six channels of each chip are not in working order. Pdo is increased with the increasing values of the HV. Higher amplification field is creating biggest tail and values at higher ranges for the Pdo. Pdo is fitted with a Landau function:

$$\varphi(\lambda) = \frac{1}{2\pi i} \int_{c-i\infty}^{c+i\infty} e^{\lambda s + slogs} ds \tag{4.1}$$

Where $\lambda = (x - x_o)/\xi$. The parameters are the argument x, the width parameter ξ and the location parameter x_o [57]. TDO is converted to ns using the calibration constants. Measurements are fitted with a double Fermi-Dirac function. This method was used to encounter the slope rising on the one side of the plot and decreasing on the other. The above fit parameters were the best possible due to the fluctuations of the measurements. The F-D function for the fitment is :

$$F(t) = \frac{p_0}{1 + e^{(p_1 - x)/p_2}} + \frac{p_6}{1 + e^{(x - p_3)/p_4}} + p_5 \tag{4.2}$$

We can derive each parameter of the Fermi Dirac from the plots. The parameters p_0 and p_6 are the maximum height of each F-D to the x-axis, p_1 and p_3 are the mean of the rising and decreasing function, the p_2 and p_4 are the parameters proportional to the slope and p_5 is the base value. The mean value of number of strips that had pdo above threshold in each Run was derived and in the fig.4.10 is presented as a function of the different amplification fields.

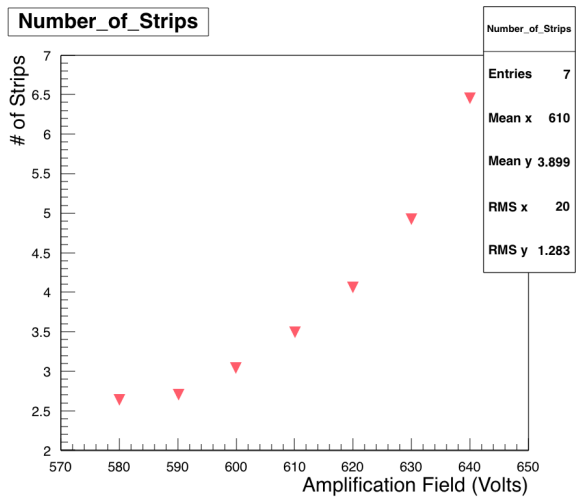

Figure 4.10: Strips opened for the different Amplification Field of each Run. Over 600V we see the number of strips opened rising faster .

4.2.2 Clustering

VMM chip can give as measurements about the strips that had pdo above threshold in each event. So for every event a topological clusterisation is applied. The cluserisation algorithm checks for adjacent strips that had pdo signal above threshold and defines this sum, as a single cluster. An event can have multiple clusters from the transversing particles. After this procedure is done the algorithm processes all the data information into clusters. VMM chips have some channels that are not efficient and in some events a single channel gap in the cluster is created. The algorithm can recognise the single strip gaps and merges the two clusters of this inefficiency into one. This way spoiling the clusterisation is avoided and leads to better statistics. VMM gives information for every bunch crossing of each event. Some more requirements were added such as the strips of a cluster are between a range determined from the bunch crossing and by this way back to back particles of an event can be recognised.

Duplicate Clusters Removal

Due to manufacturing issues, crossfire channels and efficiency problems, the data retrieved, required further processing before the clusterisation. A correction for the cluster measurements was needed. This was the duplicate channels issue which is related directly with the duplicate clusters issue. In some measurements it seemed that a strip has opened twice, in the same event and had exactly the same values in all their variables.

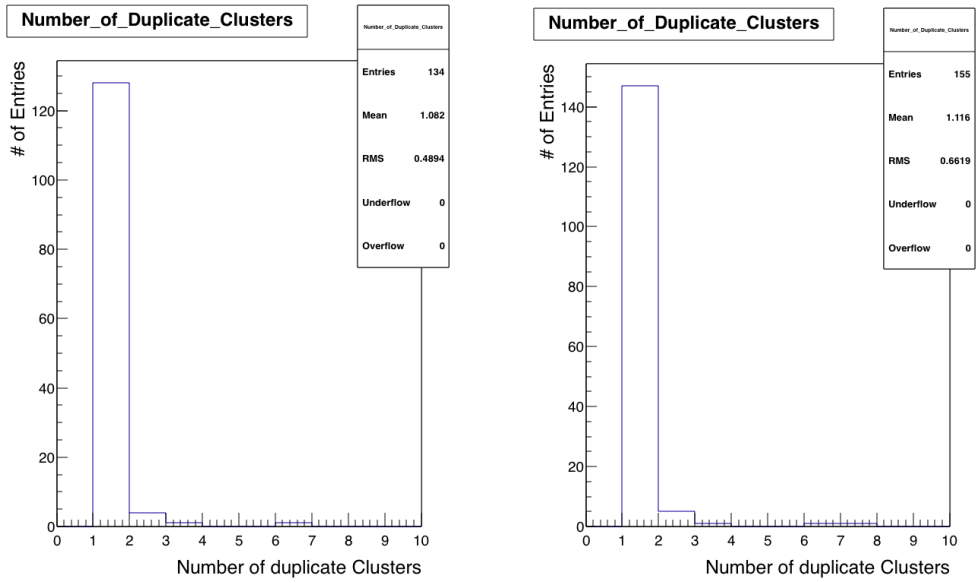

(a) Amplification Field 580 V (b) Amplification Field 590 V

Taking exactly the same pdo, timing, bcid etc measurements twice for a channel in the same event is not efficient. So an algorithm was implemented which can search

and when it finds a duplicate in an event can erase this. Afterwards that all the variables were measured for clusters a similar algorithm was applied which could find and remove the duplicate clusters. Most events that had duplicate clusters only had one but as seen at the plots that follow the duplicate clusters can be more in some events. The rest of the plots for the duplicate cluster number are below:

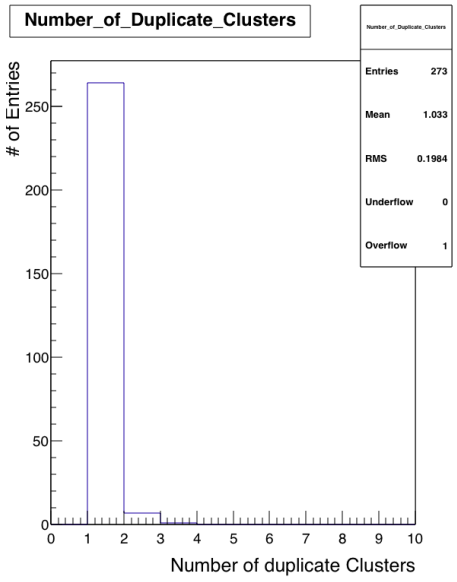

(c) Amplification Field 600 V

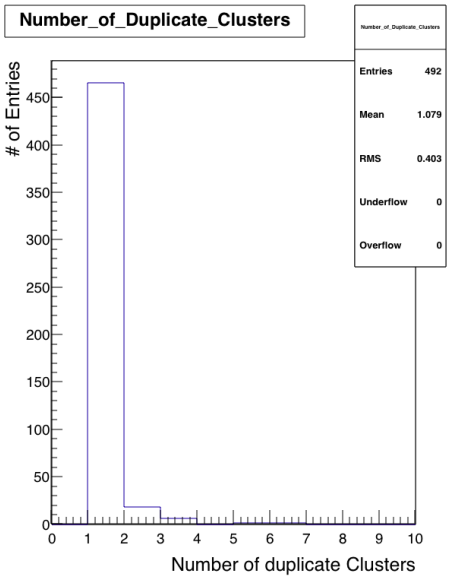

(d) Amplification Field 610 V

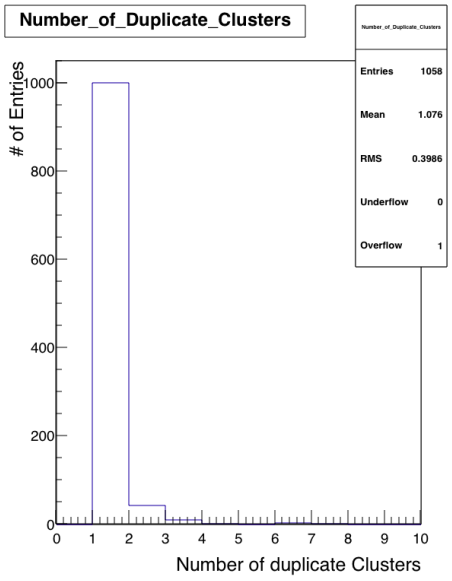

(e) Amplification Field 620 V

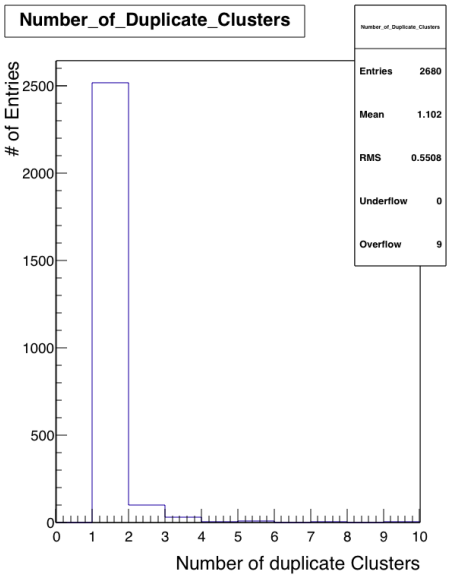

(f) Amplification Field 630 V

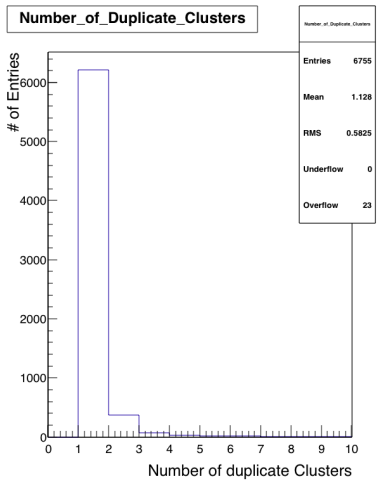

(g) Amplification Field 640 V

Figure 4.11: All the Duplicate clusters found for each Run.All those Runs had only one VMM chip on.

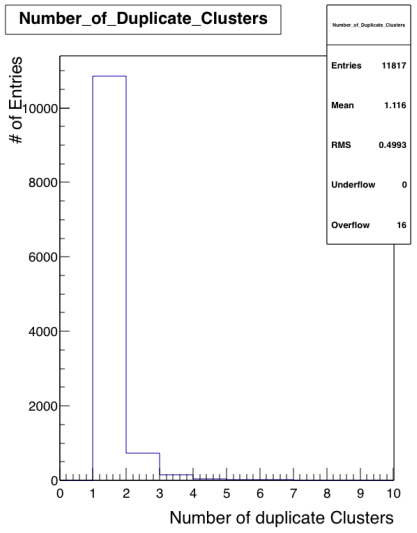

(a) Amplification Field 610 V

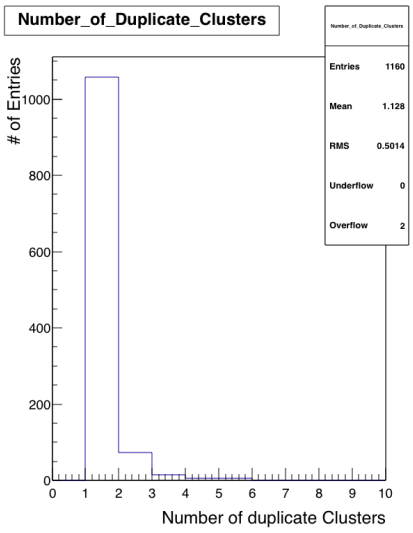

(b) Amplification Field 610 V

Figure 4.12: Two Runs will all VMM open.Although there is the same Amplification Field and (a) has more duplicates it was a Run with more entries and the duplicate percentage is very close for both.

In order to derive a result for the duplicates we made a plot with the duplicate percentage. This refers to the percentage of all the entries to the duplicate entries. As a function of the Amplification Field we can see below:

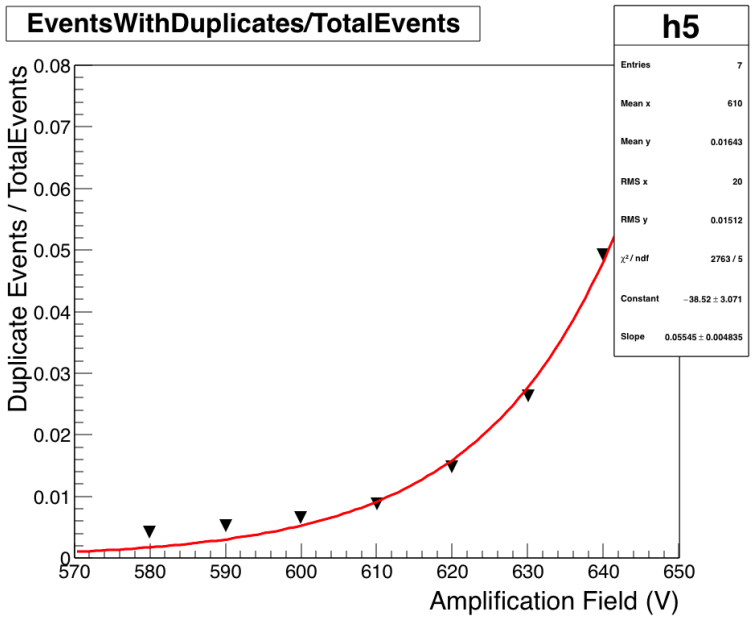

Figure 4.13: Duplicates Events to Total Events as a function of the Amplification Field. Duplicates are erased from our data so the analysis can go further without being affected by duplicates.

After the duplicate clusters are removed the clusterisation is finished and we can see the clusters before and after the duplicate removal below. Of course cluster mean value differentiates as increasing the ampl. field :

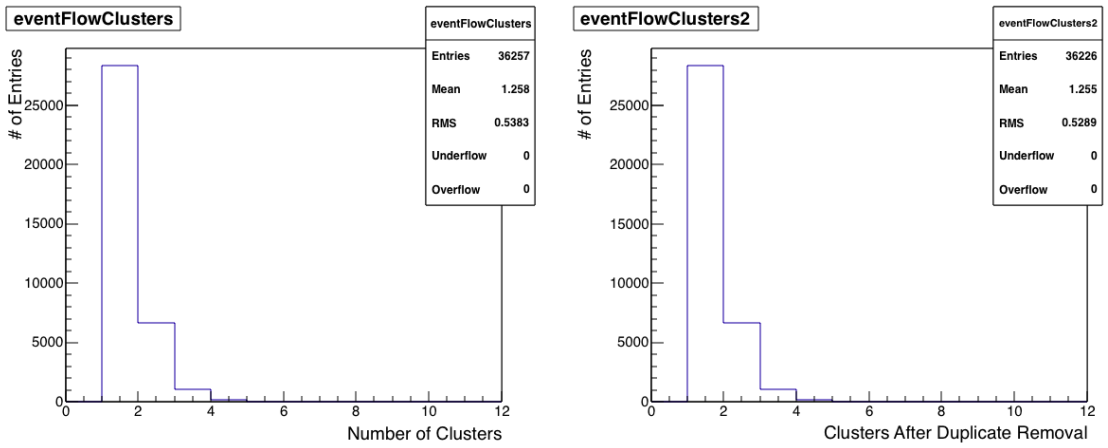

(a) Amplification Field 580 V

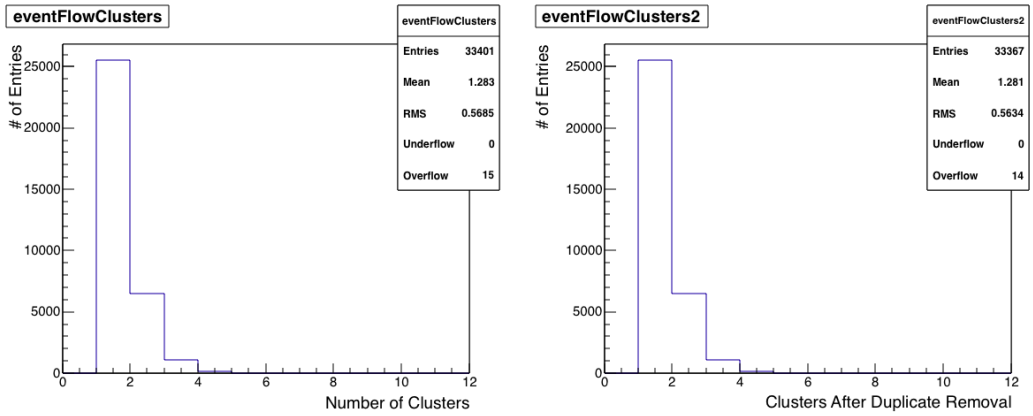

(b) Amplification Field 590 V

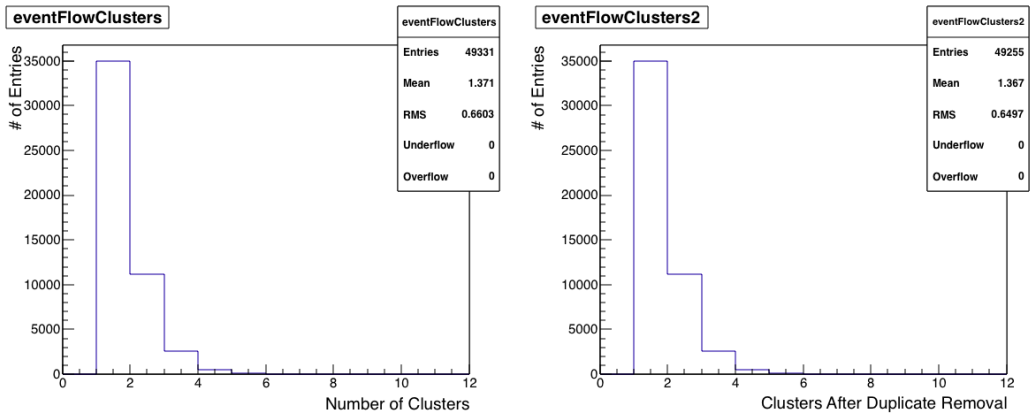

(c) Amplification Field 600 V

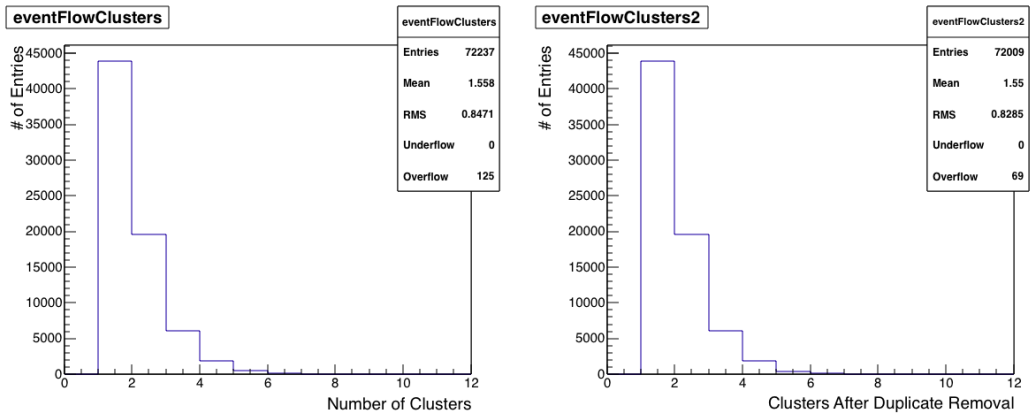

(d) Amplification Field 610 V

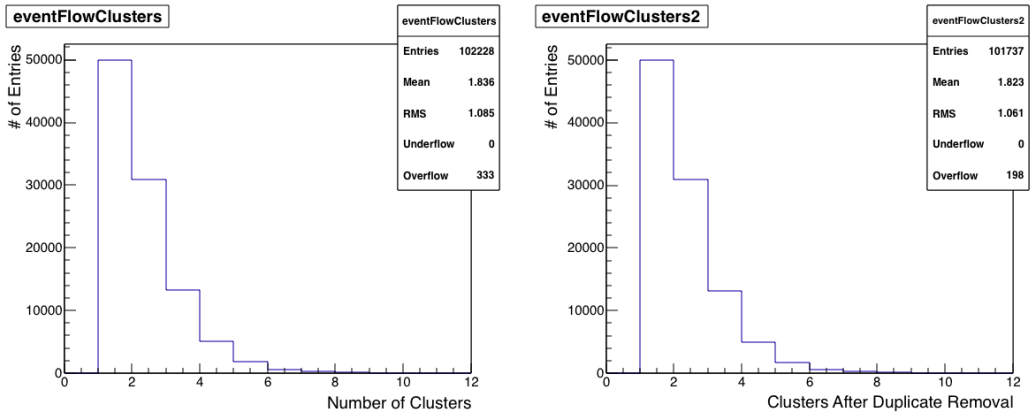

(e) Amplification Field 620 V

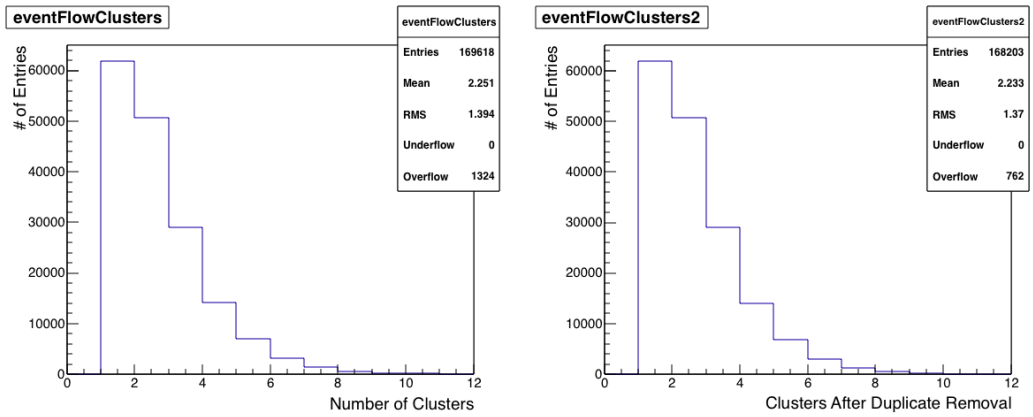

(f) Amplification Field 630 V

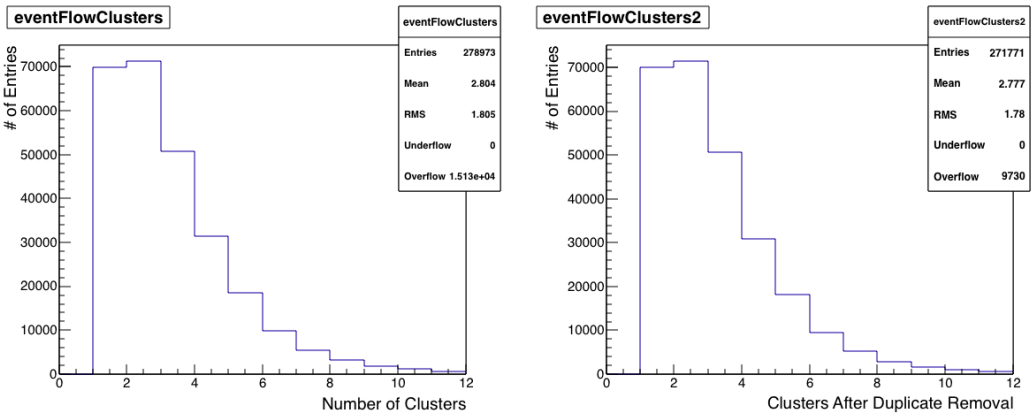

(g) Amplification Field 640 V

Figure 4.14: Number of clusters before and after duplicate removal. Every Run has been affected from the duplicates which have been removed and so we can process clusters data without duplicates

4.2.3 Weighted Cluster Position

In our studies for the SM1 chamber a Strontium 90(^{90}Sr) source was used. Since the beam axis was perpendicular to the chamber we used the Centroid method to reconstruct the position of the clusters. Centroid method is very accurate for hit reconstruction in perpendicular tracks. We used the clusterisation algorithm to get the charges of each strip of the cluster. Then the charge of each strip and the position is reconstructed with the center of gravity. This method is widely used in MM chambers. The position can be calculated with the equation:

$$P = \frac{\sum_{i=1}^{n} x_i q_i}{\sum_{i=1}^{n} q_i}$$

The x_i,q_i coefficients are the center of strip pitch and charge(pdo). Below we can see the cluster position for Runs with only the VMM in the position 5 of the MMFE8 on and with all the chips on:

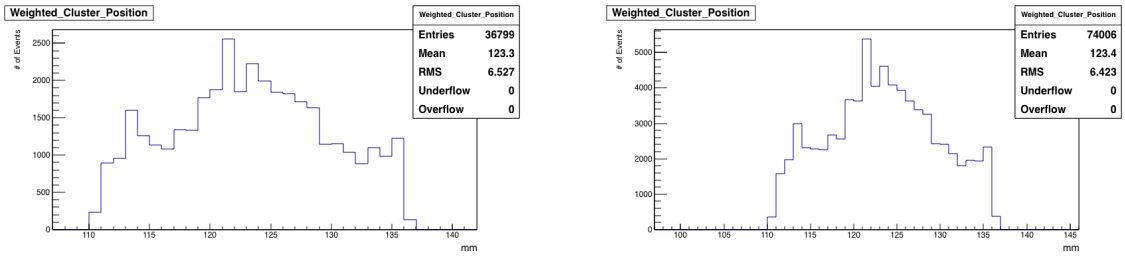

(a) Amplification Field 580 V (b) Amplification Field 610 V

Figure 4.15: Weighted Cluster Position for only one VMM on.

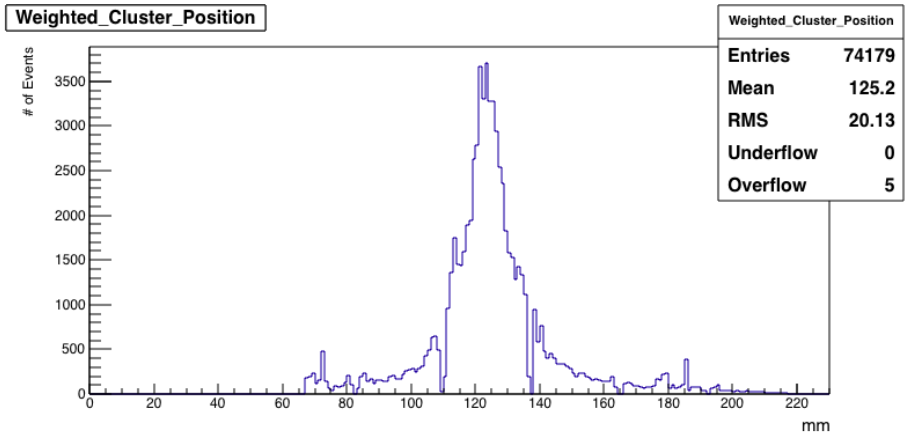

Figure 4.16: Weighted Cluster Position for all the VMM on.

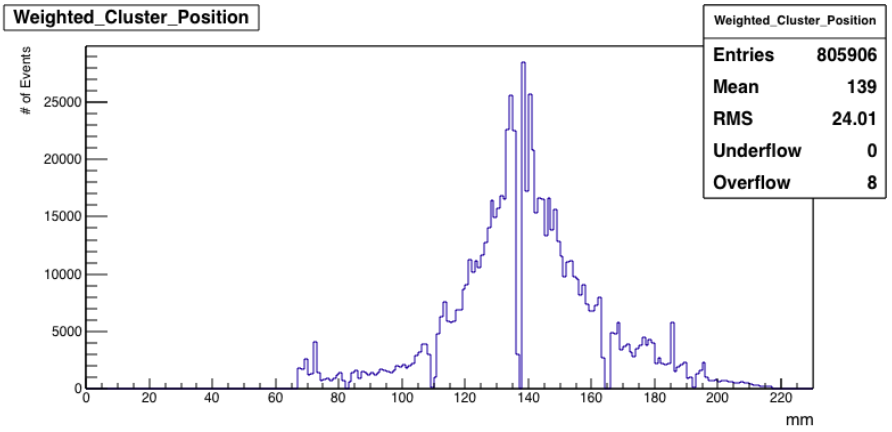

Figure 4.17: Weighted Cluster Position for all the VMM on and source raised above chamber.

4.2.4 Peak Detector Output and Timing for the clusters

The charge distribution(pdo) of the clusters and the timing outputs were measured. Pdo results are represented below :

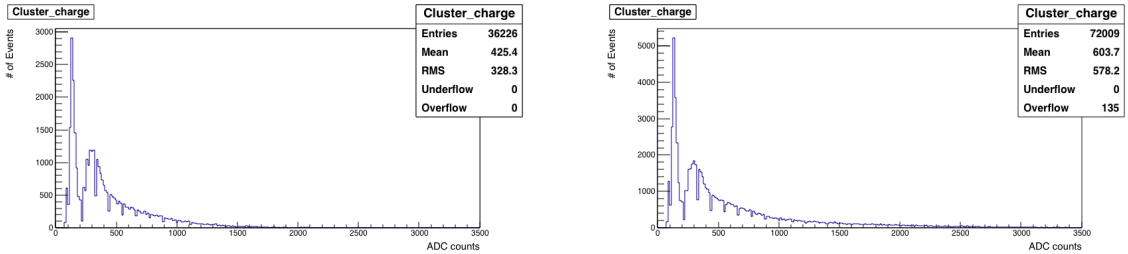

(a) Amplification Field 580 V (b) Amplification Field 610 V

Figure 4.18: The cluster charge (pdo) for 580 and 610V. As seen in the range of the ∼60-220 there is a big number of entries. Further research was done to find out the reason of the background.

At the range of 60-220 ADC counts there is a high rate area of non efficient entries. This causes issues and affects statistics in all measurements from the cluster positions that are directly depended from the charge, to cluster numbers etc. The charge measurements are usually fitted with a Landau function but without removing the background it could not be possible to do. Several pdo and tdo measurements were done for the each channel of the VMM2 on the MMFE8 board to find the cause and perform a correction to remove those entries. The electronic cross-talk between the channels has already been measured and it didn't affected the data so some tests

were performed in order to determine if there was a faulty channel that caused the inefficiencies.

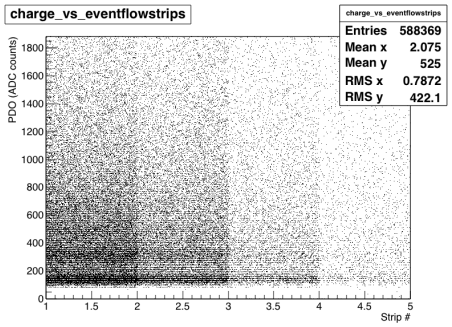

(a) The Pdo of the clusters as a function of strip number

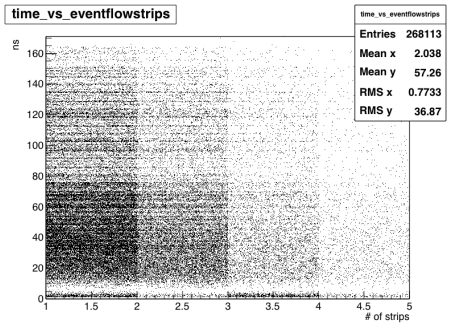

(b) The time detector output as a function of strip number

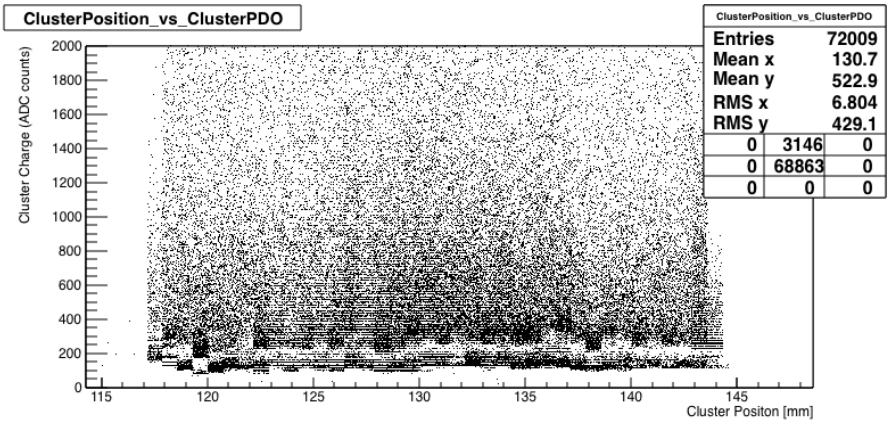

(c) Positions of clusters reconstructed with the centroid method as a function of cluster pdo, with only one VMM activated

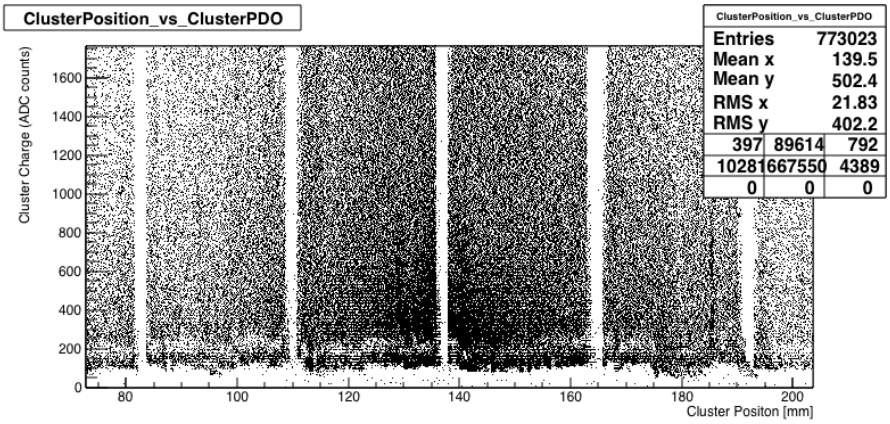

(d) Same as c but with all chips activated

Figure 4.19: Diagram a,b,c and d are all with the Ampl. Field of the 610 V.

The same plots were performed for all the different runs and amplification fields. As seen especially from (c),(d) there is not a correlation of a specific channel and pdo or timing. This research though made possible to derive the exact area of the noise. A correction cut was performed at this area and then the measurements were divided in three: before the correction, the background area and after the background removal. Diagrams are introduced below:

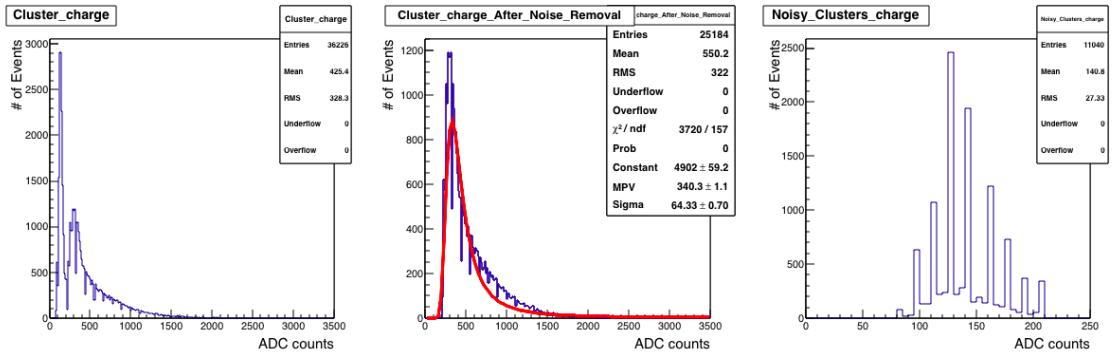

(a) Amplification Field 580 V

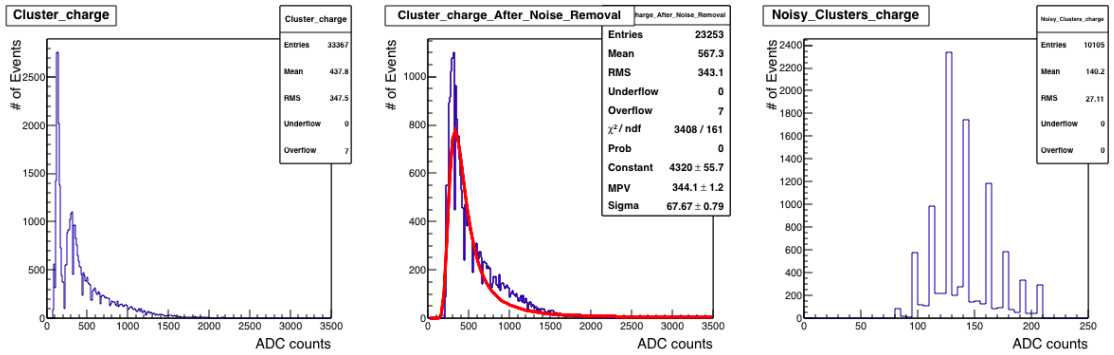

(b) Amplification Field 590 V

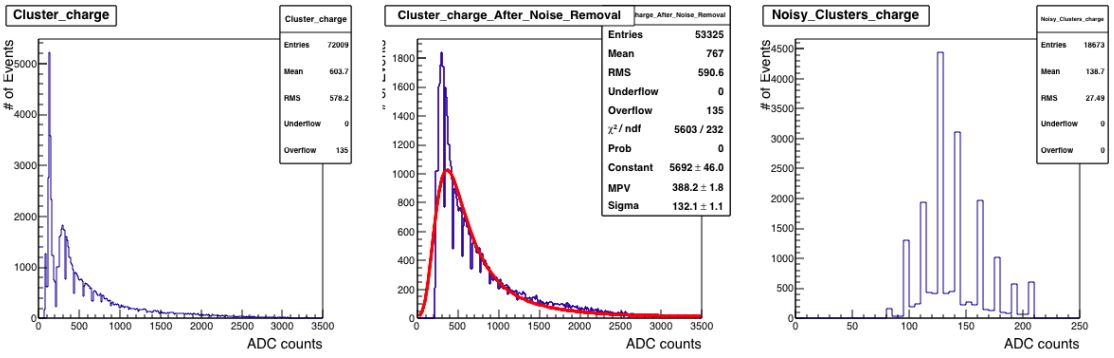

(c) Amplification Field 610 V

Figure 4.20: The cluster charge (pdo) for 580,590 and 610V. Cluster charge after background removal is fitted with the Landau function

After the determination of the exact range of the noisy clusters charge and the correction, the total cluster charge is fitted with a Landau function. For the current MMFE8 set up it was the best possible. Peaks at the 300-400 counts area especially with the higher amplification field values affects the measurements and fit functions although in some, a convolution of Gauss and Landau function was used. This was the case for all the Runs with the current set up for the SM1 chamber.

Timing of the cluster strips

Timing detector output is converted in nanoseconds with the calibration constants. After the clusterisation, the timing of the fastest cluster strip is calculated from the bunch crossing identification VMM provides. Then with a scheme that calculates the calibration constants, the converted timing and BC identification of each strip, compared to the first one, we can derive the timing of each strip of the cluster. Timing is segmented in three areas same as PDO measurements.

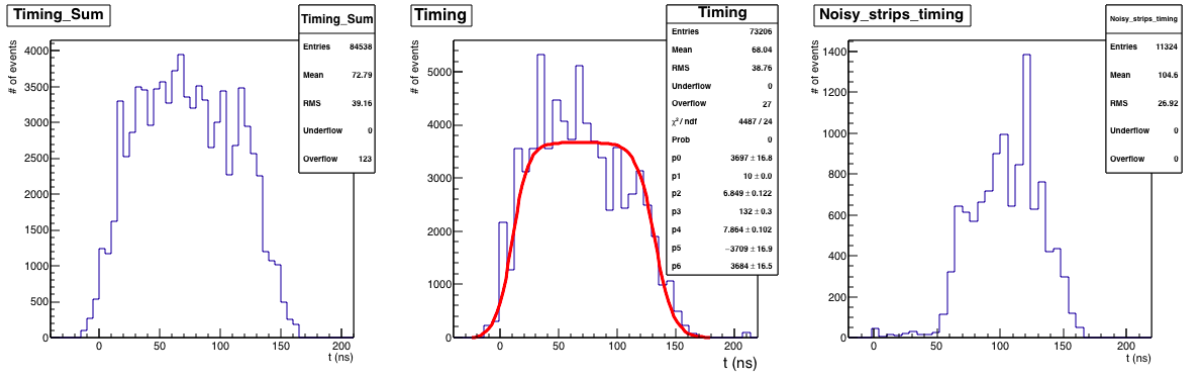

Figure 4.21: Time Detector Output for 580V

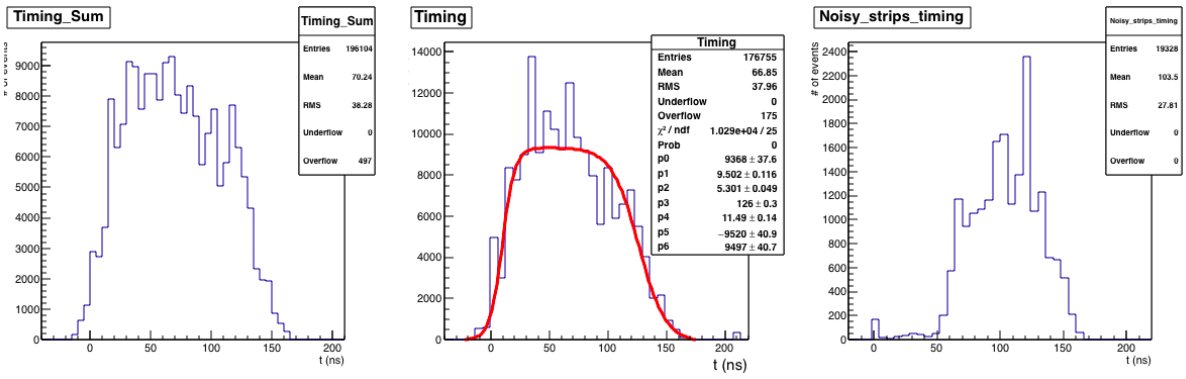

Figure 4.22: Time Detector Output for 610V

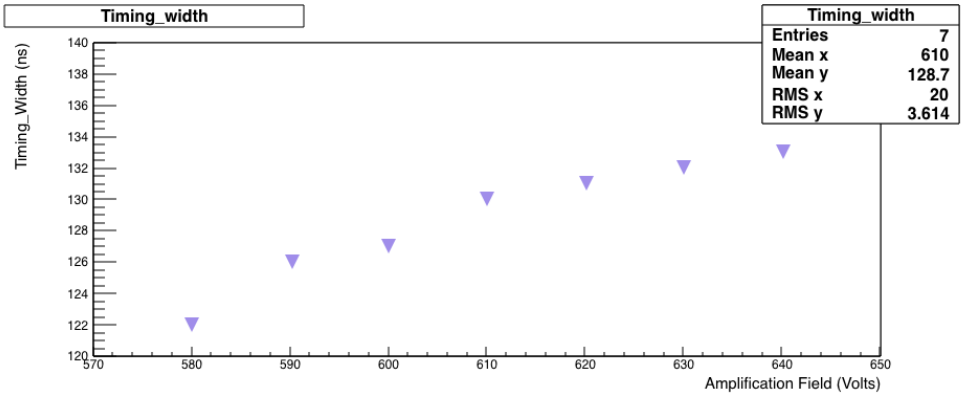

Figure 4.23: Fitted with a double Fermi-Dirac function we derived the timing width of every Run.

From the double Fermi Dirac function timing width was measured for the outputs of the VMM in the SM1. As seen the fluctuations make it hard to get the fit parameters as showed indicatively for two Runs. With further fine tuning of the parameterisation, timing widths for all the Runs (fig.4.23) were defined. This output of the timing with a mean value of 128 ns is larger than expected but from the measurements but this was corrected in the LM2 chamber which had a later version of the MMFE8 board.

4.2.5 Strip cluster multiplicity

The electrons drift to the amplification area of the chamber and end up to more than one strips, average 2-4. Especially in events where the particle has an angle the number of strips can be even bigger. Also it is affected by the amplification and magnetic field. In figure 4.24 we can see the cluster multiplicity analytically for different amplification fields.

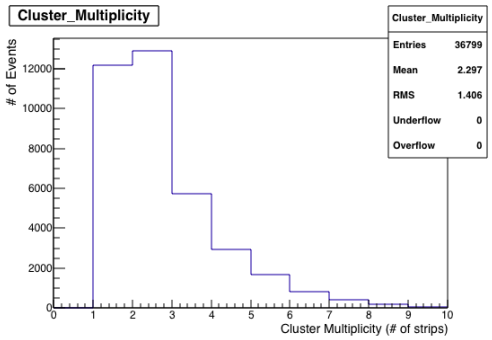

(a) Amplification Field 580 V

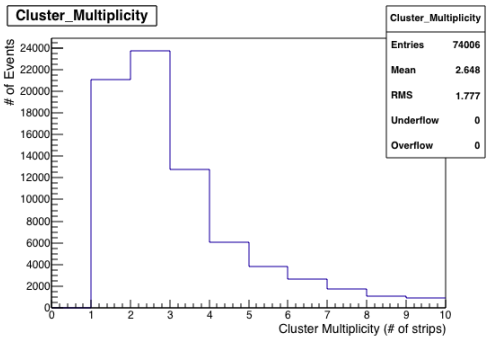

(b) Amplification Field 610 V

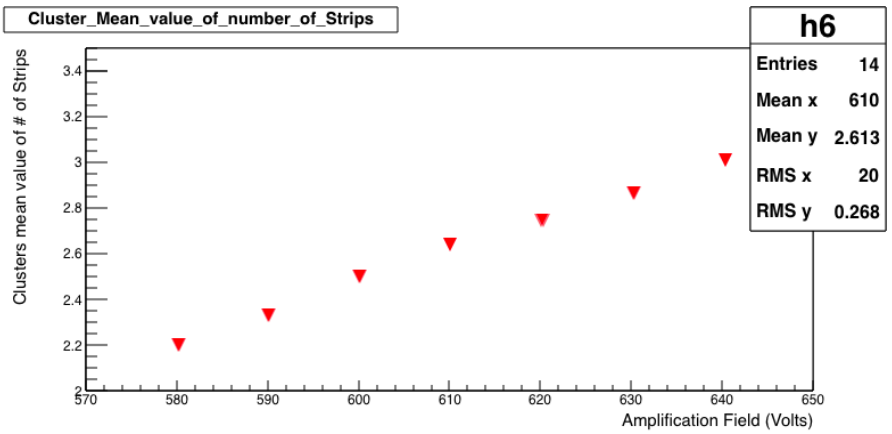

Figure 4.24: Mean Values of the Cluster Multiplicity for the different amplification Fields. As expected for higher amplification fields the number of strips is rising.

Strip cluster multiplicity is very helpful especially to position reconstruction. The mean value for each run is shown as a function of the Amplification Field. No more requirements were added except for zero clusters events to be removed. This was done with the requirement that pdo of the strips at the clusterisation have charge above threshold to avoid zero charge strips. As the measurements of pdo appointed some more requirements were added.

From the cluster multiplicity is derived the reason such a noise area existed in the first place. Single inefficient strips are creating areas at the range of 60-220 ADC counts with the high rate background. The single strips are also creating a wrong mean value for the number of strips of the clusters as seen in figure 4.24 with a mean value of 2.61 strips. This number was derived at 3.19 strips per cluster after removing the noisy strips, mostly single strips. After the same correction cut was performed to the strips size of the clusters and for the three areas:

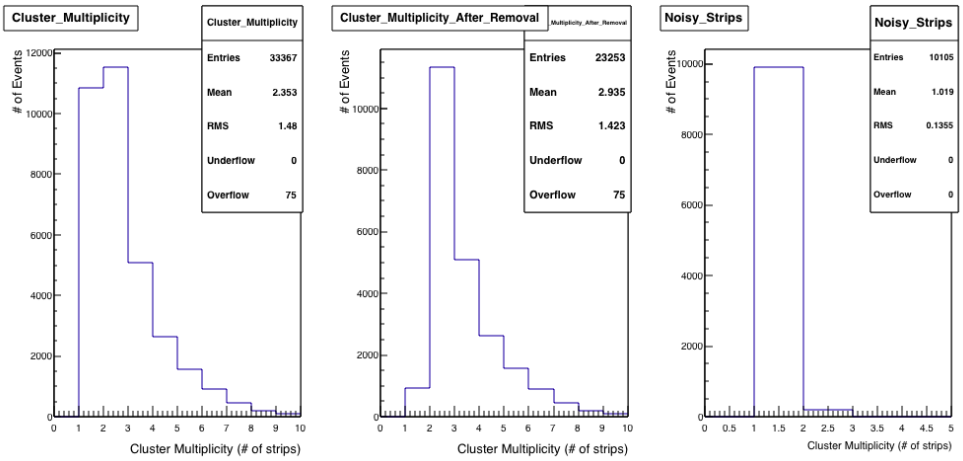

Figure 4.25: Cluster multiplicity for the amplification field of 590 V

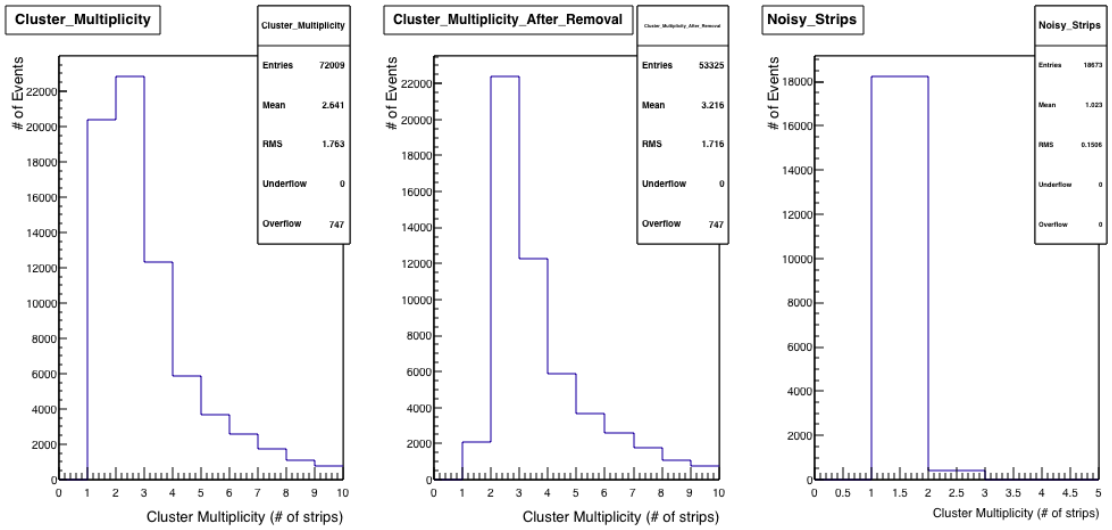

Figure 4.26: Cluster multiplicity for the amplification field of 610 V

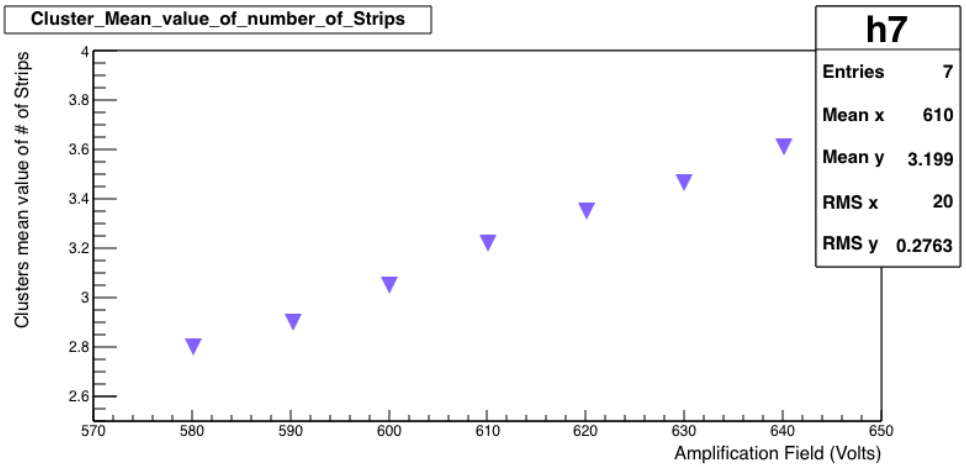

Figure 4.27: Cluster multiplicity as a function of the amplification field.

The same data were used to get the weighted cluster position with the centroid method. Cluster position is shown for the three areas. Especially for trajectories in the centre section of the beam the peaks are lowered after background removal.

At the areas of the non working channels right before and after the gap, there is an overflow of entries. This happens because the six first channels of each chip are not operating and the algorithm is creating those peaks filling the areas with entries that elsewhere would be in the gap. Some of the peaks are lowered after the noise removal. This is more clear for the Runs with all the VMM chips on. Indicatively for two runs at 610 V with one VMM on and all the Vmm on :

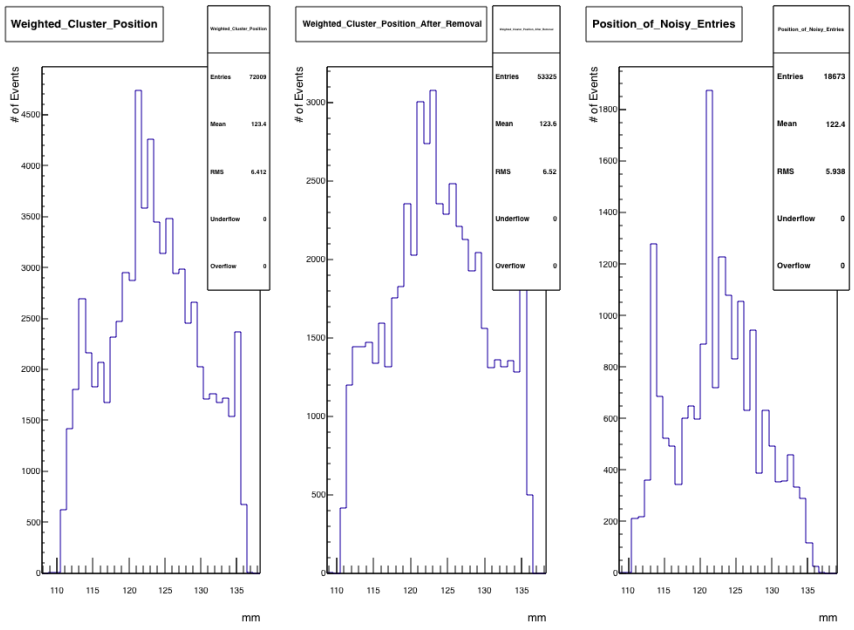

(a) Amplification Field 610 V

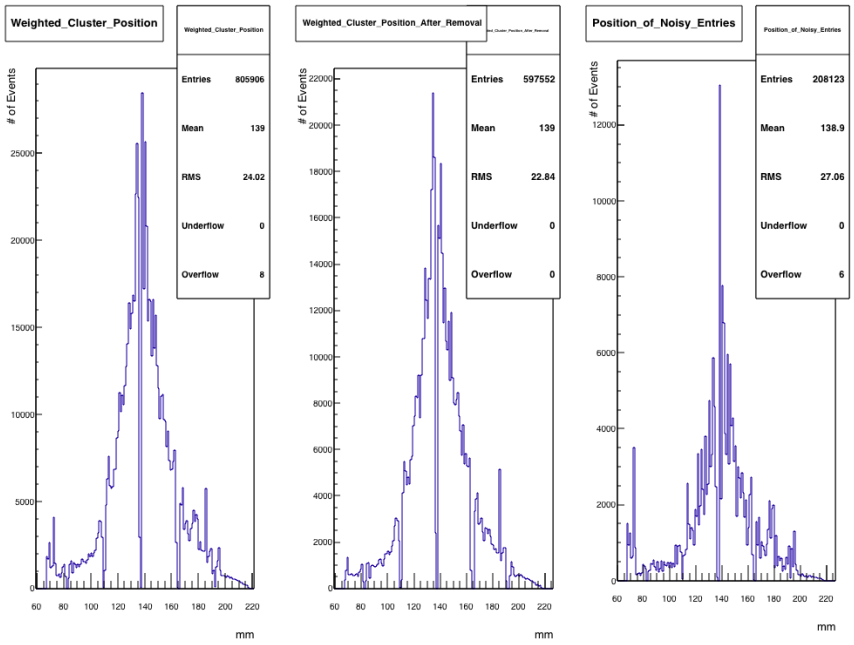

(b) Amplification Field 610 V

Figure 4.28: Weighted cluster position for one and for all the VMM chips activated.

4.2.6 Studies with the LM2 chamber

For studies of the LM2 chamber the same Strontium isotope was used. Strontium was placed in three different positions, two on the left side of the chamber and close to the MMFE8 board, then at a bigger distance and one on the right side close to the MMFE8. The LM2 chamber had a later version of the MMFE8 board and better outputs as derived. Performing the exact same measurements the efficiency is presented and analysis for the MMFE8 board on the LM2 was done for the clusters, the cluster multiplicity, cluster charge, timing output and cluster position. In every Run the Amplification Field was changed but all the VMM chips were activated.

Duplicate events in LM2

The duplicate clusters is still an issue in this version of the MMFE8. The duplicate strips removal algorithm and then a duplicate clusters removing algorithm same as SM1 analysis. For three different amplification field values, the following percentages of duplicates are found:

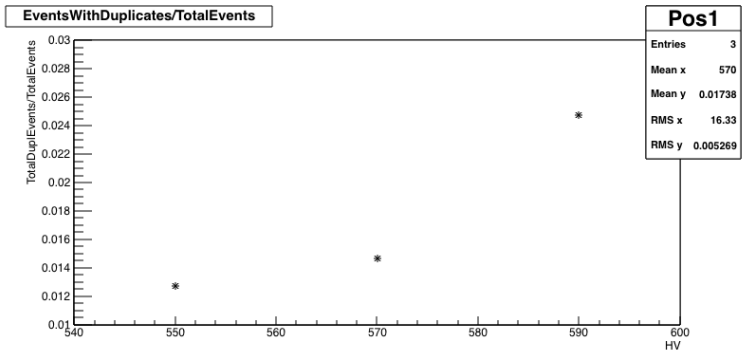

(a) Source in Position 1

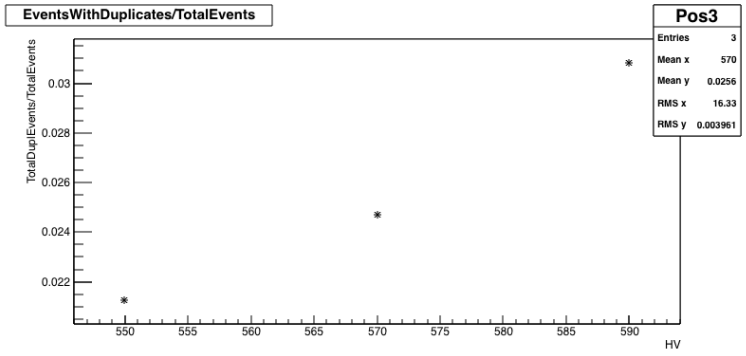

(b) Source in Position 3

Figure 4.29: The duplicates are in lower values than the previous front end board. Some differentiations in threshold values and the different position of the source give different duplicate entries

Pdo and Timing of the clusters at the LM2 chamber

At the LM2, the charge distribution of the clusters had an area with increased background entries at a similar range as the SM1 chamber but with a lower peak.

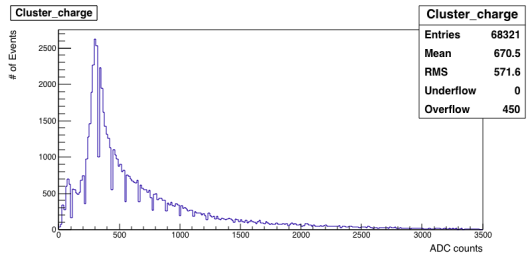

(a) Position 1

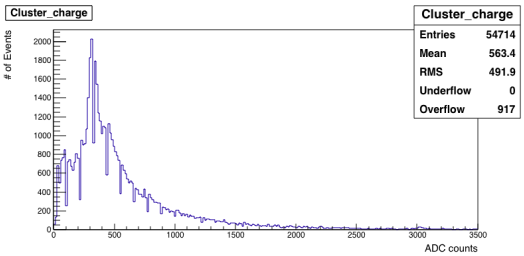

(b) Position 2

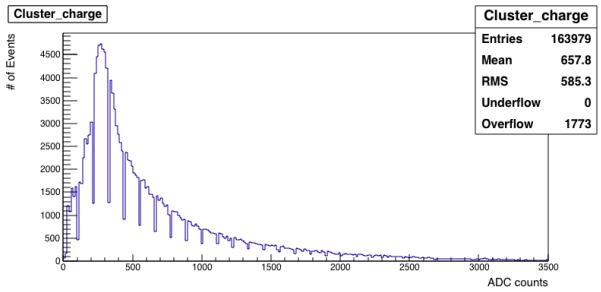

(c) Position 3

Figure 4.30: Same amplification Field of the 570V, the source is in three different positions

For the same amplification field of 570 V but with different positions for the source the exact area was derived and the background for this MMFE8 board in each Run. It is lower than the older version but it still affects the data. Indicatively for the two positions:

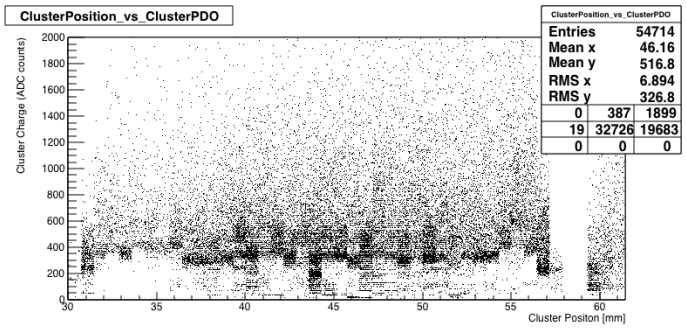

Figure 4.31: The Peak Detector Output as a function of the Cluster's Position. The source is in position 2, Ampl.Field at 570V

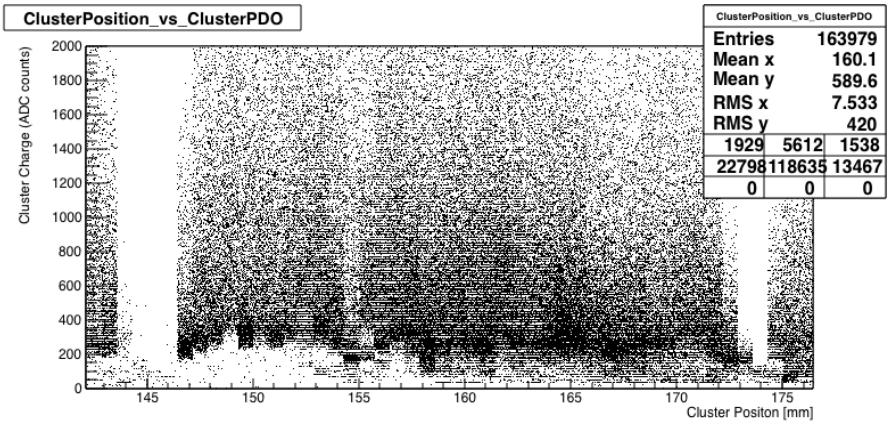

Figure 4.32: The Peak Detector Output as a function of the Cluster's Position. The source is in position 3, Ampl.Field at 570V

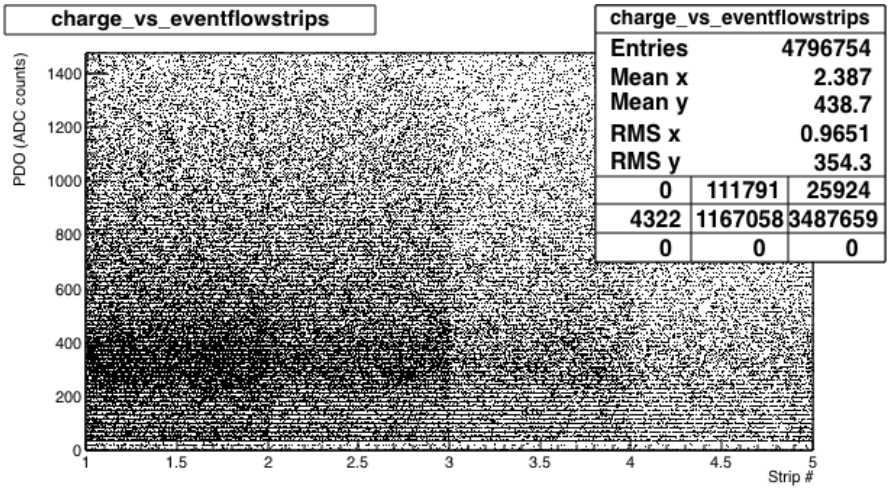

Figure 4.33: The strip number and the PDO of the strips. The Amplification Field is at 590 Volts, source in Position 3

In those two plots the focus is in the areas where the big number of hits was. So it can be now seen that the two positions of the LM2 chamber have lower number of hits in the noisy area than the SM1 chamber and the improvement in this later version is very significant. Nevertheless the correction must be applied so as to get better measurements. Those studies for the exact measurement of the area that the correction should be performed, were done for every Run we got with the LM2.

For the cluster charge in the three positions :

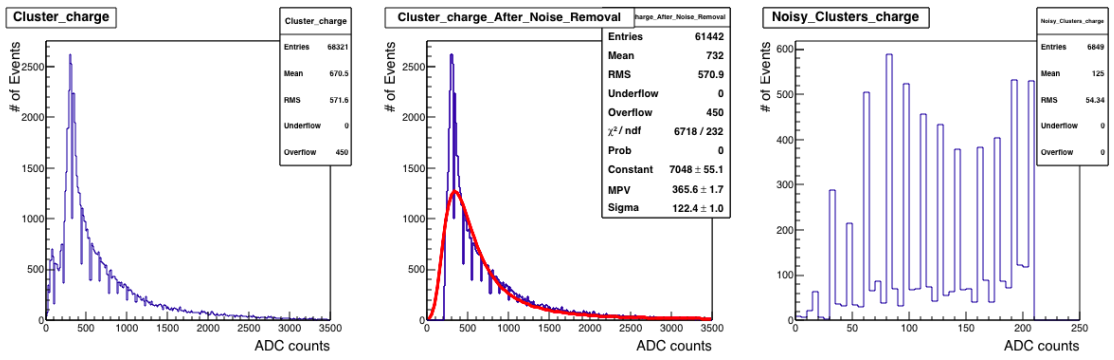

(a) Position 1

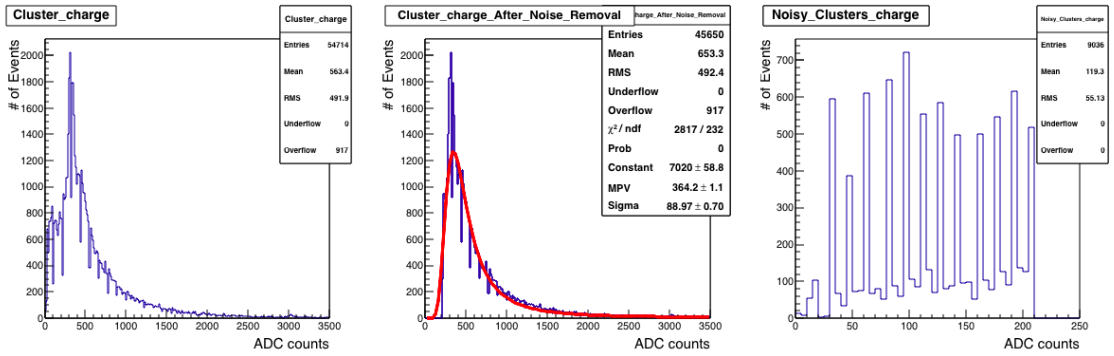

(b) Position 2

Figure 4.34: Same amplification Field (570V) the source is in two different positions

As seen the area of the clusters charge with the background is much improved but the noise, although in lower values, is at the same range. The pdo is fitted with a Landau function. For the timing distribution the same calculation method as described for the SM1 timing scheme was used. As seen the timing width is in lower values and closer to the expected.

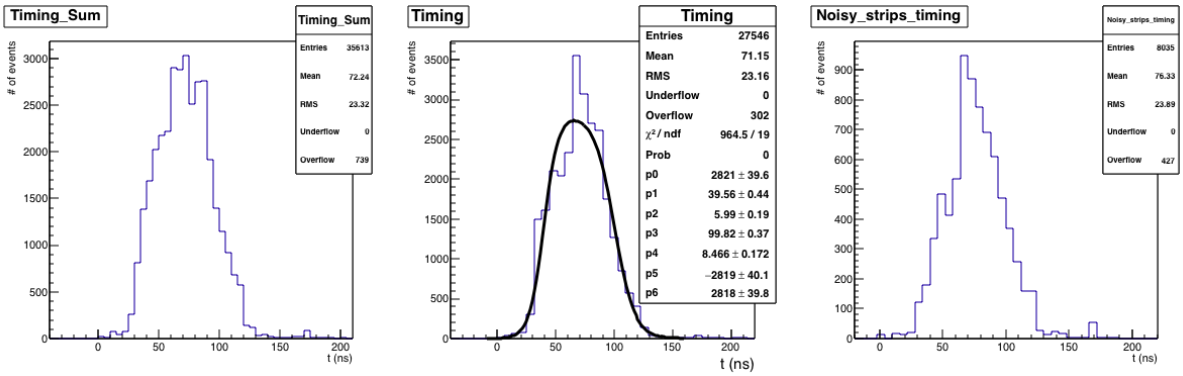

Figure 4.35: The timing width of the three areas. This timing distribution is for ampl.field of 550V and source in position 2.

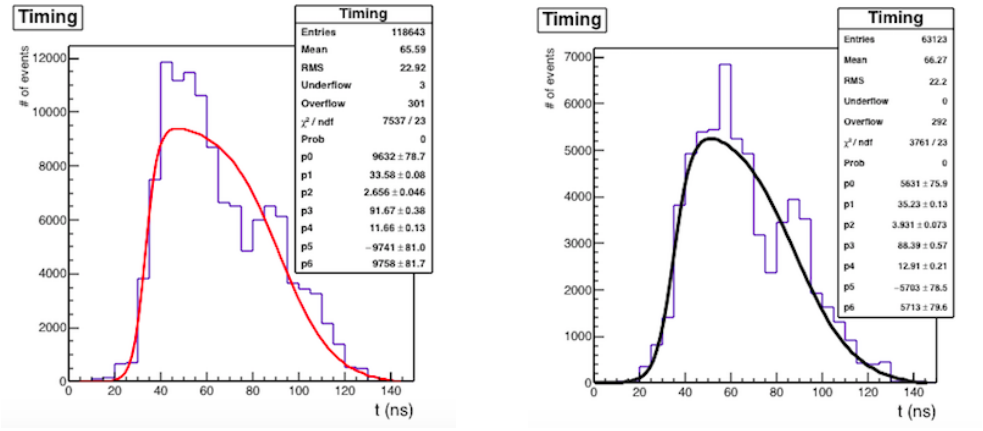

(a) Position 1 (b) Position 2

Figure 4.36: Two Runs for different positions for the timing width. We had 55-70ns timing width range which is vert close to the expected values.

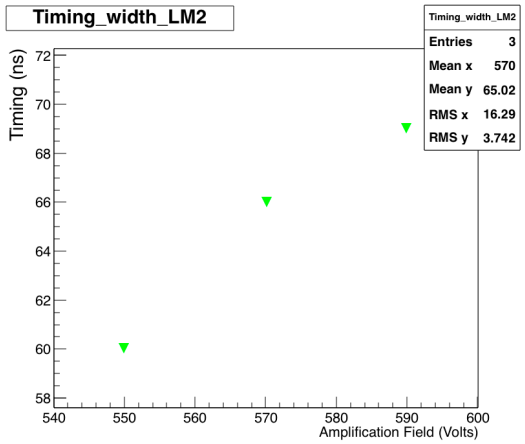

Figure 4.37: Timing width for the position one as a function of the amplification field.

Cluster Multiplicity

The cluster multiplicity measurements for the LM2 chamber are very promising. The events are better and the clusters are constructed from more than one strips. With the previous readout version in order to get better events it should be required that the cluster multiplicity must be biger than one strip. Also the LM2 chamber has wider strip pitch than the SM1 so this results have bigger importance since exactly the same Strontium source was used again for perpendicular tracks. Also the noisy area is constructed from more than one strips and it should be improved in the next version of the readout electronics.

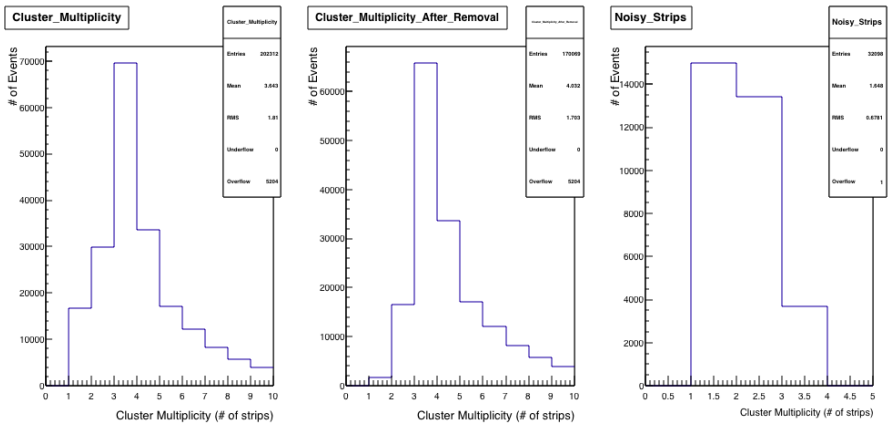

Figure 4.38: Cluster multiplicity for source in position 1 and ampl.field in 570V

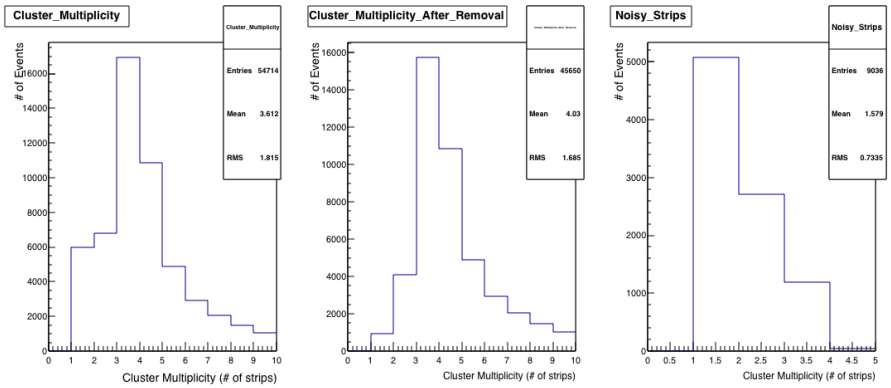

Figure 4.39: Cluster multiplicity for source in position 2 and ampl.field in 570V

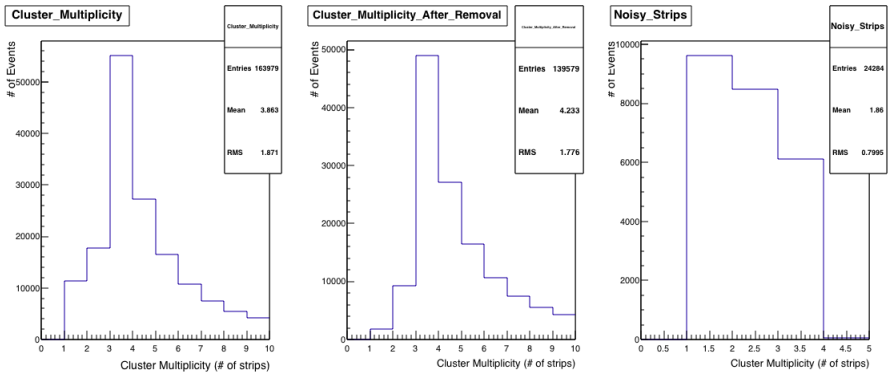

Figure 4.40: Cluster multiplicity for source in position 3 and ampl.field in 570V

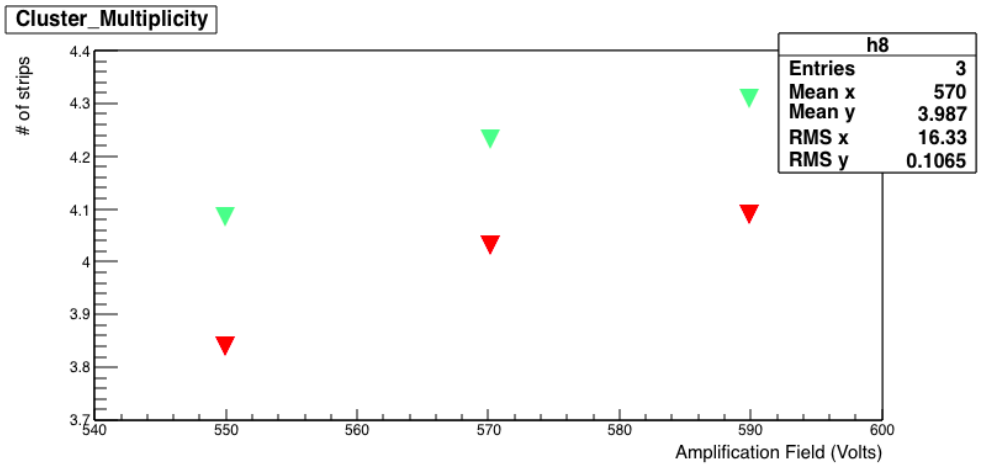

Figure 4.41: The higher range values(green) are for position three and the lower(red) for position 1

In the above figures are presented the results for three Runs with the same ampl.field but different position of the source. Also some tests were done with different amplifications and the source in different position. The average of 4 strips per cluster is in good agreement with the expected values and similar measurements for 0^o with the APV25 readouts.

Cluster Position

Since the tracks were perpendicular the centroid method was used to extract the cluster positions. For these reconstructed positions all the VMM chips were activated. With the comparison of the position 1 and 2 and same HV at 570V it is observed that two peaks at the 190-210mm area are a result from the noisy strips area.

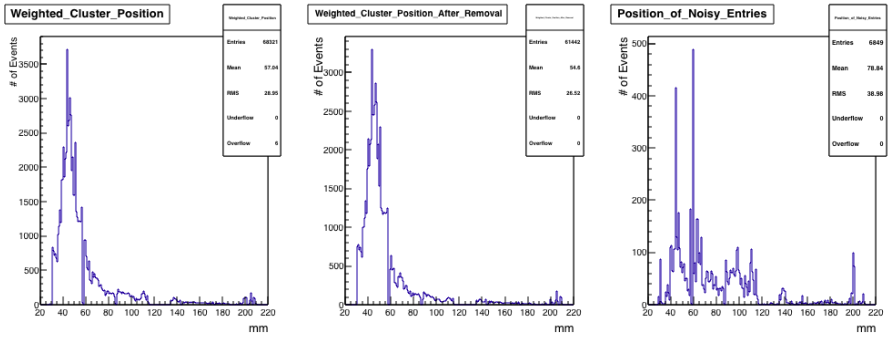

Figure 4.42: Position 1

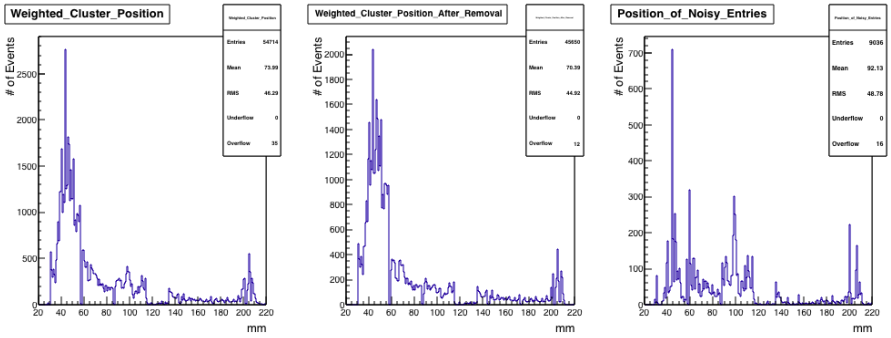

Figure 4.43: Position 2

From the beams profile it also the different distance source is, at the third position. Since there is lower number of entries in 40-60 mm area it can be seen that there is a peak of the same height in the same area as the one for the other two positions and shows inefficiency of the strips of this area. Same occurred for the 590 V ampl. field two pics at the same range for the same position which confirms our hypothesis.

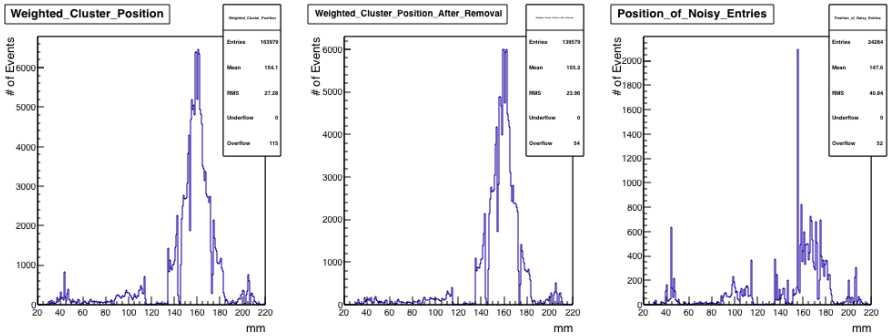

Figure 4.44: Position 3 (570V)

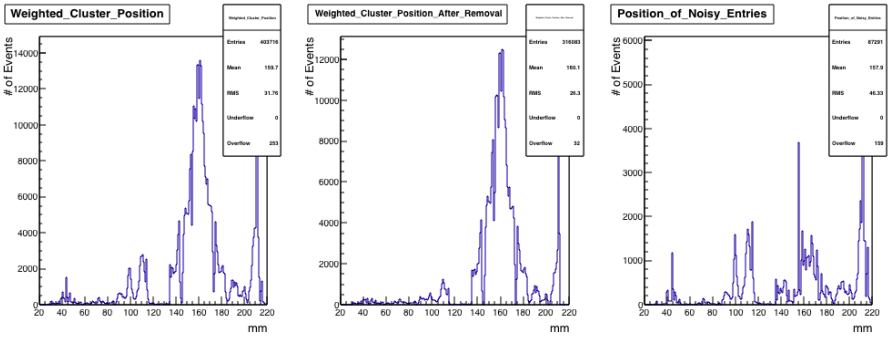

Figure 4.45: Position 3 (590V)

4.2.7 Studies with the VMM3 ASIC and Iron-55 radioactive isotope

The last section of this thesis contains the analysis of the studies with the VMM3 readout using a different chamber and a radioactive isotope. The experimental chamber was a resistive MM chamber with 1D readout and above we can see the characteristics.

Table 4.3: MicroMegas Detector Specs

MicroMegas Chamber	T-chamber with 1D readout
Strip Pitch	400μm
Strip width	140μm
Gas mixture	Ar+7%CO_2
Drift gap height	5mm
Amplification Gap	128μm
Drift Field	-300V
Amplification field	510V

VMM3 ASIC has many identical features with the VMM2 version [58] but as a result of beam, lab and chamber measurements, and extensive discussions and of course studies done jointly by the detector and electronics teams several changes were applied. Pin assignment and layout are identical to the VMM2 with 10 out of 400 pins to be different. The devise size is 21 x 21 mm^2 consistent with the MM detectors pitch. The VMM2 layout is 13.158 x 8.384mm^2. New BGA may have a higher ball count and, necessarily, smaller pitch in order to strengthen the power distribution

The Radioactive Isotope and expected peaks

In our tests a radioactive isotope of Iron was directed towards the chamber. The Iron-55 or ^{55}Fe nuclei decays to Manganese-55 (^{55}Mn) through electron capture of 1s electron with a half-life of 2.73 years [59]. After this procedure a core hole is created in the s level.

The electrons of a higher energy orbital, after a very small time frame, will fill the vacancy in the K shell and decay to the vacated 1s orbital. This energy transition, is given off as either an X-ray photon or as the kinetic energy of an Auger electron ejected from the atom.

If the result of this transition is an X-Ray photon, the X-Ray lines are oriented from 2p and 3p orbital transition generating the K-alpha-1, K-alpha-2 and K-beta X-Ray lines. The K-alpha-1 with energy of 5.89875 keV and K-alpha-2 with energy of 5.88765 keV come from the the 2p orbital or L shell, the line is in fact a doublet and the slightly different energies are a result of the spin-orbit interaction between the electron spin and the orbital momentum of the 2p orbital [60]. The K-beta of

6.49045 keV energy is a result of the transition from 3p orbital to 1s. The energies of these X-rays are so similar that they are often specified as mono-energetic radiation with 5.9 keV photon energy. Also energy is released with the emission of Auger electrons of 5.19 keV.

A second peak in a lower energy range is expected, the argon escape peak. The ^{55}Fe X-rays photoelectrically ionise the inner shell electron in argon atoms creating this peak. Electrons in higher orbitals decay to the vacated lower energy orbital and X-ray is emitted. Sometimes this X-ray can get out of the detector taking ∼3 KeV of energy with it. This leaves an amount of energy in the detector equal to the energy of the original ^{55}Fe X-ray minus the energy of the Ar X-ray [61].

In addition to the previous categories a smaller peak is expected in lower energies due to the presence of the cosmic ray background. Under the conditions data were taken and background is probably created primarily due to muons. The time window of this Run was big enough so considerable muon entries in the lower energies are expected. Compared to the decay products, these muons are highly energetic and deposit only a tiny fraction of their total energy in the detector. When muons interact with the gas they deposit an amount of charge proportional to the length of their paths inside the detector.

4.2.8 Cluster Multiplicity and Charge

The data from the VMM3 with the Iron-55 source had been proceeded to clusters. VMM3 although still in R&D process, has a better performance and no duplicate strips or clusters issues with minimum level of noise. We got a mean value of 1,036 clusters for this run and cluster multiplicity has a mean value of 3 strips per cluster as expected:

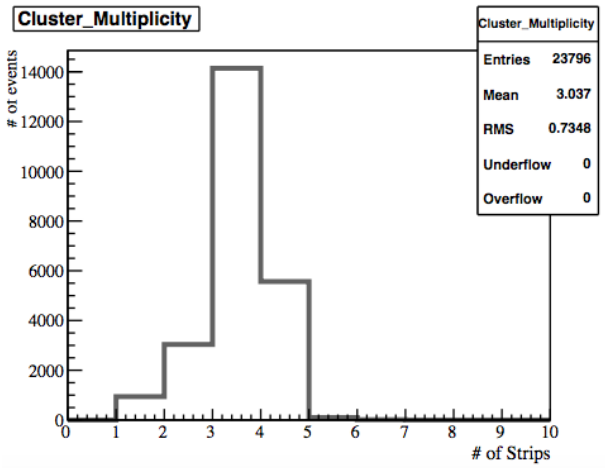

Figure 4.46: Cluster Multiplicity for the T-chamber with VMM3 readouts

The timing width measurements gave a 38 ns after the double Fermi Dirac function

which is not close to the expected value but this was due to the calibration constants. With better calibration constants better timing measurements can be extracted.

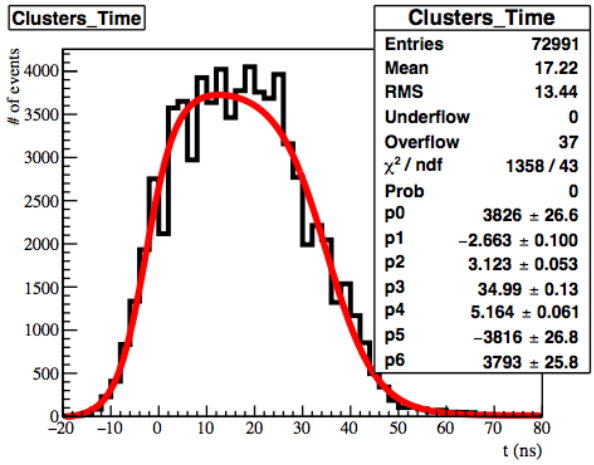

Figure 4.47: Timing width of the cluster strips

Then the cluster charge measurements were performed. As expected the two higher peaks, the 5.9 keV from the Iron-55 transitions and then a smaller at 3 keV from the argon escape are observed. Also a third peak caused from the cosmic ray background was present. This background is reduced after requiring only clusters with more than 2 strips.

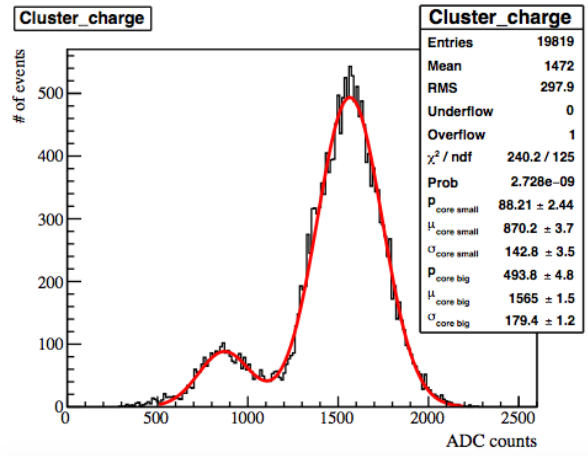

Figure 4.48: Charge of the clusters requiring multiplicity of three strips and higher.

The distribution if fitted with a double Gaussian function for both peaks. It is:

$$F(x) = A_1 e^{-(x-\mu_1)^2/(2\sigma_1)^2} + A_2 e^{-(x-\mu_2)^2/(2\sigma_2)^2} \tag{4.3}$$

Most of background is extracted and we can derive the energy resolution using the Full Width at Half Maximum (FWHM) which is the width of our distribution at the half of the maximum coordinate of the peak. For the Gauss function at half maximum height is:

$$\frac{A}{2} = Ae^{-x^2/(2\sigma_1)^2} \Rightarrow ln2 = \frac{x^2}{2\sigma^2} \Rightarrow x = \sqrt{2ln2}\sigma$$

So the energy resolution for a Gaussian distribution is:

$$E_{resol} = \frac{FWHM}{E_o} = \frac{2.3548\sigma}{E_o}100\%$$

The Energy resolution for the second Gaussian is a robust 27%.

CHAPTER 5

CONCLUSIONS

In this thesis we explored the outputs of this new setup. Tests were performed at the SPS/H6 area in September,December 2016 and January 2017. The MicroMegas chambers used are the prototypes of the NSW. The readouts were the latest implementations, which also will be used in the NSW as readout chips, the VMM2 and VMM3 ASIC.

The LM2 chamber had an MMFE8 board and the analysis done was very thorough. Many different amplification fields and tests with both all VMM and one VMM activated were performed. One problem was the duplicate strips and clusters. At the maximum amplification field used the duplicate clusters are at the level of 0.05% and can be removed with the software analysis. Also single strips creating a background area can also be corrected. So after the corrections this combination is very efficient.

The SM1 chamber had also the VMM2 ASIC but with a later version of the MMFE8 board. Several tests were performed activating all the VMM chips of the board, utilising different amplification fields and positions of the isotope. In the worst case the duplicates were at 0.03% improved from the previous MMFE8 and 4 times reduced background. Software correction can also be applied making the data outputs of the VMM2 reliable but further improvement was needed.

The VMM3 ASIC was tested in a T-chamber. The analysis had outputted zero duplicates and low level background so the data are very reliable and can be used directly. Further testing is needed though for the VMM3.

Next stage is using multiple MMFE8 layers in the different planes of the chamber's quadruplet. This must be done for different amplification fields, gas gain and sources. Taking more data not only for the perpendicular tracks but also for inclined tracks will be the final stage since it will reconstruct tracks as in real experiment conditions. With those methods we can measure the timing and spacing resolution of the NSW chambers and compare with the APV readout results.

BIBLIOGRAPHY

[1] T. Alexopoulos, G. Iakovidis, P. Gkountoumis, and A. Koulouris, "Level-1 data driver card design review report," *CERN*, 2015.

[2] P. Gkountoumis, "Electronics design and system integration of the atlas new small wheels," in *Siena,Italy*, 2016.

[3] LHC Collaboration, "Lhc design report," *CERN*, 2004.

[4] LEP Collaboration, "Lep design report," *CERN*, 1984.

[5] ATLAS Collaboration, "Atlas detector and physics performance: Technical design report," *CERN*, 1999.

[6] CMS Collaboration, "Cms physics: Technical design report volume 1: Detec- tor performance and software," *CERN*, 2006.

[7] LHCb Collaboration, "Lhcb : Technical proposal," *CERN*, 1998.

[8] TOTEM Collaboration, "Totem- technical design report," *CERN*, 2004.

[9] ALICE Collaboration, "Alice technical design report," *CERN*, 1998.

[10] ATLAS Collaboration, "Atlas central solenoid: Technical design report," *CERN*, 1997.

[11] ——, "Atlas central solenoid: Technical design report," *CERN*, 1997.

[12] ——, "Atlas barrel toroid: Technical design report," *CERN*, 1997.

[13] ——, "Atlas inner detector: Technical design report, 1," *CERN*, 1997.

[14] ——, "Atlas end-cap toroids: Technical design report," *CERN*, 1997.

[15] ——, "Atlas calorimeter performance: Technical design report," *CERN*, 1996.

[16] ——, "Atlas liquid-argon calorimeter: Technical design report," *CERN*, 1996.

[17] ——, "Atlas muon spectrometer: Technical design report," *CERN*, 1997.

[18] K. Ntekas, "Performance characterization of the micromegas detector for the new small wheel upgrade and development and improvement of the muon spectrometer detector control system in the atlas experiment," Ph.D. dissertation, National Technical University of Athens, 2016.

[19] H.Dekker et al, "The rasnik ccd 3-d dimensional alignment system," *eConf*, 1993.

[20] K. Hashemi and J.Bensinger, "The bcam camera," *Tech.Rep ATL-MUON CERN*, 2000.

[21] Long-wire data acquisition specification. [Online]. Available: http://alignment.hep.brandeis.edu/electronics/lwdaq/LWDAQ.html

[22] Fermi lab. [Online]. Available: http://home.fnal.gov/~farrell3/CSCSection/CSCTiming.pdf

[23] ATLAS Collaboration, "Observation of a new particle in the search for the standard model higgs boson with the atlas detector at the lhc," *Physics Letters B*, 2012.

[24] CMS Collaboration, "Observation of a new boson at a mass of 125 gev with the cms experiment at the lhc," *Physics Letters B*, 2012.

[25] HL-LHC: High Luminosity Large Hadron Collider. [Online]. Available: http://hilumilhc.web.cern.ch/about/hl-lhc-project

[26] ATLAS Collaboration, "Letter of intent for the phase-i upgrade of the atlas experiment," *CERN*, 2011.

[27] ——, "Letter of intent for the phase-ii upgrade of the atlas experiment," *CERN*, 2012.

[28] ——, "New small wheel technical design report," *CERN*, 2013.

[29] Yiannis Giomataris et al, "Micromegas: a high-granularity position-sensitive gaseous detector for high particle-flux environments," *Nuclear Instruments and Methods in Physics Research Section A: Accelerators, Spectrometers, Detectors and Asso- ciated Equipment*, 1996.

[30] G. Iakovidis, "Research and development in micromegas detector for the atlas upgrade," Ph.D. dissertation, National Technical University of Athens, 2014.

[31] ATLAS Collaboration, "Technical design report for the phase-i upgrade of the atlas tdaq system." *CERN*, 2013.

[32] E. Fermi, "The ionization loss of energy in gases and in condensed materials," *Phys. Rev. 57*, 1940.

[33] Particle Data Group, "Review of particle physics," *Chin.Phys.*, 2014.

[34] P.Langevin and C.R.Acad, "Sur la theorie du mouvement brownien," *C.R.Acad.Sci. 146*, p. 530, 1908.

[35] E. Dris and S. Maltezos, *Organology Notes*. NTUA, 2013.

[36] W.Shockley, "Currents to conductors induced by a moving point charge'," *Journal of Applied Physics 9*, p. 635, 1938.

[37] S.Ramo, "Currents induced by electron motion," *Proceedings of the IRE 27*, p. 584, 1939.

[38] E.Rutherford and H.Geigerg, "An electrical method of counting the number of α-particles from radio-active substances," *Proceedings of the Royal Society of London*, p. 141, 1908.

[39] A.Oed, "Position-sensitive detector with microstrip anode for electron multiplication with gases," *Nuclear Instruments and Methods*, p. 351, 1988.

[40] F.Sauli, "Gem: A new concept for electron amplification in gas detectors'," *Nu- clear Instruments and Methods in Physics Research Section A: Accelerators, Spectrometers, Detectors and Associated Equipment*, p. 531, 1997.

[41] Y.Giomataris et al., "Micromegas: a high-granularity position-sensitive gaseous detector for high particle-flux environments," *Nuclear Instruments and Methods in Physics Research Section A: Accelerators, Spectrometers, Detectors and Associated Equipment*, 1996.

[42] J. WOTSCHACK, "The development of large-area micromegas de- tectors for the atlas upgrade," *Modern Physics Letters A*, 2013.

[43] T. Alexopoulos, G. Iakovidis, and G. Tsipolitis, "Study of resistive micromegas detectors in a mixed neutron and photon radiation environment," *Journal of Instrumentation 7*, 2012.

[44] J. Bortfeldt, "Construction and test of full-size micromegas modules for the atlas new small wheel upgrade," *ATL-MUON-PROC-2015-017*, 2015.

[45] G.Iakovidis, "Research and development in micromegas detector for the at- las upgrade," Ph.D. dissertation, National Technical University of Athens, 2014.

[46] MMFE-8 specification. [Online]. Available: https://indico.cern.ch/event/354058/session/0/contribution/5

[47] The Front End Card with 8 VMM (MMFE-8). [Online]. Available: https://edms.cern.ch/file/1470529/1/NSW_MMFE-8-Specification-020515_PDR.pdf

[48] Yao Lin, "The address in real time card for the micromegas detector of the atlas muon upgrade," *Brookhaven National Laboratory*, 2016.

[49] V. Polychronakos and L. Yao, "February 2015 nsw electronics design reviews art data driver card," *Brookhaven National Laboratory*, 2014.

[50] G.De Geronimo et al, "Vmm1 - an asic for micropattern detectors," *Nuclear Science, IEEE Transactions on 60*, 2013.

[51] G. De Geronimo et al, "Asic for small angle neutron scattering experiments at the sns," *Nuclear Instruments and Methods*, 2007.

[52] M. French et al, "Design and results from the apv25, a deep sub-micron cmos front-end chip for the cms tracker," *Nuclear Instruments and Methods in Physics Research Section A: Accelerators, Spectrometers, Detectors and Associated Equip- ment*, vol. 466, 2001.

[53] MMDAQ. [Online]. Available: https://indico.cern.ch/event/218341/session/1/contribution/22/attachments/352429/491014/mmdaq_QA.pdf

[54] RECOMM. [Online]. Available: https://twiki.cern.ch/twiki/bin/viewauth/Atlas/RecoMm

[55] ROOT - data analysis framework. [Online]. Available: http://root.cern.ch/drupal/

[56] G. Geronimo and S.Li, "Shaper design in cmos for high dynamic range," *Nuclear Science*, 2011.

[57] K. Kölbig and B. Schorr, "A program package for the landau distribution," *Computer Physics*, vol. 31, 1984.

[58] V.Polychronakos, G.Iakovidis, and G.De Geronimo, "Atlas nsw electronics specification," *CERN*, 2016.

[59] G. Audi, *Nuclear Physics A*. The Nubase evaluation of nuclear and decay properties, 2003.

[60] E. Hussein, *Handbook on Radiation Probing, Gauging, Imaging and Analysis: Volume I: Basics and Techniques*. Springer, 2003.

[61] P.K.Lightfoot, K. Mavrokoridis, Y. Ramachers, G. Barker, and N. Spooner, "Optical readout tracking detector concept using secondary scintillation from liquid argon generated by a thick gas electron multiplier," *Instrumention and Detectors*, 2008.